



**BUDAPEST UNIVERSITY OF TECHNOLOGY AND
ECONOMICS**

FACULTY OF CHEMICAL TECHNOLOGY AND BIOTECHNOLOGY

GYÖRGY OLÁH DOCTORAL SCHOOL

PhD Dissertation Title

Complex inverse opal photonic crystals for improved photocatalysis

Author: Hamsasew Hankebo Lemago,

PhD Candidate at the Department of Inorganic and Analytical Chemistry,
Budapest University of Technology and Economics, BME

Supervisor: Prof. Dr. Imre Miklós Szilágyi (Professor, University of Miskolc,
Institute of Physical Metallurgy, Metal Forming and Nanotechnology)

Internal Consultant: Dr. János Madarász (Associate professor, BME Department
of Inorganic and Analytical Chemistry)

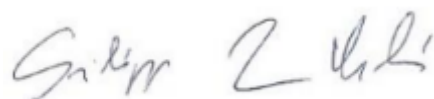
November 2025,

Budapest, Hungary

Statement of the Supervisor

I, **Dr. Szilágyi Imre Miklós**, as the supervisor (external), hereby declare that the thesis written by Hamsasew Hankebo Lemago (Neptune code: SV7CMT) titled **Complex inverse opal photonic crystals for improved photocatalysis** is his writing and that I supported his work with regular consultations. I also declare that the thesis meets the formal and professional requirements of the Budapest University of Technology and Economics and those of the Faculty of Chemical Technology and Biotechnology, thus I support its submission.

(Budapest, November 06, 2025)



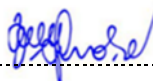
Professor Dr. Szilágyi Imre Miklós

Statement of the Student

I, **Hamsasew Hankebo Lemago** (Neptune Code: SV7CMT), as author of the dissertation, hereby declare that my thesis titled **Complex inverse opal photonic crystals for improved photocatalysis** is my original writing and I have not plagiarized any other work.

All third-party materials, including published and unpublished sources, were referenced. I acknowledge that the intellectual property rights of the methods used and the results of any research or development described in the thesis belong to the participating researchers and institutions/companies, thus their utilization or publication must not be initiated before the approval of all parties. I also declare that during the preparation and writing the thesis, I did not mislead my supervisor(s) and thesis advisor.

(Budapest, November 06, 2025)



Hamsasew Hankebo Lemago (PhD Candidate)

TABLE OF CONTENTS

TABLE OF CONTENTS	IV
LISTS OF ABBREVIATIONS	VII
LIST OF FIGURES	IIX
LIST OF TABLES	IX
1. INTRODUCTION	12
2. LITERATURE REVIEW	15
2.1. Advancements in Inverse Opal Materials	15
2.2. Characteristic Properties of IO Materials	16
2.2.1. Periodicity	16
2.2.2. Photonic Band Gap	17
2.2.3. Slow Photon Effects	18
2.3. Atomic Layer Deposition	18
2.3.1. Summary of ALD methods: TALD vs PEALD	20
2.4. TiO ₂ Inverse Opal	21
2.5. ZnO Inverse Opal	24
2.6. Al ₂ O ₃ Inverse Opal	27
2.7. Applications of Inverse Opal Materials	30
2.7.1. Photocatalysis	30
2.7.2. Photocatalytic Dye Degradations	30
2.7.3. Photocatalytic Water Splitting	32
2.7.4. Biological Application of IOPC	33
3. KNOWLEDGE GAP	36
4. EXPERIMENTAL METHODS	37
4.1. Aims of the Experiments	37
4.2. Preparation of PS Nanosphere Opal Sacrificial Template	37
4.2.1. Materials Used	37
4.2.2. Preparation of the template from the PS suspension	38
4.2.3. Preparation of the Template from PS powder	38
4.3. Thin Film Deposition Using ALD Methods	39
4.3.1. PEALD Film Growth	40
4.4. Heat Treatment of the Samples: Annealing and Post-Annealing	41
4.5.1. Thermal Analysis by TG/DTA-MS	42
4.5.2. FTIR Analysis	42
4.5.3. Morphological and Cross-Sectional Analysis by SEM and TSEM	42

4.5.4. Atomic Force Microscopy	43
4.5.5. Compositional Analysis By EDX.....	43
4.5.6. XRD Structural Analysis	43
4.5.7. Raman Structural Analysis	44
4.5.8. UV Visible is Optical Analysis and Photonic Band Gap Estimation.....	44
4.5.9. Ellipsometry Thickness Analysis.....	45
4.5.10. Photoluminescence Spectra Analysis	45
4.5.11. X-ray Photoelectron Spectroscopy Measurement	45
4.5.12. Photocatalytic Activity Measurement.....	46
4.5.13. Measurement by Doctoral Candidate and Collaborators.....	46
5. RESULT AND DISCUSSION.....	48
5.1. Thermal, FTIR, and Morphological Analysis of PS Nanospheres With Various Sphere Size Differences	48
5.1.1. Thermal Analysis Results	48
5.1.2. FTIR Analysis Results	48
5.2. Synthesis of IOs TiO ₂ , ZnO, and Composites Using PS-300 Template using PEALD Methodology	50
5.2.1. Morphology & Composition Analysis of IO via PS-300 Template.....	50
5.2.2. Crystalline Structure Analysis: XRD and Raman Analysis.....	51
5.2.3. UV Visible Absorption and PL in IO Materials.....	53
5.2.4. Photocatalytic Studies.....	54
5.2.5. The Photodegradation Mechanism	56
5.3. Thermal and Plasma-Enhanced ALD for the Synthesis of Inverse Opal Al ₂ O ₃ and Its Composite Materials	57
5.3.1. Morphological Studies by SEM and AFM	57
5.3.3. Optical Properties Determined by UV Visible and PL Spectroscopy.....	60
5.4. Fabrication of ZnO-Al ₂ O ₃ Inverse Opals with Atomic Layer Deposited Amorphous-Al ₂ O ₃ for Enhanced Photocatalysis.....	63
5.4.1. Morphological and Compositional Analysis	63
5.4.2. Crystalline Structure Determined by XRD and Raman Spectroscopy Analysis	64
5.4.3. UV Absorption and PL analysis.....	65
5.4.4. Photocatalytic Studies of ALD-Synthesised Inverse Opals Under Visible Light...67	
4.5. Synthesis of TiO ₂ /Al ₂ O ₃ Double Layer Inverse Opal by Thermal and Plasma-Assisted ALD for Photocatalytic Applications.....	69
4.5.1. Morphological and Compositional Analysis of the ALD IO samples	69
4.5.2. Structural and Optical Studies	70

5. CONCLUSION.....	74
6. THESIS POINTS	76
7. PUBLICATIONS	78
7.1. PUBLICATIONS RELATED TO DISSERTATION.....	78
7.2. PUBLICATIONS NOT RELATED TO DISSERTATION.....	79
8. CONFERENCE PARTICIPATION	80
8. REFERENCES	82
9. APPENDICES.....	102
9.1. APPENDIX A	102
9.2. APPENDIX B	102
9.3. APPENDIX C	102
9.4. APPENDIX D.....	103
9.5. APPENDIX E	104
9.6. APPENDIX F.....	104
9.7. APPENDIX G.....	105
9.8. APPENDIX H.....	106
9.9. APPENDIX I	106
9.10. APPENDIX J	107
9.11. APPENDIX K.....	107
9.12. APPENDIX L.....	107
10. ACKNOWLEDGEMENT	108

LISTS OF ABBREVIATIONS

Abbreviation	Full Form
1D	One-dimensional
2D	Two-dimensional
3D	Three-dimensional
3DOM	Three-dimensionally ordered microporous
AFM	Atomic Force Microscopy
ALD	Atomic Layer Deposition
AuNP	Gold nanoparticle
CVD	Chemical Vapour Deposition
DEZ	Diethyl Zinc
ED	Electron Deposition
E_g	Electric Band Gap Energy
FCC	Face Centered Cubic
FTIR	Fourier Transform Infrared
FWHM	Full Width at Half Maximum
GOD@SiOs	Glucose oxidase-containing silica inverse opals
GPC	Growth per Cycle
IO	Inverse Opal
IOPC	Inverse Opal Photonic Crystal
MB	Methylene Blue
MS	Mass Spectroscopy
4-NP	4-Nitrophenol
OPH@SiOs	Organophosphorus hydrolase-containing silica inverse opals
PAM	Polyacrylamide Microspheres
PBG	Photonic Band Gap
PC	Photonic Crystal
PEALD	Plasma-Enhanced Atomic Layer Deposition
PL	Photoluminescence
PMMA	Polymethyl Methacrylate
PS	Polystyrene
PS-300	Polystyrene nanosphere 300 nm pore size

PS-460	Polystyrene nanosphere 460 nm pore size
PS-600	Polystyrene nanosphere 600 nm pore size
RF	Radiofrequency
Rh6G	Rhodamine 6G
RhB	Rhodamine B
RMS	Root Mean Square
SCO	Semiconductor Oxide
SEM	Scanning Electron Microscope
SEM/EDX	Scanning Electron Microscope/Energy Dispersive X-ray Spectroscopy
SiO ₂	Silica
TALD	Thermal Atomic Layer Deposition
TDMATi	Tetrakis(dimethylamino) titanium
TG/DTG/DTA	Thermogravimetry/Differential Thermal Analysis/Derivative Thermogravimetry
TMA	Trimethylaluminum
TSEM	Transmission Scanning Electron Microscope
TEM	Transmission Electron Microscope
VLD	Vertical Layer Deposition
XPS	X-ray Photoelectron Spectroscopy
XRD	X-ray Diffraction Spectroscopy
ZnO QDs@3DOM TiO ₂	TiO ₂ nanocomposites decorated by ZnO quantum dots
ZnO-PCs	Zinc oxide photonic crystals

LIST OF FIGURES

Figure 2.1: SEM images of the IOs of Cr ₂ O ₃ (a), Ga ₂ O ₃ (b), Fe ₂ O ₃ (c), and In ₂ O ₃ (d) IOs, prepared from pure metal nitrates as precursor [30].....	16
Figure 2.2: Schematic representation of TiO ₂ synthesis via ALD using various precursors: (a) titanium isopropoxide and H ₂ O [69], (b) tetrakis(dimethylamino) titanium (TDMATi) and H ₂ O [70], and (c) the ALD-synthesized TiO ₂ IO structure [37].....	22
Figure 2.3: Schematic representation of the fabrication of TiO ₂ IO decorated with metal nanoparticles (a-b), TiO ₂ IO/Au, and (c) TiO ₂ IO decorated with Au and Ag [68,71,76].....	24
Figure 2.4: Representation of one ALD cycle (ZnO) with the sequential precursor exposure [86].....	26
Figure 2.5: Fabrication of ZnO-IO conformally coated by multi-step ALD deposition [33]..	26
Figure 2.6: SEM images of Al ₂ O ₃ as a function of heat treatment [101].....	28
Figure 2.7. XRD shows γ -Al ₂ O ₃ shows precursor (boehmite)[102].....	29
Fig. 2.8: Schematic representation of photocatalytic processes, (a) Under UV light, ZnO-PC directly absorbs light, exciting electrons (e ⁻) and creating holes (h ⁺) for photocatalysis (left). Under visible light, dye molecules (RhB or MB) absorb light, inject excited electrons into ZnO-PC, and participate in photocatalysis (right) [41] and (b) Photocatalytic activity in AuNP TiO ₂ /ZnO IO structure [119].....	32
Figure 2.9: PS microspheres were deposited on the indium tin oxide glasses by the vertical self-assembly method for biosensor applications [129].....	35
Figure 2.10: (a) Schematic illustration of the preparation of an enzyme-containing silica IOs, and (b); (a) SEM micrograph of polyacrylamide microspheres(PAM), (b) SEM, (c) TEM, and (d) confocal laser scanning microscopy micrograph of the enzyme-containing silica IOs [132].	35
Figure 4.1: (a) Glass substrate preparation involves cleaning with soap, ethyl alcohol, and water, followed by soaking in piranha solution and drying in a furnace, and (b) Opal template synthesis starts with diluting PS nanosphere suspension, ultrasonication, vertical deposition onto the glass substrate, and drying to form the opal structure	38
Figure 4.2: Illustrates the fabrication of a PS nanosphere template on a glass substrate: (a) PS powder is scraped, (b) suspended in water, (c) dispersed (3 min), (d) deposited onto glass via VLD at 80 °C, resulting in (e) a 600 nm sized opal template.....	39
Figure 5. 1. FTIR spectra of PS templates with different particle sizes: (a), PS-460, (b), and PS-600 (c) nanospheres in both air and N ₂ atmospheres, respectively.....	49

Figure 5.2: SEM images of PS nanosphere templates of varying sizes, (a) 300nm, (b) 460nm, and (c) 600nm, respectively	50
Figure 5.3: Displays SEM images of TiO ₂ IO (a, e), ZnO/TiO ₂ (b, d), ZnO (c), TiO ₂ /ZnO (d), and TSEM images of ZnO/TiO ₂ (f) and TiO ₂ /ZnO (g, h), respectively.....	51
Figure 5.4: (a) XRD and (b) Raman spectroscopy analysis of the PEALD IO samples	52
Figure 5.5: (a) UV Visible absorbance spectroscopy, and (b) PL spectroscopy of TiO ₂ , ZnO, and their composite samples	54
Figure 5.6: Schematic representations of photocatalytic materials: PEALD-IOs of TiO ₂ and ZnO for degradation of pollutants under UV light irradiation.....	56
Figure 5.7. SEM micrographs of (a, b) Al ₂ O ₃ IO, (c) Al ₂ O ₃ /ZnO TALD, (d) Al ₂ O ₃ /TiO ₂ TALD, (e) Al ₂ O ₃ /ZnO PEALD, and (f) Al ₂ O ₃ /TiO ₂ PEALD IOs and their composite samples.	58
Figure 5.8. AFM images of: (a) 460-PS template, (b) pure Al ₂ O ₃ IO, (c) Al ₂ O ₃ /ZnO-TALD, (d) Al ₂ O ₃ /ZnO-PEALD, (e) Al ₂ O ₃ /TiO ₂ -TALD, (f) Al ₂ O ₃ /TiO ₂ -PEALD, respectively	58
Figure 5.9: Roughness analysis of Al ₂ O ₃ IO and composite samples using AFM	59
Figure 5.10: The XPS measurement results of Al ₂ O ₃ IO and its composite samples.....	59
Figure 5.11: (a) UV Visible absorption, and (b) PL spectroscopy of Al ₂ O ₃ IO samples and composite samples, respectively	61
Figure 5.12: SEM images of pure ZnO IO (a,b), ZnO/Al ₂ O ₃ -T (c,d), and ZnO/Al ₂ O ₃ -P (e,f), respectively	64
Figure 5.13. (a) XRD diffraction patterns, (b) Raman spectroscopy, (c) UV Visible absorption spectroscopy, and (d) the PL emission spectra of: pure ZnO IO, composite ZnO-Al ₂ O ₃ -T, and composite ZnO-Al ₂ O ₃ -P, respectively	67
Figure 5.14: Decolorization of MB, Rh6G, and 4-NP dyes through photocatalysis under visible light irradiation for 3 hours using photocatalyst samples grown through ALD. (a-c) Photocatalytic performance – A _t /A ₀ vs irradiation time, using ALD photocatalyst samples in the presence of MB (a), Rh6G (b), and 4-NP (c), respectively.....	68
Figure 5.15: SEM micrograms of (a) pure TiO ₂ IO, (b) TiO ₂ /Al ₂ O ₃ -TALD, and (c) TiO ₂ /Al ₂ O ₃ -PEALD, respectively	69
Figure 5.16 (a) XRD, (b) Raman analysis results of IOs of pure TiO ₂ , TiO ₂ /Al ₂ O ₃ -thermal, TiO ₂ /Al ₂ O ₃ -plasma ALD composite samples, respectively	72
Figure 5.17: UV Visible absorption results of IOs of pure TiO ₂ (a), TiO ₂ /Al ₂ O ₃ -TALD (b), TiO ₂ /Al ₂ O ₃ -PEALD (c) composite samples, and (d) PL spectroscopic results, respectively. .	72

LIST OF TABLES

Table 4.1: TiO ₂ IO coated with an ultrathin layer of Al ₂ O ₃ TALD and PEALD	39
Table 4.2: ZnO IO coated with an ultrathin layer of Al ₂ O ₃ , TALD and PEALD	40
Table 4.3: TiO ₂ , ZnO IOs and their composite (TiO ₂ /ZnO and ZnO/TiO ₂) using PEALD	41
Table 4.4: Al ₂ O ₃ IO coated with an ultrathin layer of TiO ₂ , and ZnO using ALD methods	41
Table 4.5. Annealing program for all IO samples	42
Table 5.1. Crystallite size and FWHM analysis of pristine IO materials	53
Table 5.2: k _{app} of the samples, k _{app} [10 ⁻² /min ⁻¹].....	56
Table 5.3 EDX Table ZnO IO and composite samples	64
Table 5.4: The rate constant, k, and linear regression square, R ² , of the sample.....	73

1. INTRODUCTION

Over recent years, semiconductor oxides (SCO) have garnered significant attention due to their versatile technological applications. Their non-toxic nature, chemical stability, and environmental benefits make them promising candidates for addressing pressing issues such as environmental pollution and the global energy crisis. They have been widely explored for various applications, including solar cells, UV Visible light emitters, fuel cells, batteries, transparent electronics, and photocatalysis [1,2]. In photocatalysis, the process involves light absorption, the generation and separation of electron-hole pairs, their migration to the photocatalyst's surface, and the subsequent redox reactions. Due to their high photoactivity, SCOs play a crucial role in photocatalyzing diverse reactions such as water splitting, pollutant degradation, energy conversion, environmental remediation, and self-cleaning surfaces. These properties make SCO-based photocatalysis a transformative approach for tackling environmental and energy-related challenges while offering new possibilities in chemical synthesis and materials science [3–5].

Inverse opal photonic crystal (IOPC) materials have emerged as a powerful strategy to enhance SCO-based photocatalysis by improving light-harvesting efficiency, charge transport, and reaction kinetics [6]. They are materials with a periodic variation in their refractive index, which allows for manipulating light propagation within the crystals. They are created by the inverse replication of a self-assembled template structure (for example, polymers, silica), resulting in an ordered array of voids or pores within a solid matrix. This distinctive structure gives inverse opal (IO) a range of interesting optical properties, making them attractive for various applications. The periodic arrangement of voids in IO materials gives rise to a photonic bandgap (PBG), a range of wavelengths that are forbidden to propagate through the material. This bandgap can be tuned by changing the spheres' size, shape, and composition, allowing for control over the material's optical properties [7–10].

Nanolithography and the self-assembly of colloidal microspheres are two prevalent techniques employed in fabricating IO structures. Nanolithography, referred to as the "top-down" approach, is relatively expensive and time-consuming, resulting in only a few structural layers of materials [11]. On the other hand, the "bottom-up" method, involving the self-assembly of colloidal microspheres, offers a cost-effective means of preparing crystalline samples comprising several hundred structural layers of varying thickness. In the bottom-up approach, various templates such as silica (SiO_2), polystyrene (PS), or Polymethyl

methacrylate (PMMA) microspheres are meticulously arranged into an opal photonic crystal (PC) using methods like self-assembly [12], evaporation [13], stöber method [14], gravity sedimentation [15], and dip coating [16,17]. These opal PCs then serve as the templates into which the desired precursor or target material is introduced. Subsequently, the template is removed through calcination or etching, forming the IOPC. Throughout the preparation process, different methods can be employed to fill the precursor or target material, including Atomic Layer Deposition (ALD)[18], Chemical Vapor Deposition (CVD) [19], Electrochemical Deposition (ED) [20,21], sol-gel method [22,23], and more.

In this PhD study, I aimed to synthesize, analyse, and characterize ordered nanoporous IO structures composed of various oxides and their composites (TiO_2 , ZnO , Al_2O_3 , TiO_2/ZnO , ZnO/TiO_2 , $\text{TiO}_2/\text{Al}_2\text{O}_3$, $\text{ZnO}/\text{Al}_2\text{O}_3$, $\text{Al}_2\text{O}_3/\text{TiO}_2$, $\text{Al}_2\text{O}_3/\text{ZnO}$) using both ALD techniques via thermal ALD and plasma-enhanced ALD. My key objectives were to establish a controlled fabrication method for periodic polystyrene (PS) nanosphere sacrificial templates with diameters of 300 nm, 460 nm, and 600 nm through vertical layer deposition (VLD), which served as scaffolds for the subsequent ALD of IO oxides. These parameters critically influenced light localization and enhanced photocatalytic activity in the UV and Visible range. Additionally, I explored different synthesis pathways using both PS suspensions and powders to optimize template ordering, morphology, and structural integrity. My goal was to engineer these nanostructured IO materials with tailored compositions and architectures to enhance their photocatalytic performance. Specifically, I fabricated both pristine and composite IOs by depositing the selected metal oxides onto PS templates of varying sizes, followed by template removal via annealing.

I first focused on synthesizing TiO_2 , ZnO , and TiO_2/ZnO IO structures using PS-300 templates to maximize PBG effects in the UV Visible region and enhance their photocatalytic activities. I then investigated Al_2O_3 -based IO structures and their composites ($\text{Al}_2\text{O}_3/\text{ZnO}$ and $\text{Al}_2\text{O}_3/\text{TiO}_2$) using PS-460 templates, comparing TALD and PEALD techniques to evaluate their influence on film quality, surface morphology, and defect passivation. Finally, I extended the study to PS-600-templated ZnO and TiO_2 IOs coated with ultrathin Al_2O_3 layers to fabricate bilayer structures aimed at improving photocatalytic activity under UV and visible light. After preparing the IO materials, I conducted a comprehensive characterization of their structural, compositional, and optical properties using techniques such as Scanning Electron Microscope/Energy Dispersive X-ray Spectroscopy (SEM/EDX), Atomic Force Microscopy (AFM), X-ray Diffraction (XRD), Raman spectroscopy, X-ray Photoelectron Spectroscopy

(XPS), Photoluminescence (PL), and UV Visible spectroscopy. These analyses confirmed the crystalline structures of ZnO and TiO₂ and the amorphous nature of Al₂O₃. I also evaluated their photocatalytic performance under UV and visible light by testing the degradation of methylene blue (MB), rhodamine 6G (Rh6G), and 4-nitrophenol (4-NP).

2. LITERATURE REVIEW

2.1. Advancements in Inverse Opal Materials

The development of IO structures dates back to the late 20th century, driven by the need to engineer periodic dielectric materials for photonic applications. The breakthrough came in the 1990s with colloidal crystal templating, where monodisperse colloidal spheres, typically PS or silica, self-assemble into a close-packed template. This template is then infiltrated with high-refractive-index materials through sol-gel processing, ED, CVD, or ALD. The subsequent removal of the sacrificial template via calcination or chemical etching produces a highly ordered porous structure, the hallmark of IOs [23–25].

The metal oxide-based IO represents a sophisticated class of materials that have attracted substantial interest due to their distinctive structural and optical properties, which underpin a wide range of potential applications. These materials embody an advanced level of material design, extending beyond conventional metal oxides to incorporate intricate, ordered architecture at the nanoscale. Fundamentally, metal oxide-based IOs are 3D periodic structures comprising an interconnected metal oxide network with a regular array of air voids (macropores)[26–28]. These structures are typically synthesized using a template-based approach. The process involves the self-assembly of monodisperse colloidal spheres, often composed of polymers like PS or silica, into a highly ordered face-centered cubic (FCC) lattice, thus mimicking the structural attributes of natural opals. This colloidal crystal serves as the template. The interstitial spaces within the template are then infiltrated with a metal oxide precursor. Finally, the colloidal template is removed through calcination or chemical etching, leaving behind a 3D interconnected network of the metal oxide with a periodic arrangement of air voids, thus forming the IO structure [13,15,29].

Inverse opals of Cr_2O_3 , Ga_2O_3 , Fe_2O_3 , and In_2O_3 were fabricated via PMMA-templated infiltration and conversion (Fig. 2.1). The resulting structures exhibited vivid structural colors with strong reflectance peaks: Cr_2O_3 (red, 690 nm), Ga_2O_3 (orange-pink, 671 nm), Fe_2O_3 (maroon, 708 nm), and In_2O_3 (pink-purple, 636 nm) [30]. The precursor composition strongly influenced the quality and color intensity of the metal oxide IOs, with pure metal nitrates yielding well-ordered inverse opal architectures. Highly crystalline IOs (e.g., Nb_2O_5 , TiO_2) were made via soft-hard chemistry, enabling 700 °C treatment without collapse [31]. Other IOs (e.g., TiO_2 , Indium tin oxide) were created by evaporation-induced self-assembly and calcination for use in catalysis, energy, and biomedicine [13].

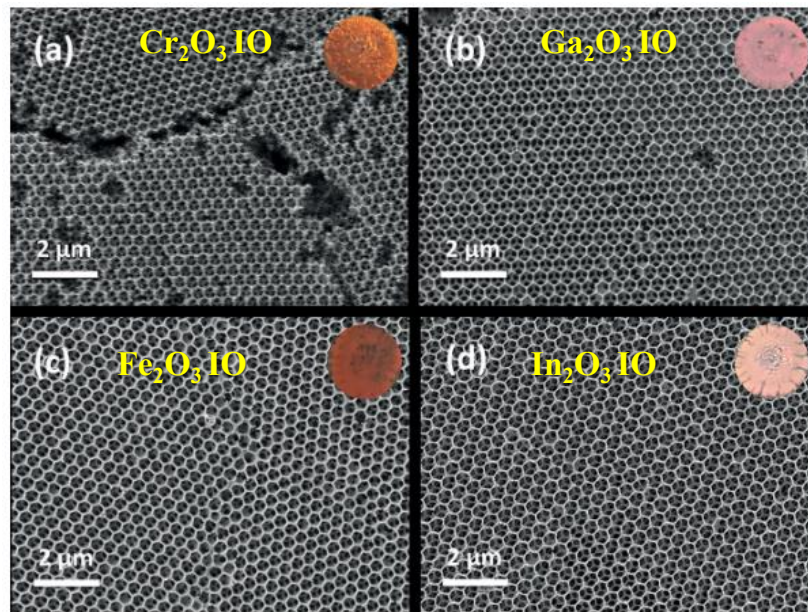


Figure 2.1: SEM images of the IOs of Cr_2O_3 (a), Ga_2O_3 (b), Fe_2O_3 (c), and In_2O_3 (d) IOs, prepared from pure metal nitrates as precursor [30].

2.2. Characteristic Properties of IO Materials

2.2.1. Periodicity

Periodicity in IO structures refers to the repeating center-to-center distance between neighboring pores, which is determined by the diameter of the spheres in the template. Larger template spheres result in larger pores and a greater periodicity, as the space between the spheres dictates the spacing between the pores. By adjusting the size of the template spheres, researchers can precisely control the periodicity of the IO, which is essential for applications that require specific pore sizes and periodicity, such as light manipulation and fluid control [32–34].

This periodic arrangement is the key to the photonic properties of IOs. It gives rise to a PBG, where specific light wavelengths are forbidden due to interference within the structure, and causes Bragg diffraction, leading to high reflection at specific wavelengths depending on the periodicity and refractive index contrast [27]. By precisely controlling the size of the spheres and the material filling the pores, researchers can fine-tune the periodicity and manipulate the resulting PBG for specific applications (e.g., optical sensors, catalysis, energy storage)[35–37].

Additionally, by introducing defects into this ordered structure, light can be further localized at the desired structure, offering even greater control over light manipulation. Ultimately, this inherent periodicity is what grants IOs their unique optical properties,

including the ability to slow down light, enhance light-matter interactions, and even create vibrant colors that change depending on the viewing angle [9,38].

2.2.2. Photonic Band Gap

IOPCs mimic semiconductors using a periodic structure to create PBG. This PBG restricts light propagation at specific frequencies, like a semiconductor band gap restricts electron flow [39]. While the material properties dictate a semiconductor's band gap, the PBG in IOPCs can be precisely tuned by controlling the structure and material filling the pores. Due to the differing dielectric media and the resulting refractive index contrast within the crystal, light is scattered and diffracted from various surfaces, creating a band of forbidden frequencies where the interference of scattered waves is destructive in all directions. Light cannot propagate within this region, and the greater the refractive index contrast, the wider the PBG becomes [29]. A full PBG is a feature only observed in PCs where light propagation is prohibited in all directions, while an incomplete PBG or pseudogap, also known as a stopband, prohibits light from propagating in only some directions. The wavelength range influenced by the PBG is determined by the lattice parameter or characteristic length scale of the crystal structure. The ability to tune the PBG to suit specific frequencies is one of the most attractive qualities of PCs [40].

The PBG in IOPCs arises due to the interaction between light and periodic structure, causing destructive interference of a certain range of wavelengths in the visible region. The presence of a PBG in IOPCs leads to several important optical phenomena. It can inhibit spontaneous emission, control the flow of light, and create localized modes where light is confined to specific regions within the crystal. The ability to control the size of the spheres and the material filling the pores allows scientists to fine-tune the periodicity and manipulate the resulting PBG for specific applications. By introducing defects (e.g., vacancies, pore size irregularities, dislocations) into the ordered structure, light can be further localized at desired wavelengths, offering even greater control over light manipulation. In one-dimensional (1D), 2D, and 3D PCs, the periodicity in one, two, or three directions, respectively, leads to unique optical properties. The most significant optical phenomena, including the PBG or stop-band, the inhibition of spontaneous emission, and the potential for localized modes, are applicable across all dimensional systems. The detailed design of PCs, particularly the periodic arrangement and refractive index contrast, determines the extent and position of the PBG, making these materials highly versatile for photonic applications [6,41,42].

2.2.3. Slow Photon Effects

IOPC exhibits a fascinating phenomenon called the “slow photon” effect. As light approaches the edges of the PBG, its group velocity plummets. This happens because the material's dispersion relation flattens in these regions, causing light to travel at a much slower pace, leading to a multitude of beneficial effects. By prolonging light-matter interaction through “slow photon”, enhanced nonlinear optical effects are achieved, making the material ideal for applications like sensors, lasers, and light-harvesting devices. This extended interaction time further strengthens the absorption and emission rates of embedded light sources like dyes or quantum dots, paving the way for efficient light-emitting devices. At the edges of the PBG, light experiences a dramatic reduction in speed, enhancing its interaction with the IO material. This effect is particularly strong when the edge of the PBG coincides with the absorption band of IO, leading to an increase in light-matter efficiency [43,44].

Moreover, the “slow photon” effect is beneficial for photocatalysis and other light-absorbing applications. For example, it has been utilized in thin-film multilayer solar cells to selectively enhance light absorption in the active layers, thereby boosting the photocurrent and overall efficiency of the solar cells. The “slow photon” effect, which occurs at the red (long-wavelength) edge of the PBG rather than the blue (short-wavelength) edge, was found to be more effective in enhancing photocatalysis[45,46].

2.3. Atomic Layer Deposition

ALD presents a promising and innovative synthetic pathway for creating IOs due to its exceptional step coverage, conformality, and ability to grow dense films with precise control over atomic structures. It is a deposition technique used to produce thin films with utmost precision at the atomic scale. It involves sequentially depositing individual atomic layers, typically through self-limiting surface gas-solid reactions. It involves the sequential introduction of two or more reactants, referred to as precursors, into a reactor. This process occurs under precisely controlled pressure and temperature conditions, enabling the layer-by-layer deposition of material onto the surface of a target substrate. The substrate is typically placed in a dedicated chamber that is integrated with the ALD reactor to ensure uniform coating and process stability [47].

To produce IO structures through the ALD method, the initial step involved the self-assembly of polymer templates on a substrate such as glass, a metal sheet (e.g., Al, Cu, or stainless steel), or a silicon wafer. These templates facilitated the formation of polymer

colloids. Next, the precursors (consisting of metal and oxidants) were introduced into the ALD reactor by sequentially employing N₂ or Ar gas. To transform the opal into ALD metal oxide IOs, the infiltrated opal underwent a high-temperature (500 °C) treatment in the presence of air. This process led to the decomposition and evaporation of the polymer opal layer, leaving behind the desired metal oxide IO structure [6,48,49].

There are two common types of ALD deposition methods used in IO synthesis: TALD and PEALD, which differ in the energy source used for deposition. High-quality ZnO inverse opals (IOs) have been successfully synthesized using TALD at temperatures between 160–240 °C. By adjusting the deposition temperature and number of ALD cycles, high-quality, periodically arranged IO structures can be achieved. Additionally, ALD has been employed to deposit protective layers of TiO₂ or Al₂O₃ on the prepared ZnO IOs [33].

Similarly, it was reported that a 0.25 nm SiO₂ layer deposited by ALD on TiO₂ IO structures, synthesized via sol-gel infiltration of PS opal templates followed by calcination, enhanced photocatalytic activity by 112 %, whereas thicker SiO₂ layers (>3 nm) hindered charge carrier transport to the surface. In contrast, Al₂O₃ ALD coatings on TiO₂ IO significantly suppressed photocatalytic activity, with even a 1 nm layer reducing performance by over 90%. These results highlight the critical influence of ALD parameters, coating thickness, and material selection on the photocatalytic activity of IO-based composite structures [50].

Plasmas in PEALD were commonly generated from O₂, N₂, H₂, or their mixtures, serving as reactant gases. They replaced the ligand-exchange mechanisms used with H₂O or NH₃ and enabled deposition of metal oxides, metal nitrides, and metal films. Plasmas were also generated in gases or vapors such as NH₃ and H₂O, which cause simultaneous plasma and surface reactions. PEALD required complexity and cost than TALD. It needed a plasma source with an RF power supply and extra gas flow controllers, and a pumping capacity was necessary. Reactor design was more intricate to ensure uniform exposure of substrates to short-lived radicals [51–53].

Another study explored plasma-enhanced spatial ALD for TiO₂ thin films on both 2D and 3D substrates, providing insights into crystallization and deposition mechanisms. It was reported that while this deposition method enabled conformal coating on high-aspect-ratio structures, partial crystallization occurred within 3D architectures due to variations in film thickness, highlighting the significance of thickness-dependent crystallization in complex

geometries [54]. Additionally, the research indicated that oxygen radical recombination probabilities in atmospheric pressure at 200°C were comparable to those in low-pressure PEALD, implying that differences in film conformality were influenced more by radical density and diffusion than by recombination effects. Furthermore, investigations into PEALD of TiO₂ in high-aspect-ratio trench structures (1:30) demonstrated that optimizing plasma exposure time and deposition temperature significantly improved step coverage, achieving over 95% conformality. These findings underscored the potential of PEALD for high-k dielectric applications and emphasized the necessity for process refinements to ensure uniformity in intricate nanostructures [55].

Furthermore, Studies demonstrated that ALD enabled the synthesis of various metal oxides, including TiO₂, ZnO, Fe₂O₃, and their composites. These inverse opals exhibited unique light-interaction properties, such as PBG effects, which enhanced their photocatalytic performance. They showed strong photocatalytic activity under both UV and visible light for pollutant degradation, while composites such as TiO₂/Fe₂O₃ achieved superior performance due to bandgap harmonization (engineering the energy band gaps of different materials in a heterostructure) and PBG enhancement, highlighting their potential for efficient photocatalysis [56–58].

2.3.1. Summary of ALD methods: TALD vs PEALD

TALD relies on thermal energy to activate surface reactions, enabling the growth of high-purity, conformal thin films through sequential, self-limiting steps. The deposition typically operates within a temperature window of 150–350 °C and at low pressures (~0.1–1 Torr), ensuring uniform film growth on substrates such as Si wafers, glass, platinum, and porous opal templates. The process commonly employs thermally stable precursors such as (e.g., TiCl₄, titanium isopropoxide (TTIP), diethyl zinc (DEZ), along with H₂O as the oxidant. While TALD offers excellent conformality on high-aspect-ratio such as features with deep pores or trenches, where the height or depth is much greater than the width, such as nanoporous or 3D architectures, its slower reaction rates and higher temperature requirements restrict its use with thermally sensitive materials and limit large-area scalability [59,60].

PEALD utilizes plasma to generate highly reactive species such as ions, radicals, and excited neutrals, which significantly enhance surface reactivity compared to purely thermal processes. These reactive species are typically produced using radiofrequency (RF) or inductively coupled plasma sources, enabling efficient activation of precursors even at lower substrate temperatures. PEALD operates under low-pressure conditions (typically 0.1–1 Torr)

and within a temperature range of 80–200 °C, which is considerably lower than the 150–350 °C required for TALD. The plasma activation accelerates the surface reactions, leading to faster deposition rates and more complete ligand removal, which results in denser films. This low-temperature capability makes PEALD particularly suitable for temperature-sensitive substrates such as polymers, flexible electronics, photoresists, and organic-inorganic hybrid materials, where high heat could cause deformation or degradation. Although PEALD produces films with enhanced density, improved mechanical properties, and broader precursor compatibility, the addition of plasma generation and control systems increases equipment complexity, maintenance requirements, and overall process cost compared to TALD [51,61,62].

2.4. TiO₂ Inverse Opal

Anatase, brookite, and rutile are the three crystalline forms of TiO₂, a white, stable substance. Anatase exhibits significant photocatalytic activity, although rutile is the most stable [63]. TiO₂ has a high refractive index (> 2.5), strong biocompatibility, and other favourable properties such as chemical stability, non-toxicity, and excellent optical transparency. Its optical properties, such as its band gap (approximately 3.2 eV for anatase and 3.0 eV for rutile), photonic localisation, “slow photon” effect, super prism effect, and negative refraction effect (light bending opposite to the normal direction), have garnered a lot of attention. rendering it beneficial for plastics, paints, and coatings. In sunscreens and self-cleaning surfaces, it is a semiconductor with strong UV absorption that is water-insoluble and resistant to acids and bases [64,65].

Inverse opal TiO₂ photocatalysts are fabricated using various bottom-up techniques, such as the sol-gel method, ALD, electrodeposition, and vapour-liquid methods with an opal template, resulting in a material with a 3D periodic structure and excellent optical properties. The general procedure for preparing TiO₂ IOPCs involves using colloidal crystal templates, where materials like silica, PS or PMMA are arranged into an opal template via methods such as gravity sedimentation, centrifugal sedimentation, self-assembly, evaporation, or dip coating. The resulting IO structure has a large specific surface area (50–150 m²/g), and the optical properties of PCs [66–68].

ALD represents a relatively recent advancement in vapor deposition techniques, offering a unique approach to thin film growth. This method relies on the sequential introduction of gaseous precursors into a reaction chamber, separated by inert gas purges. Film deposition occurs through self-limiting surface reactions between these precursors and the

substrate surface. This layer-by-layer growth mechanism provides exceptional control over film thickness, uniformity, and conformality, even on complex three-dimensional structures. Particularly, ALD has emerged as a powerful tool for the fabrication of IO TiO₂ and its composite structures, leveraging its precise deposition capabilities to create intricate and highly ordered architectures. In ALD of TiO₂ synthesis (Fig 2.2 a-c), the typical titanium precursors utilized encompass titanium tetrachloride (TiCl₄) and a range of titanium alkoxides, notably titanium isopropoxide and titanium ethoxide, while the oxygen source is most commonly H₂O, although alternative oxidants such as O₃ or O₂ plasma can be employed to tailor the resulting film characteristics and process parameters [37,69,70].

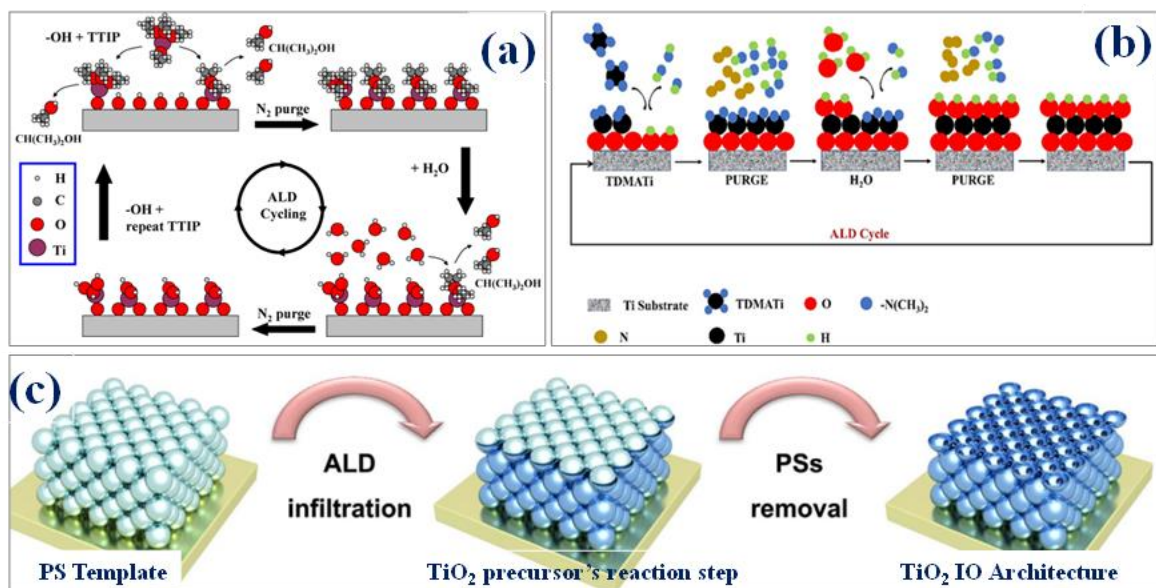


Figure 2.2: Schematic representation of TiO₂ synthesis via ALD using various precursors: (a) titanium isopropoxide and H₂O [69], (b) tetrakis(dimethylamino) titanium (TDMATi) and H₂O [70], and (c) the ALD-synthesized TiO₂ IO structure [37].

TiO₂ IOPCs can be modified chemically or physically to enhance their performance and provide new capabilities. Modification techniques for compost forms include semiconductor composites, noble metal deposition, non-metal components or metal ion doping, and quantum dot sensitisation. The modification of TiO₂ IOPCs is a crucial step toward broadening their applications across various fields, including chemical sensors, solar cells, and photocatalysis. Noble metal deposition is a prominent modification method, as it can enhance the optical properties and catalytic activity of TiO₂ IOPCs. For instance, depositing noble metals like Au, Pt, or Ag nanoparticles onto the TiO₂ IO surface can improve the efficiency of photocatalytic processes by facilitating charge separation and enhancing light absorption.

Zulfiqar et al. detailed a method for fabricating TiO₂ IO structures involving the self-assembly of colloidal particles, followed by TiO₂ precursor infiltration and calcination. To enhance photocatalytic activity, Au nanoparticles were introduced by immersing the TiO₂ IO structures in an Au nanoparticles solution (Fig. 2.3a) [71]. In a separate study, Birnal et al. synthesized TiO₂-Au composite IOs and planar films using ALD with direct liquid injection, where ALD was used for TiO₂ deposition and preformed Au nanoparticles were injected (Fig. 2.3b). This process involved depositing a thin TiO₂ layer after the Au nanoparticles deposition and a final annealing step to remove the template and crystallize the TiO₂ [72]. Lei et al. reported that Ag nanoparticle-decorated spherical TiO₂ IOs were synthesized using extraction-assisted microemulsion self-assembly and a wet-chemical method. The resulting Ag-decorated TiO₂ maintained its microstructure, showed a reduced band gap (~2.6eV), and exhibited improved photocatalytic activity (1.7 times higher) compared to pristine TiO₂ IOs. These Ag-decorated TiO₂ IOs demonstrated enhanced photodegradation of MB and showed effective inhibition of photogenerated charge recombination, highlighting their potential for photocatalysis [73]. Furthermore, TiO₂ IO structures were fabricated via infiltration and functionalized with Au, Ag, and Au/Ag core-shell metal nanoparticles (Fig. 2.3c). Their photocatalytic activity, assessed through the gas-phase conversion of acetylene to CO₂, showed enhanced performance in all metal-functionalized structures, with the gold-silver core-shell nanoparticle-decorated TiO₂ IO exhibiting the most significant improvement [67].

Non-metal elements or metal ion doping is an effective strategy to modify the properties of TiO₂ IOPCs. The introduction of elements such as N, F, or metal ions can alter the electric band structure of TiO₂, thereby enhancing its response to visible light and improving its performance in photocatalysis and solar cell applications. For example, Hu et al. reported a method for fabricating N-doped TiO₂ IO films using a one-step co-assembly of polymer colloidal spheres and a titania precursor. This approach eliminates the need for preassembled colloidal crystal infiltration and separate chemicals for titania formation and nitrogen doping. The resulting films, produced with an optimized amount of titanium (IV) bis(ammonium lactato) dihydroxide, exhibited enhanced visible light photocatalytic activity, demonstrating their potential in applications such as environmental purification, water photoelectrolysis, and dye-sensitized solar cells [74]. Furthermore, Xu et al. developed a new and simple method to fabricate N-F-codoped TiO₂ IO films with a hierarchical meso-macroporous structure using a liquid phase deposition process with a silica colloidal crystal template. The resulting N-F-codoped TiO₂ IO films demonstrated a significantly higher MB visible-light photodegradation

rate, achieving a rate 6.6–7.4 times greater than that of similarly doped films without the inverse opal structure, which underscores the profound efficacy of this synergistic modification strategy[75].

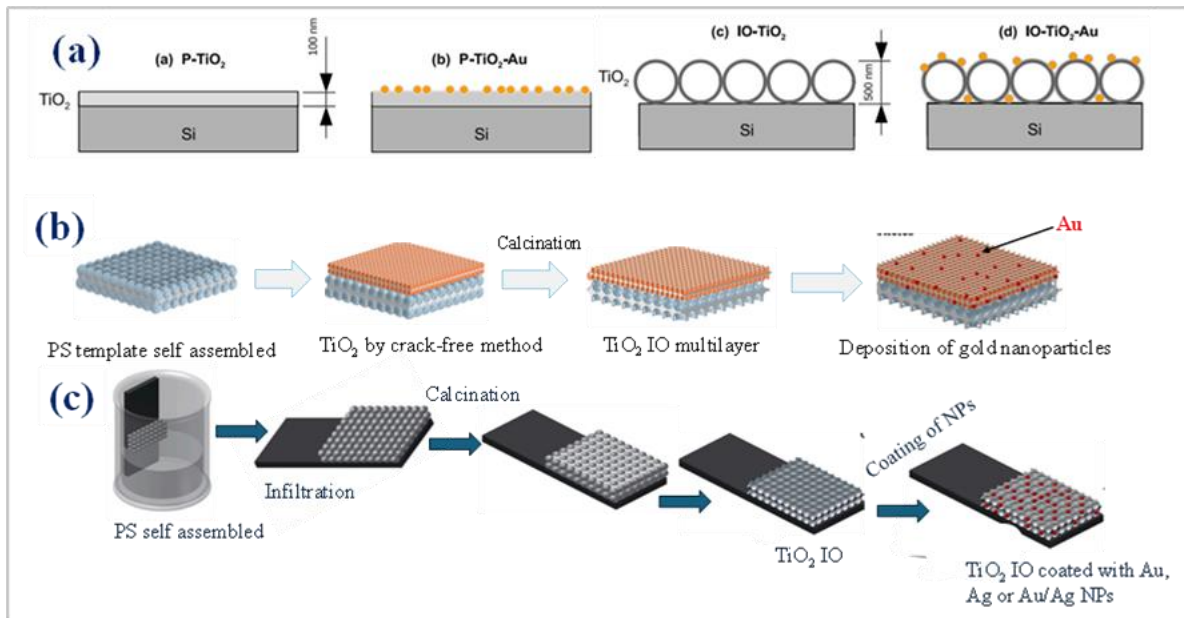


Figure 2.3: Schematic representation of the fabrication of TiO_2 IO decorated with metal nanoparticles (a-b), TiO_2 IO/Au, and (c) TiO_2 IO decorated with Au and Ag [68,71,76].

2.5. ZnO Inverse Opal

ZnO, particularly in its IO form, has garnered significant attention in photocatalysis due to its advantageous physical and chemical properties. Its low cost, straightforward synthesis, chemical stability, and low toxicity render it an environmentally friendly option for large-scale applications. Besides its photocatalytic capabilities, ZnO is a promising optoelectronic material with potential as a short-wavelength light source, owing to its wide bandgap (3.37 eV at room temperature) and high exciton binding energy (~60 meV), both of which enable efficient emission in the near-UV region. Although its refractive index (~2.2) is not sufficient for creating a complete omnidirectional PBG, it can still facilitate directional pseudogaps. Furthermore, ZnO benefits from high electron mobility, which supports the rapid transfer of photon-generated electrons to its surface, thereby enhancing photocatalytic performance. When structured into IOs, ZnO attains additional advantages, such as a higher specific surface area and enhanced photocatalytic activity compared to bulk or non-structured ZnO, along with improved light harvesting through PC effects, making these structures highly promising for environmental and energy-related photocatalytic applications [77–80].

Among various techniques for synthesizing ZnO IOs, ALD stands out as the most common and effective method. ZnO synthesized via ALD exhibits exceptional uniformity, conformality, and atomic-level thickness control, making this technique particularly suitable for applications demanding precise nanoscale engineering. The synthesis process is governed by alternating, self-limiting surface reactions between vapor-phase precursors, enabling layer-by-layer film growth with sub-nanometer accuracy (See Fig. 2.4). The selection of suitable precursors is critical to achieving high-quality ZnO. Zinc precursors commonly employed in ALD include diethylzinc (DEZ) and zinc acetylacetonate, while water is typically used as the oxygen source. These precursors must fulfill several fundamental criteria: they must possess adequate volatility at the deposition temperature to allow efficient vapor transport, undergo irreversible chemisorption on the substrate surface, and avoid thermal decomposition or incorporation into the growing film matrix [81,82].

ZnO synthesized via ALD is particularly advantageous for fabricating complex nanostructures, such as IOs, due to the method's ability to uniformly coat high-aspect-ratio and three-dimensional substrates. Furthermore, using alternative oxidants such as ozone (O_3) or oxygen plasma provides additional degrees of control over film composition, crystallinity, and electronic properties, broadening the applicability of ZnO films in advanced electronic and optoelectronic devices. Experimental studies have validated the precision and tunability of ZnO films grown by ALD. For example, Boyadjiev et al. reported the successful deposition of ultrathin ZnO layers (~20 nm) using DEZ and H_2O as precursors, achieving nanometer-scale control over thickness, which is essential for gas sensing applications [83]. In another study, ZnO quantum dots were deposited onto graphene substrates via ALD, with film thickness varied between 2 and 7 nm by modulating the number of deposition cycles. Such fine control is critical in optimizing performance in lithium-ion battery anodes [84,85].

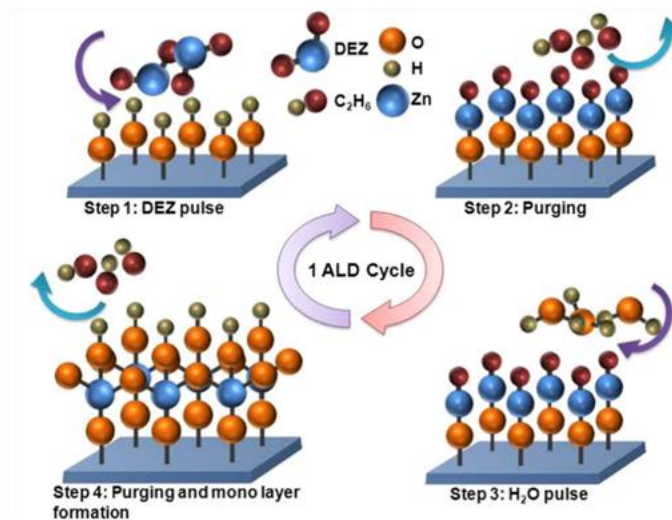


Figure 2.4: Representation of one ALD cycle (ZnO) with the sequential precursor exposure [86].

Combining ZnO IO architectures via ALD emerged as a highly effective strategy to enhance photocatalytic performance, particularly under UV illumination. ALD provided unparalleled precision in tuning the thickness, crystallinity, and uniformity of ZnO films, enabling their conformal coating onto polymer sphere templates to produce ordered porous IO structures. These photonic architectures leveraged “slow photon” effects and high surface areas to boost light harvesting and photocatalytic activity. Long et al. demonstrated that ZnO IOs fabricated via ALD and subsequent annealing exhibited tunable optical properties and superior UV-driven degradation performance. The formation of ZnO/TiO₂ (Fig. 2.5) heterostructures via ALD further improved efficiency by facilitating effective charge separation, making them promising candidates for environmental remediation applications such as water purification and pollutant degradation [33].

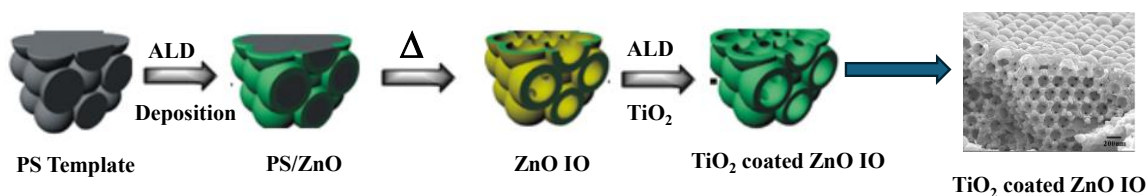


Figure 2.5: Fabrication of ZnO-IO conformally coated by multi-step ALD deposition [33].

Beyond IO architectures, various fabrication approaches such as bilayer nanofilms [87], hybrid nanosheets [88], and nanowire arrays [89], broadened the functional versatility of ZnO-based photocatalysts. Techniques like low-temperature ALD on electrospun sacrificial layers

allowed to production of ultrathin nanofilms, with bilayer ZnO/TiO₂ structures showing the highest activity due to efficient spatial charge separation [83]. Hydrothermal growth on ALD-seeded substrates yielded vertically aligned ZnO nanowires, which were enhanced by integrating noble metals or sulfides for better stability and performance [90]. Additionally, ALD enabled uniform deposition on complex 3D substrates, including sponges, membranes, and opal crystals, greatly expanding the range of photocatalytic designs. ZnO heterostructures in various morphologies, especially with materials like Ag, Cu₂O, or Mn₃O₄, exhibited tailored properties[91–93]. Optimization of layer thickness and the use of co-catalysts such as Pt further elevated performance, while magnetic components like Fe₂O₃ cores allowed easy recovery without compromising catalytic efficiency [94,95].

2.6. Al₂O₃ Inverse Opal

Al₂O₃, commonly called alumina, is a vital ceramic material known for its multiple polymorphic forms and broad industrial utility. Among these, the thermodynamically stable α -Al₂O₃ (corundum) phase stands out due to its exceptional mechanical strength, superior thermal and chemical stability, and resistance to corrosion and oxidation. These attributes make it ideal for use in abrasives, refractories, electronics, and protective coatings. Meanwhile, metastable phases such as γ -, δ -, and θ -Al₂O₃ exhibit high surface areas and pronounced catalytic activity, making them well-suited as catalysts, catalyst supports, and adsorbents. However, these metastable forms tend to irreversibly convert to the stable α -phase at high temperatures (~1100 °C), often resulting in pore collapse and diminished catalytic performance [96,97].

A more advanced iteration of this material, the Al₂O₃ IO, combines the advantageous properties of alumina with a highly ordered, 3D porous framework. Typically fabricated via colloidal crystal templating followed by infiltration and thermal processing, these structures exhibit periodic mesoporous or macroporous architectures. In the α -Al₂O₃ form, the IO structure not only preserves thermal stability but also enhances photonic and catalytic properties due to its interconnected pores and robust framework. These characteristics render Al₂O₃ IOs highly promising for applications in photonic crystals, sensors, catalysis, and high-temperature membranes, owing to their structural order, porosity, and thermal resilience[98–100].

Studies showed that, based on the combined SEM and XRD analyses (Fig. 2.6 and 2.7, respectively), a clear correlation was observed between the microstructural evolution of the alumina inverse opals and their crystallographic phase transitions during heat treatment. After

template removal by calcination at 500 °C for 30 minutes, the structure exhibited a well-ordered, shell-like macroporous network corresponding to an amorphous alumina phase, as confirmed by the absence of crystalline peaks in the XRD patterns. Sintering at 1200 °C for 1 hour initiated the γ - to α -Al₂O₃ phase transformation, while the SEM images showed that the macroporous architecture largely remained intact, with only faint surface features marking the onset of α -phase formation. Further heating at 1400 °C for 8 hours led to the development of these features into a vermicular, porous network through neck growth and grain boundary elimination, yet the ordered framework retained its structural integrity without significant collapse or densification. The XRD results corroborated this evolution, revealing a sequential phase transition from amorphous or boehmite alumina to γ -Al₂O₃ around 1000 °C and finally to the thermodynamically stable α -Al₂O₃ (corundum) phase at 1200 °C [101,102].

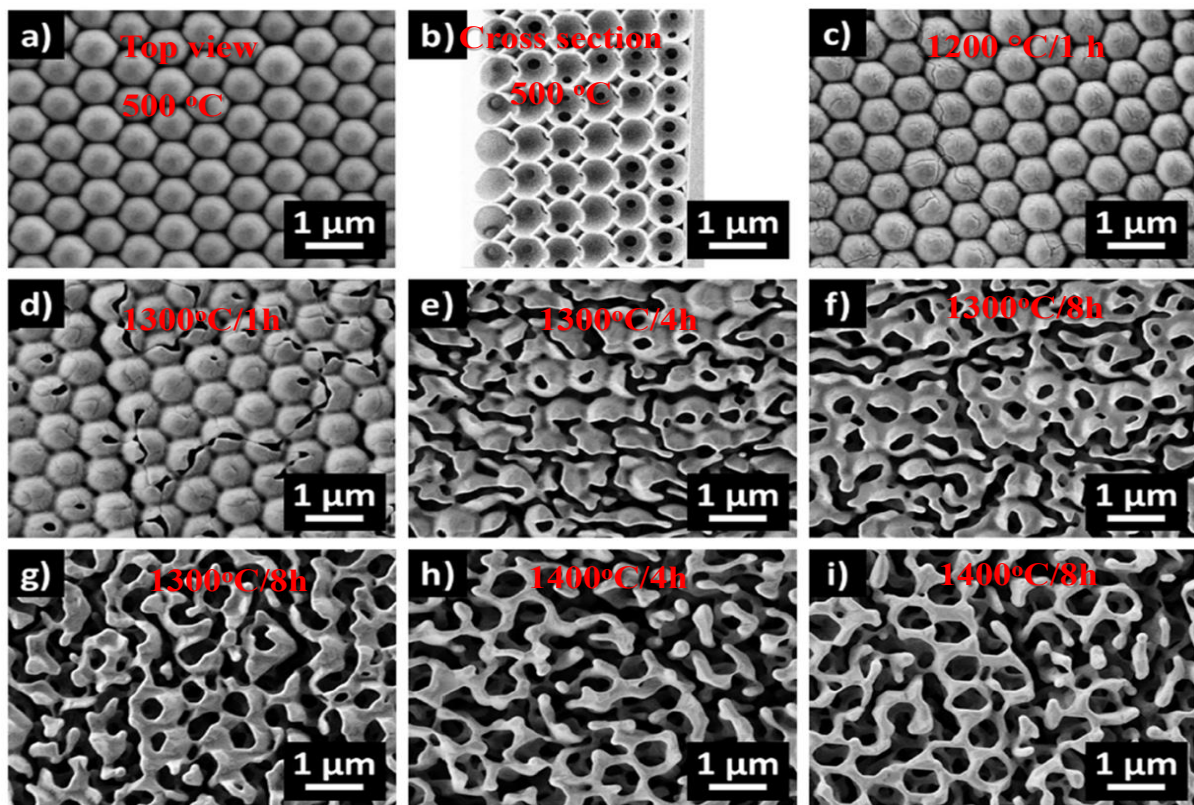


Figure 2.6: SEM images of Al₂O₃ as a function of heat treatment [101].

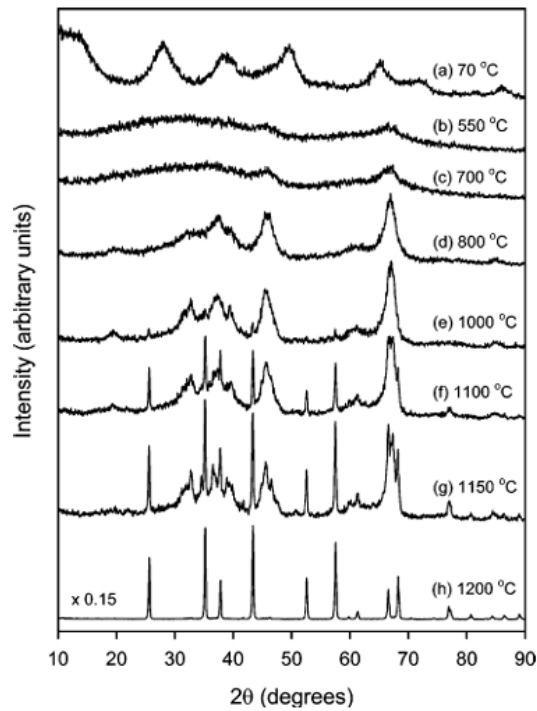


Figure 2.7. XRD shows γ - Al_2O_3 shows precursor (boehmite)[102].

Al_2O_3 has emerged as a versatile material, commonly utilized as a coating or dopant on various surfaces, including those of materials and inverse opals, due to its exceptional properties that enhance performance across a wide range of applications. A prominent approach in this context is the infiltration of Al_2O_3 into silicon IOs using ALD, as reported by Gallego-Gómez and colleagues. This technique was designed to passivate silicon nanocrystals, addressing PL instability induced by surface defects [103]. Similarly, Coll et al. explored the use of Al_2O_3 as a supporting layer in IO fabrication, where conformal deposition via ALD at low temperatures preserved template integrity [104]. In a related study, Graugnard and collaborators demonstrated the application of Al_2O_3 as a sacrificial buffer layer in the fabrication of non-close-packed inverse opals [105]. Furthermore, Al_2O_3 has been utilized in various applications. Lopez et al., used ALD to create $\text{Al}_2\text{O}_3/\text{ZnO}$ multilayers with tunable optical properties for UV optoelectronics [106]. Nasr et al., [107] and Zhang et al. [99] enhanced optical, structural, and photocatalytic performance by doping ZnO with Al_2O_3 .

2.7. Applications of Inverse Opal Materials

2.7.1. Photocatalysis

Photocatalysis uses light to drive chemical reactions for various applications, including water purification. IOPCs are emerging as promising materials in this field with their unique properties. These crystals possess a unique structure and light-manipulating properties that make them photocatalytic. Their highly porous and interconnected network offers a large surface area for reactants to interact with, facilitating efficient mass transfer. Additionally, the "slow photon" effect within the structure increases light absorption and interaction with the material, boosting the efficiency of photocatalytic reactions. These features make them promising for various applications like water purification, pollutant degradation, and hydrogen production [108–111].

Extending this concept, F-centers (or color centers), anion vacancies within the crystal lattice that trap one or more electrons, further enhance photocatalytic activities through defect engineering. Based on the number of trapped electrons, they are classified as F-centers (one electron), F^+ -centers (partially filled), and F_2^+ -centers (vacant). These defect states act as active sites influencing light absorption, charge separation, and electron transfer dynamics. Specifically, F-centers enable visible-light absorption by promoting electron excitation from defect levels to the conduction band, while F^+ -centers aid in charge carrier trapping to suppress recombination losses. F_2^+ -centers, on the other hand, function as electron acceptors that improve redox balance during photocatalytic reactions. These F-center variations fine-tune the electronic structure and surface reactivity of oxide-based photocatalysts such as TiO_2 , ZnO , and CeO_2 , optimizing their efficiency under visible-light-driven photocatalytic conditions [85,112,113].

2.7.2. Photocatalytic Dye Degradations

Photocatalytic dye degradation utilizes light and a catalyst to break down organic dyes. IOPCs with a periodic air void structure have emerged as promising photocatalysts due to their unique properties [114,115]. Several studies have explored the effectiveness of IOs for dye degradation: Birnal et al. investigated IO TiO_2 and found them to achieve the highest degradation rate (90% in 10 hours) for MB dye under UV light compared to planar and rutile TiO_2 . This is attributed to their high surface area and PC properties, highlighting their potential for wastewater treatment [68]. Besides, Bakos et al. also utilized carbon nanospheres for the first time to create titania IOPC materials for degrading organic dyes. This method offered

higher thermal stability and easier removal compared to conventional methods, suggesting the potential for visible-light-driven photocatalysis [116]. Wang et al. fabricated IO SnO₂ and found it to be significantly more effective (1.4 times) than conventional SnO₂ in degrading Rhodamine B dye under visible light. This is due to its larger surface area, facilitating adsorption and mass transfer, and its narrower bandgap, enhancing light absorption. This work emphasized the promise of IOs for developing efficient photocatalysts for various pollutants [117].

Meng et al. also investigated the impact of pore size and the “slow photon” effect on photocatalytic degradation using 3D inverse opal Zinc oxide photonic crystals (ZnO-PCs). They found that the rate constant is influenced by the competition between surface area and mass transport, while the “slow photon” effect enhances photocatalytic efficiency when pollutants are absorbed by the ZnO-PCs (See Fig. 2.8a). This study provides valuable insights for developing advanced functional materials [41]. Zalfani et al. studied TiO₂ nanocomposites decorated by ZnO quantum dots (ZnO QDs@3DOM TiO₂) and found them to significantly enhance photocatalytic activity for RhB dye degradation compared to pure three-dimensionally ordered microporous (3DOM) TiO₂. This is due to the synergistic effect of quantum size effects and the 3DOM structure, promoting efficient separation of photogenerated electron-hole pairs and enhancing light absorption [28].

A study developed a two-step process to fabricate ZnO/TiO₂ IO for efficient degradation of MB. The ZnO/TiO₂ composite IO exhibited the highest activity due to suppressed electron-hole recombination and improved chemical stability. Additionally, the activity increased with increasing IO wall thickness due to a larger catalyst amount and enhanced light scattering. This method offers a promising approach to environmental remediation [118]. Another study investigated the photocatalytic degradation of acetylene using multi-compound IO structures functionalized with AuNPs. These structures, made from TiO₂, TiO₂-SiO₂, and TiO₂-ZrO₂, showed high activity (See Fig. 2.8b) under UV light, especially in the presence of gold nanoparticles (AuNPs). Additionally, AuNPs enabled activity under visible light [76].

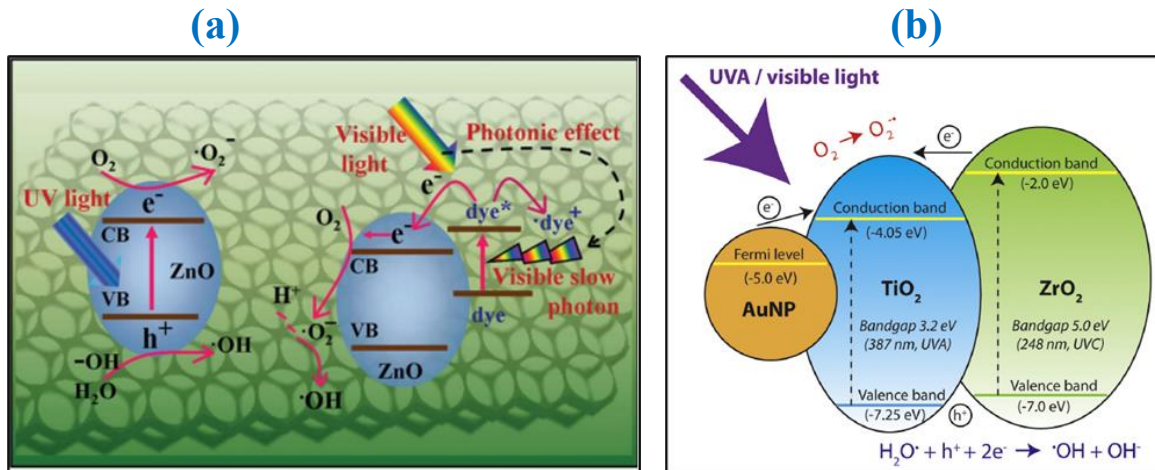


Fig. 2.8: Schematic representation of photocatalytic processes, (a) Under UV light, ZnO-PC directly absorbs light, exciting electrons (e^-) and creating holes (h^+) for photocatalysis (left). Under visible light, dye molecules (RhB or MB) absorb light, inject excited electrons into ZnO-PC, and participate in photocatalysis (right) [41] and (b) Photocatalytic activity in AuNP TiO_2/ZnO IO structure [119].

2.7.3. Photocatalytic Water Splitting

Photocatalytic water splitting is a promising method to generate clean energy from sunlight. However, materials like metal oxide semiconductors (ZnO , TiO_2 , WO_3 , $\text{Fe}_2\text{O}_3\dots$) suffer from low efficiency due to limited light absorption and fast recombination of charge carriers. Researchers are exploring solutions like film coatings, doping, noble metals deposition, semiconductor recombination, and material integration to improve efficiency and overcome these limitations. ZnO-based structures, particularly IOs, are promising options for enhanced performance. This study demonstrates the effectiveness of using ALD to fabricate ZnO IOs with superior performance compared to traditional methods. Additionally, protective layers of TiO_2 and $\text{TiO}_2/\text{Al}_2\text{O}_3$ improve the stability of these structures [120–123].

The synthesis of IO photoelectrodes for photoelectrochemical water splitting utilizes templating methods like colloidal crystal templating to create highly porous, three-dimensional architectures that enhance light absorption, charge separation, and transport. Zhou et al. developed Mo-doped BiVO_4 IO structures using a controllable colloidal crystal template method, improving conductivity and increasing the active surface area, leading to significantly enhanced photocurrent density. Similarly, studies have shown that materials such as Mo-doped BiVO_4 and Bi_2WO_6 benefit from the “slow photon” effect and superior light-harvesting properties, further boosting solar-to-hydrogen conversion efficiency. Additionally, a 3DOM

CsTaWO_{6-x}N_x IO photoanode synthesized via a templating method, followed by nitridation and intercalation with a boron-doped carbon nitride layer, achieves a high photocurrent density of 4.59 mA cm⁻² at 1.6 V vs. reversible hydrogen electrode and demonstrates excellent stability. These advancements highlight the potential of engineered IO-based photoelectrodes for sustainable and efficient photoelectrochemical water splitting [124–126].

Another study successfully integrated a graphene layer into iron oxide (α -Fe₂O₃) photoanodes, significantly boosting their water-splitting efficiency. This graphene layer acts as both an electron pathway and a barrier against the electrolyte, reducing recombination and improving electron transport [127]. Finally, combining TiO₂ and tantalum oxynitride (TaO_xN_y) in an IO structure resulted in a photoanode with significantly enhanced water-splitting performance. This improvement is attributed to the formation of a specific type of junction that optimizes light absorption, charge separation, and overall efficiency [128].

2.7.4. Biological Application of IOPC

IOPC materials have gained significant attention for their diverse biological applications, particularly in biosensing and biomedical diagnostics. Chen et al. synthesized TiO₂ IOs using a PS colloidal template, followed by ALD, calcination, and subsequent loading of Au nanoparticles via a hydrothermal redox approach (Fig. 2.9). The resulting biosensor exhibited a red shift in the reflection peak upon binding of L-cysteine and Avidin, facilitating highly sensitive biomolecule detection. Both experimental and finite difference time domain simulation results confirmed the characteristic optical response of the Au/TiO₂ system, achieving a detection limit of 200 nM for Avidin with a clear linear relationship between peak shift and concentration. This cost-effective, highly sensitive optical biosensor holds great promise for biomolecule detection [129]. In a related development, Xie et al. fabricated 3D ZnO/CuO IOs using a PMMA template, followed by sol-gel infiltration and calcination. These ZnO/CuO IO sensors demonstrated superior acetone gas sensing capabilities, with an optimal Zn/Cu ratio of 1:1, yielding a response 1.4–2.4 times higher than other sensor configurations and a detection limit of 100 ppb. The sensors also exhibited excellent selectivity, stability, and resilience under high humidity, making them particularly suitable for non-invasive diabetes diagnosis through exhaled breath analysis. The improved sensing performance was attributed to the formation of p-n heterojunctions and the 3D IO structure, which enhanced gas diffusion and electron transport, underscoring the potential of ZnO/CuO IO composites for practical breath-sensing applications [130].

Expanding the scope of IOPC applications, Yan et al. developed an advanced electrochemical biosensor array for multiplex cancer biomarker detection, integrating in situ self-assembled carbon nanotubes within a 3D IO framework. The biosensor was fabricated using microdroplet-based microfluidics, nanoparticle self-assembly, and chemical wet-etching techniques, allowing precise control over pore size and structural stability. It exhibited exceptional sensitivity and accuracy in detecting C-reactive protein, carbohydrate antigen 125, and carcinoembryonic antigen in human serum, achieving low detection limits as low as 0.005 ng/mL for C-reactive protein. Performance validation against commercial methods demonstrated its potential for point-of-care testing and early disease diagnosis, emphasizing its high throughput, rapid response, and clinical applicability [131].

Jiang et al. introduced an approach for enzyme immobilization by embedding glucose oxidase and organophosphorus hydrolase into silica IOs using water-soluble polyacrylamide colloidal crystal templates (Fig. 2.10 a & b). The resulting enzyme-containing silica IOs exhibited remarkable stability against extreme pH, temperature, and chemical denaturants, outperforming free enzymes in terms of durability and functionality. The Glucose oxidase-containing silica inverse opals (GOD@SiOs) showed high sensitivity and selectivity for glucose detection, while the organophosphorus hydrolase-containing silica inverse opals (OPH@SiOs) effectively detected organophosphorus compounds. This environmentally friendly, in situ enzyme immobilization strategy holds significant potential for biosensors, bioanalytical devices, and enzyme catalysis, expanding the utility of IOPC materials in biomedical and environmental applications [132].

Further advancing optical biosensing, Wang et al. employed silica colloidal crystal thin films as templates to fabricate polystyrene IO films through a filling and etching process. A comparative study of silica colloidal crystal, polystyrene-silica colloidal crystal composite, and IO films demonstrated the IO film's superior response to refractive index variations and biomolecular interactions. Notably, IO films exhibited enhanced sensitivity, higher protein adsorption capacity, and improved mass transport efficiency, attributed to their 3D interconnected porous structure. The significantly broader detection range (0.5–1000 $\mu\text{g/mL}$) and increased sensitivity for biomolecular interactions suggest that IO films present considerable advantages for label-free biosensing, paving the way for advancements in optical interferometric biosensor technology [133].

Collectively, these studies highlight the versatility of IOPC materials in biosensing, diagnostics, and biomedical applications. Their unique porous architectures, high surface area, and tunable optical properties offer remarkable advantages for detecting biomolecules, gases, and disease biomarkers, reinforcing their potential for next-generation sensing technologies.

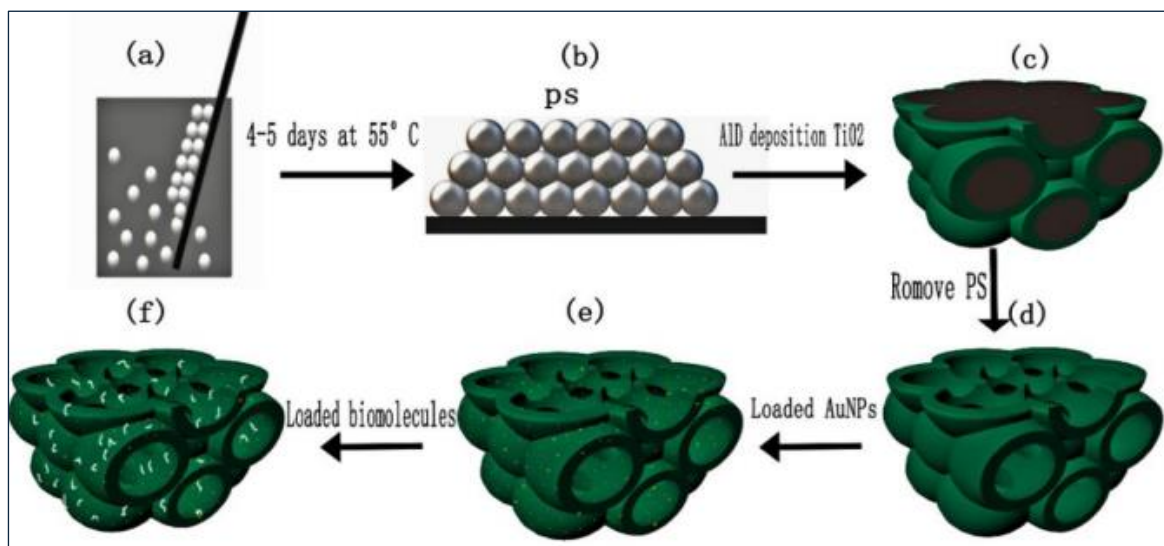


Figure 2.9: PS microspheres were deposited on the indium tin oxide glasses by the vertical self-assembly method for biosensor applications [129].

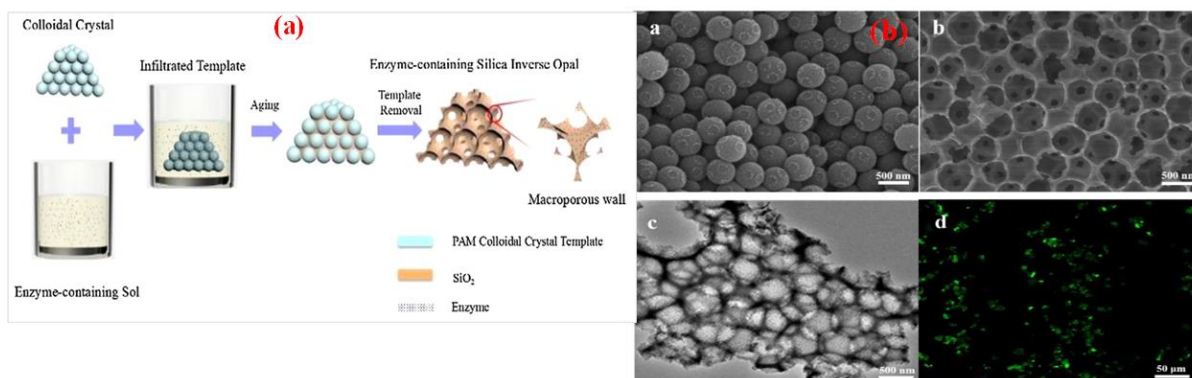


Figure 2.10: (a) Schematic illustration of the preparation of an enzyme-containing silica IOs, and (b); (a) SEM micrograph of polyacrylamide microspheres (PAM), (b) SEM, (c) TEM, and (d) confocal laser scanning microscopy micrograph of the enzyme-containing silica IOs [132].

3. KNOWLEDGE GAP

Despite remarkable advances in the design and synthesis of IOPCs, significant research gaps still limit their full potential in photocatalytic applications. Most existing studies focus on photocatalysts that operate effectively only under UV light irradiation, which represents a small portion of the solar spectrum. In contrast, the development of IOPC systems that can efficiently utilize visible light, the dominant and more practical portion of sunlight, remains limited. This under exploration restricts their relevance for real-world, solar-driven environmental and energy applications.

Even though IOPCs show great promise for enhancing light absorption and charge transport, these improvements often do not result in better photocatalytic performance. This gap is mainly due to limited control over internal material properties, including the presence of structural defects, weak interfaces between oxide layers, and rapid recombination of photo-generated charge carriers before they can drive chemical reactions. In addition, achieving structural precision and uniform composition in complex IOPC architectures remains a major challenge. While advanced fabrication techniques such as TALD and PEALD enable precise coating, their different impacts on photonic–electronic interactions, band alignment, and charge transfer are not yet fully understood. Similarly, the effects of template size, coating thickness, and multi-layer configurations such as $\text{TiO}_2/\text{ZnO}/\text{Al}_2\text{O}_3$ composites on the balance between UV and visible-light activity are not systematically explored.

Most current studies remain confined to laboratory settings, with limited attention to large-scale fabrication, long-term durability, and cost-effectiveness. To bridge these gaps, future research should integrate precise structural design, compositional control, and advanced hybrid ALD techniques to create stable, defect-tolerant, and visible-light-active inverse opal photocatalysts suitable for real-world environmental and energy applications.

4. EXPERIMENTAL METHODS

4.1. Aims of the Experiments

This chapter briefly overviews the experimental methodology used for fabricating, characterizing, and analyzing nanostructured, porous IOs from various semiconductor oxides, such as TiO_2 , ZnO , and Al_2O_3 , and their composites, using different ALD techniques to improve photocatalytic performance. PS nanosphere sacrificial templates of 300 nm, 460 nm, and 600 nm were constructed using VLD to achieve periodic, ordered, and porous IO structures. Additionally, the goal was to control the self-assembly of colloidal particles to formulate regular template fabrication as a scaffold for later semiconductor oxide ALD. Moreover, several synthesis pathways were employed to optimize template order, morphology, and structural integrity, including the use of PS suspensions and powders.

Pure IOs of TiO_2 , ZnO , and Al_2O_3 were successfully synthesized, followed by ultrathin ALD coatings to create composite IOs such as $\text{TiO}_2/\text{Al}_2\text{O}_3$, $\text{ZnO}/\text{Al}_2\text{O}_3$, TiO_2/ZnO , and ZnO/TiO_2 , employing both TALD and PEALD for Al_2O_3 and ZnO . Both TALD and PEALD techniques were successfully employed in the synthesis of IO materials. Finally, the photocatalytic performance of all synthesized IOs, including those with varying PS template sizes and composite structures, was evaluated through the degradation of MB, Rh6G, and 4-NP under UV and visible light irradiation.

4.2. Preparation of PS Nanosphere Opal Sacrificial Template

4.2.1. Materials Used

PS nanosphere suspensions purchased from Sigma Aldrich with different particle sizes (300 nm, 460 nm, and 600 nm) were used in the study for synthesizing opal sacrificial templates. VLD was used to create these templates using Knittel Glaser microscope glass slides and a silicon wafer. Ion exchange water served as the oxidizing agent for the deposition procedures, which used precursors such as titanium tetrachloride (TiCl_4), diethylzinc (DEZ), and trimethylaluminum (TMA) for TiO_2 , ZnO , and Al_2O_3 , respectively. Using pollutants such as MB, Rh6G, and NP that were acquired from Sigma-Aldrich, the photocatalytic degradation tests evaluated the photocatalytic performance of the synthesized materials.

4.2.2. Preparation of the template from the PS suspension

The opal template was prepared from PS suspension (Sigma Aldrich, 10% w/w and 300 or 600nm particle size) after being diluted to achieve a concentration of 3.0 % (V/V) by transferring 0.15 mL PS suspension to a 5 mL flask and placed in a closed glass container to avert its evaporation and ultrasonicated for 2h at 35°C to separate the aggregated nanospheres. Microscope glass slide (Knittel Glaser, ca. 76 x 26 mm, Germany) was used as a planar substrate, cleaned first with soap, ethyl alcohol, and ion exchange water (Fig. 4.1a). This substrate was soaked in piranha solution (a mixture of 98% (v/v) H₂SO₄ and 30 % (w/w) H₂O₂ in a 3:1 ratio) for 1h to remove any organic residue on the glass surface and to make it more hydrophilic. The clean glass slides were placed in the PS suspension at a 45-degree angle to achieve the successful vertical deposition self-assembly of colloidal particles. They were placed in the furnace at 50°C for 14h, so the colloidal crystal could form during the evaporation of the water through colloidal self-assembly, and was finally heated to 80°C for 90 min. The schematic representation of the whole experimental procedure is shown in Fig. 4.1 a and b below.

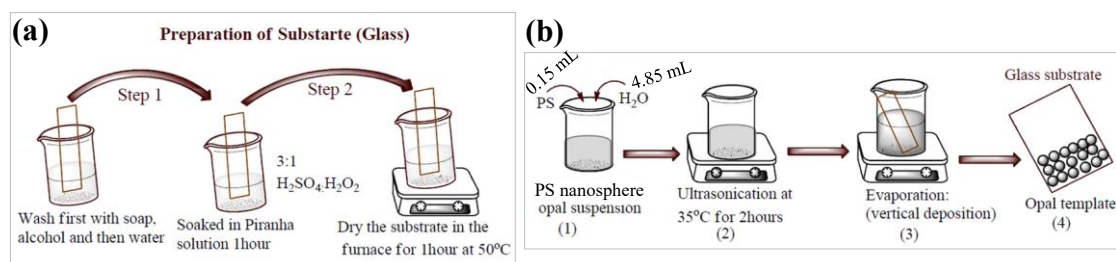


Figure 4.1: (a) Glass substrate preparation involves cleaning with soap, ethyl alcohol, and water, followed by soaking in piranha solution and drying in a furnace, and (b) Opal template synthesis starts with diluting PS nanosphere suspension, ultrasonication, vertical deposition onto the glass substrate, and drying to form the opal structure.

4.2.3. Preparation of the Template from PS powder

The preparation of a PS suspension (Sigma Aldrich, 600 nm, 10%) commenced with gently scraping powder from the PS bottle using a curved-end spatula. Subsequently, 15 mg of PS powder was mixed with 4.85 ml of ion exchange water and thoroughly stirred manually until a homogeneous dispersion was achieved (Fig. 4.2). To enhance particle uniformity and surface area, the suspension underwent high-frequency sonication treatment using Sono Plus equipment (Bandelin ultrasound, DIN EN 62638, Germany) with the following parameters: amplitude 30%, pulsation time 0.5 seconds, energy 6.1 kJ, and duration 3 minutes at ambient

temperature (25 ± 2 °C). Finally, the prepared PS suspension was utilized to grow an opal layer on a microscope glass slide using the VLD method, in line with our previous study protocol.

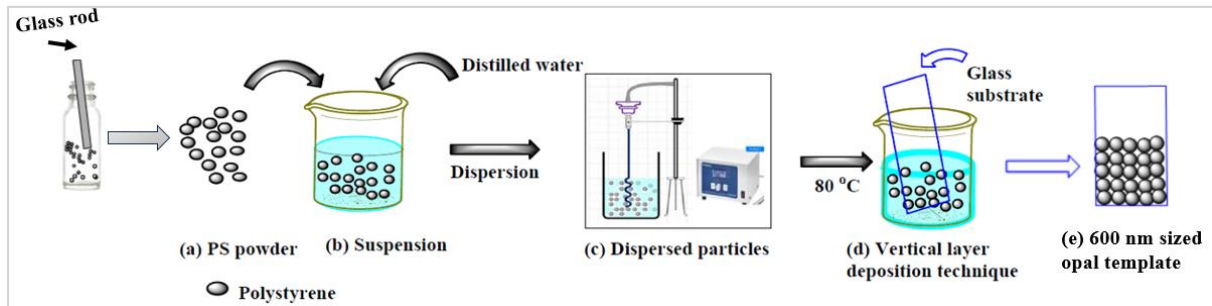


Figure 4.2: Illustrates the fabrication of a PS nanosphere template on a glass substrate: (a) PS powder is scraped, (b) suspended in water, (c) dispersed (3 min), (d) deposited onto glass via VLD at 80 °C, resulting in (e) a 600 nm sized opal template.

4.3. Thin Film Deposition Using ALD Methods

In this study, I successfully fabricated IOPC materials using two ALD thin film coating techniques: TALD and PEALD. PEALD used plasma to increase reactivity and provide more exact control over film characteristics at lower temperatures, while TALD simply used thermal energy to induce surface reactions. The ALD deposition parameters for TiO₂, ZnO, Al₂O₃ layers, and their composites are summarized in Tables 4.1 and 4.2. All ALD experiments were conducted using a Beneq TFS-200-186 ALD reactor. For the deposition processes, TiCl₄, DEZ, and TMA were used as precursors for TiO₂, ZnO, and Al₂O₃, respectively, with H₂O serving as the oxidizing agent. For example, in the case of TiO₂ layer, each ALD cycle comprised a 0.3 s TiCl₄ pulse, followed by a 3 s N₂ purge, a 0.3 s H₂O pulse, and a subsequent 3 s N₂ purge. These depositions were carried out at a controlled temperature of 52.9°C in thermal mode.

Table 4.1: TiO₂ IO coated with an ultrathin layer of Al₂O₃ TALD and PEALD

Sample Name	Deposited oxide layer	Modes of ALD reaction	ALD cycles	Thickness (nm)	ALD (pulse/purge)	Steps	GPC (nm)
TiO ₂ IO	TiO ₂	TALD	671	51.6	TiCl ₄ , N ₂ , H ₂ O, N ₂		0.07
TiO ₂ /Al ₂ O ₃ -T	Al ₂ O ₃	TALD	7	5	TMA, N ₂ , H ₂ O, N ₂		0.71
TiO ₂ /Al ₂ O ₃ -P	Al ₂ O ₃	PEALD	9	5	TMA, N ₂ , Ar, N ₂		0.55

Table 4.2: ZnO IO coated with an ultrathin layer of Al₂O₃, TALD and PEALD

Sample Name	Deposited oxide layer	Modes of ALD reaction	ALD cycles	Thickness (nm)	ALD Steps (pulse/purge)	GPC (nm)
ZnO IO	ZnO	TALD	539	51.4	DEZ, N ₂ , H ₂ O, N ₂	0.09
ZnO/Al ₂ O ₃ -T	Al ₂ O ₃	TALD	19	4.4	TMA, N ₂ , H ₂ O, N ₂	0.23
ZnO/Al ₂ O ₃ -P	Al ₂ O ₃	PEALD	23	5.5	TMA, N ₂ , Ar, N ₂	0.23

4.3.1. PEALD Film Growth

The low-temperature PEALD deposition technique applied plasma species as a co-reactant to enhance precursor reactivity, resulting in the growth of high-quality films [134]. The process commenced with preheating the ALD chamber to 50°C for 2 hours to ensure uniform substrate heating. Subsequently, the samples and a reference silicon wafer were placed in the PEALD reactor to initiate film growth, with the wafer positioned beside each sample to accurately determine the final film thickness. A consistent 50 W radio frequency power was applied to the plasma during PEALD to activate the O₂ oxidant. Argon was the carrier gas used to deliver oxidant vapor and metallic precursors to the reactor. The vacuum chamber and deposition reactor maintained internal pressures of 7.4 mBar and 1.2 mBar, respectively.

The PEALD process involved alternating pulses and purges of reactant gases, using N₂ as the purging agent. For TiO₂ deposition, the sequence comprised a 0.15 s TiCl₄ pulse, followed by a 2 s N₂ purge, a 2 s Ar plasma exposure, and another 2 s N₂ purge. This cycle was repeated 286 times to achieve a 30 nm thick film, with a growth rate of 0.10 nm per cycle. For ZnO deposition, a modified sequence using DEZ and O₂ resulted in a 10 nm film after 74 cycles, at a GPC of 0.13 nm. Additional ZnO samples were fabricated using DEZ and water, or with TiO₂ grown on top of ZnO layers. Further details are summarized in Table 4.3.

Table 4.3: TiO₂, ZnO IOs and their composite (TiO₂/ZnO and ZnO/TiO₂) using PEALD

Sample Name	Deposited oxide layer	Modes of ALD	ALD cycle	Thickness (nm)	ALD Steps (pulse/purge)	GPC (nm)
TiO ₂ IO	TiO ₂	TALD	286	30	TiCl ₄ , N ₂ , Ar, N ₂	0.10
TiO ₂ /ZnO	ZnO	TALD	74	10	DEZ, N ₂ , Ar, N ₂	0.13
ZnO IO	ZnO	TALD	221	30	DEZ, N ₂ , Ar, N ₂	0.13
ZnO/TiO ₂	TiO ₂	TALD	96	10	TiCl ₄ , N ₂ , Ar, N ₂	0.10

Table 4.4: Al₂O₃ IO coated with an ultrathin layer of TiO₂, and ZnO using ALD methods

Sample Name	ALD Mode	Thickness (nm)	ALD cycle	ALD Steps (pulse/purge)	GPC (nm)
Al ₂ O ₃ IO	TALD	36	133	TMA, N ₂ , H ₂ O, N ₂	0.27
Al ₂ O ₃ /ZnO-T	TALD	5	55	DEZ, N ₂ , H ₂ O, N ₂	0.09
Al ₂ O ₃ /ZnO-P	PEALD	5	37	DEZ, N ₂ , Ar, N ₂	0.13
Al ₂ O ₃ /TiO ₂ -T	TALD	5	52	TiCl ₄ , N ₂ , H ₂ O, N ₂	0.09
Al ₂ O ₃ /TiO ₂ -P	PEALD	5	48	TiCl ₄ , N ₂ , Ar, N ₂	0.10

4.4. Heat Treatment of the Samples: Annealing and Post-Annealing

The heat treatment process involved placing both the samples and reference samples (silicon wafer) into alumina ceramic crucibles to remove the template material. The process was carried out in a furnace (Nabertherm L9/11/B410, Germany) under ambient air conditions. In the heating program, the samples were heated from ambient temperature to 500 °C for 4 hours and then maintained at that temperature for 2 hours. After the PS template was effectively eliminated, the resultant structure comprised a high-quality pristine IO structure. Additionally, post-annealing was performed at 500 °C for TiO₂, ZnO, and their composites after an extra layer had been deposited on the surface of the IO structures, facilitating the formation of the final IO architecture (See Table 4.5).

On the other hand, Al₂O₃ IO samples were annealed in an alumina crucible under ambient air using a thermogravimetric analysis optimized program: heated from room temperature to 450 °C over 4 hours, held for 30 minutes to remove the PS template, then raised to 900 °C for 1 h and held for 2 h to complete template removal and optimize the structure (see Table 4.5 below).

Table 4.5. Annealing program for all IO samples

IO samples	Temperature (°C)	
	Template removal (°C)	Post annealing (°C)
TiO ₂	500	500
ZnO	500	500
Al ₂ O ₃	450	900

4.5. Material Characterization

4.5.1. Thermal Analysis by TG/DTA-MS

For the PS opal sample, thermal analysis was carried out with a TA Instruments SDT 2960 simultaneous thermogravimetry/differential thermal analysis/derivative thermogravimetry (TG/DTG/DTA) device, in an air atmosphere with a heating rate of 10°C/min and a flow rate of 130 cm³/min until 600°C simulating the environment during the removal of the PS nanospheres. The evolved gaseous products were identified with a thermostat GSD 300 Balzers Instruments type quadrupole mass spectrometer (MS) coupled online to the TG/DTA device. The selected ions were followed in multiple ion detector modes. For the measurement, the thin PS film was scratched off from the glass surface and collected into the Pt crucibles.

4.5.2. FTIR Analysis

Fourier transform infrared (FTIR) spectra of PS opal templates were acquired using a PerkinElmer Spectrum 2000 FT-IR spectrometer at a resolution of 4 cm⁻¹, scanning from 4000 to 400 cm⁻¹. Samples were prepared as KBr pellets and subjected to 64 co-added scans.

4.5.3. Morphological and Cross-Sectional Analysis by SEM and TSEM

The SEM images were taken with an FEI Inspect S50 scanning electron microscope in a low-vacuum system, using a backscattered electron detector. The samples were examined

without any modification or treatment, and no conductive film (Au and Pd) was deposited on the samples to avoid possible signals due to their interference.

The SEM analysis was performed utilizing a JEOL JSM-5500LV scanning electron microscope operating at 25 kV with an SEI Detector under high vacuum conditions. The samples were observed without any modification or treatment, and no conductive film (Au and Pd) was applied to prevent potential signal interference. EDX spectra were captured using the JEOL JSM-5500LV SEM, with three measurement points taken for each sample and an average of them.

The cross-sectional morphological analysis of the Transmission Scanning Electron Microscope (TSEM) was analyzed using a SCIOSTM 2 Dual Beam™ FIB-SEM (Thermo Fisher Scientific), equipped with an Everhart-Thornley detector and a field emission gun source. This system featured advanced electron optical components, including an annular in-column detector. For STEM analysis, high-angle annular dark-field mode and a TSEM+ detector were used, with the specimen tilted at 38°. The horizontal field width was set to 1.92 µm. To mitigate charging effects on uncoated samples, a reverse bias of 20 V was applied to the specimen holder.

4.5.4. Atomic Force Microscopy

The surface roughness and morphology of the samples were characterized using atomic force microscopy (AFM) with a Nanosurf C3000 controller. The AFM images and root mean square (RMS) values were obtained and analyzed using Gwyddion version 2.64 software.

4.5.5. Compositional Analysis By EDX

EDX analysis was performed using a JEOL JSM-5500 LV SEM operating at 25 kV. SEM imaging of the PS template samples was conducted after sputter-coating with an Au/Pd alloy to prevent charging by providing a conductive surface. The EDX spectra from all ALD samples were utilized for element identification, with three measurement points taken for each sample and the results averaged.

4.5.6. XRD Structural Analysis

The structural analysis was performed using a PAN analytical X'Pert Pro Monochromatic Parallel-Beam Powder XRD with Copper K-alpha ($\lambda=1.540 \text{ \AA}$) radiation, in the 2-Theta (5–70 °). The resulting patterns were compared to the International Centre for

Diffraction Data database to identify crystalline phases. The mean size of the crystallites, D , was determined with the Scherrer equation:

$$D = \frac{K\lambda}{\beta \cos\theta} \quad (3.1)$$

Where K is the constant, λ is the wavelength of the radiation, β is the full width of diffraction peaks at half-maximum (FWHM), and θ is the angle at which the peak occurs (Bragg angle).

4.5.7. Raman Structural Analysis

The Raman structural analysis was done using a Jobin Yvon Labram Raman spectrometer equipped with an Olympus microscope and a green Neodymium-doped Yttrium Aluminum Garnet laser. The Raman shift (in wave number) was measured within the range of 100 to 1800 cm^{-1} .

4.5.8. UV Visible is Optical Analysis and Photonic Band Gap Estimation

The samples were UV Visible spectroscopically analyzed using an AvaSpec-2048 spectrometer from AVANTES, equipped with an Ava Light-DHS deuterium halogen lamp. Ava Soft software was used for absorbance-reflectance-mode data acquisition.

The PBG of the IO materials has been estimated by using a modified Bragg's equation (3.2), shown below:

$$\lambda_{\max} = 1.632D (n_{\text{avg}}^2 - \sin^2\theta)^{1/2} \quad (3.2)$$

Where λ_{\max} is the wavelength of the band maximum (PBG) of the materials, D is the diameter of spheres (would generally be taken as $2r$, where r is the sphere radius), θ is the angle between the incident light and the surface of the sample. The average refractive index n_{avg} of the samples can be calculated using the following equation (3.3):

$$n_{\text{avg}} = f_{\text{sphere}}n_{\text{sphere}} + (1 - f_{\text{sphere}})n_{\text{air}} \quad (3.3)$$

Where f_{sphere} is the filling factor, representing the proportion of space occupied by the solid PS spheres within the overall structure. For a face-centered cubic lattice, the volume fractions of PS spheres and air f_{air} is typically 74 % and 26 %, respectively. Additionally, n_{PS} , n_{ZnO} , $n_{\text{Al}_2\text{O}_3}$, and n_{air} represents the refractive indices of PS, ZnO, Al_2O_3 , and air, respectively. The refractive indices are: $n_{\text{PS}} = 1.59$, $n_{\text{ZnO}} = 2.0$, $n_{\text{Al}_2\text{O}_3} = 1.7$, and $n_{\text{air}} = 1.0$.

Using the Tauc relation (equation 3.4) and Kubelka-Munk theory, electric band gap energies (E_g) of IOs TiO_2 , ZnO, and their composites were calculated from absorption data (α)

and photon energy ($h\nu$). For indirect E_g (TiO_2) and direct E_g (ZnO) and their composites, Tauc plots $(\alpha h\nu)^{1/2}$ vs. $h\nu$ and $(\alpha h\nu)^2$ vs. $h\nu$ were made. The band gap energy was obtained by extrapolating the linear portions of the plots to $(\alpha h\nu)^{1/n} = 0$.

$$(\alpha h\nu)^n = A(h\nu - E_g) \quad (3.4)$$

4.5.9. Ellipsometry Thickness Analysis

A SEMILAB Spectroscopic Ellipsometer SE-2000 (Cambridge, USA) was utilized to measure the thickness of the IO films and reference samples. To ensure accurate measurements, reference Si (100) wafers were integrated as control samples in the ALD system along with the opal and IO samples.

4.5.10. Photoluminescence Spectra Analysis

Photoluminescence (PL) spectra were recorded using an Edinburgh Instruments FS5 spectrofluorometer with a stationary fluorescence setup, employing excitation wavelengths of 280 nm and 380 nm at room temperature (25°C), and including a long pass glass filter in the emission beam, set at nominal wavelengths of 320 nm and 380 nm, respectively.

4.5.11. X-ray Photoelectron Spectroscopy Measurement

The XPS measurements were conducted using an XR 50 dual-anode, non-monochromatized X-ray source and a Phoibos 100 MCD-5 hemispherical energy analyzer by SPECS (Berlin, Germany). Samples were mounted onto copper sample holders using double-sided adhesive tape and degassed in the high vacuum of the sample loading chamber ($\sim 10^{-7}$ mbar) overnight before being transferred into the spectrometer. The base vacuum of the instrument was maintained at 5×10^{-10} mbar. During the measurements, samples were cooled with liquid nitrogen, and the pressure remained below 10^{-8} mbar. Spectra were acquired sequentially using Al K_α radiation (1486.6 eV) with an acceleration voltage of 10 kV and an emission current of 10 mA (100 W X-ray power). The binding energy scale was calibrated using the Au 4f and Cu 2p peaks of a freshly cleaned reference sample containing both metals, as per the manufacturer's instructions. Charge referencing was performed using the C 1s peak of carbon (284.8 eV), which is rightfully considered untrustworthy, as detailed in [135] and some other works from these authors, however, in our case the spectra were mainly used for confirming the elemental composition in the samples, which does not require truly rigorous charge correction. Data processing was carried out using CasaXPS software.

4.5.12. Photocatalytic Activity Measurement

To evaluate the photocatalytic performance of samples, they were subjected to both UV and visible light irradiation while immersed in solutions containing different pollutants such as MB, 4-NP, and Rh6G for 4 hours. The pH of the 4-NP solution was adjusted to $10.01 \text{ pH} \pm 0.01$ using a buffer (Thermo Fisher Scientific). The MB, 4-NP, and Rh6G solutions exhibited maximum absorbance peaks at 665 nm, 400 nm, and 530 nm, respectively. Each sample was attached to the walls of a glass vessel using plastic tape to ensure that only the film portion was fully submerged in the dye solutions. Before irradiation, the samples were kept in the dark for half an hour to allow adsorption-desorption equilibrium to be established. At regular intervals of 30 minutes, 2 ml of the solution was carefully pipetted into a quartz cuvette, and its absorbance was measured using an Avantes fiber optic spectrometer (AvaSpec-2048) equipped with an Ava Light-DHS light source. The photocatalytic decomposition of the pollutants was initiated by exposing the sample solutions to both UV and Visible light irradiation from Osram 18W blacklight and visible lamps 3x3 arranged in a stack configuration. The sample solution was placed in front of the central lamp and maintained at 5 cm to guarantee uniform lighting conditions. This photocatalytic experimental setup enabled the quantification of the photocatalytic activity of the IO-grown samples over time, providing insights into their efficiency in degrading the pollutants.

4.5.13. Measurement by Doctoral Candidate and Collaborators

I collaborated with BSc and MSc students to develop the synthesis and characterization of various IOPC materials using ALD methods. **Feras Shugaa Addin**, an MSc student, fabricated bare TiO_2 IO and its composites ($\text{TiO}_2/\text{Al}_2\text{O}_3$) from 600 nm-sized PS templates using ALD procedures to enhance photocatalytic activity. Another MSc student, **Nour Khauli**, used ALD methods to synthesize and characterize pure ZnO IO and its composites ($\text{ZnO}/\text{Al}_2\text{O}_3$) from 600 nm PS templates, also aiming to improve photocatalytic activity. **Leticia Tolezani**, a BSc student, synthesized and characterized IOPC materials from a 300 nm sized PS template, including TiO_2 , ZnO, and their composites (TiO_2/ZnO and ZnO/TiO_2), using PEALD techniques for enhanced photocatalytic activity. **Soeun Choi Arwen** synthesized and characterized Al_2O_3 IOPC using 460 nm PS templates with ALD techniques. I characterized the pure and composite IOPCs using SEM/EDX, FTIR, XRD, and UV Visible at the Department of Inorganic and Analytical Chemistry, Budapest University of Technology and Economics. I fabricated a PS opal sacrificial template on specific substrates using vertical deposition, performed annealing after ALD, prepared and characterized IOPC materials (TiO_2 ,

ZnO, Al₂O₃, and their composites), and conducted photocatalytic investigations of these synthesized materials. The students worked under my supervision and that of **Professor Dr. Imre Miklós Szilágyi**, my thesis supervisor.

Gyula Jágerszki from the Department of Inorganic and Analytical Chemistry at Budapest University of Technology and Economics performed the AFM measurements. I then evaluated the results. Raman measurements were done by Tamás Igricz of the Department of Organic Chemistry and Technology, Budapest University of Technology and Economics, and I evaluated the measurement results of Raman. Photoluminescence measurements were done by **Dr. Dóra Hessz** of the Department of Physical Chemistry and Materials Science, Budapest University of Technology and Economics. ALD techniques were performed by **Professor Dr. Zoltán Erdélyi, Dr. Petra Pál, and Dr. Eszter Mónika Baradács** of the Department of Solid-State Physics, University of Debrecen. I then characterized and analyzed the resulting measurements.

Professor Dr. Zoltán Erdélyi (Department of Solid-State Physics, University of Debrecen) and **Tamás Fodor** (HUN-REN Institute for Nuclear Research, Debrecen) performed the XPS measurements. I then evaluated the XPS data. TSEM measurements were conducted by **Professor Dr. Zoltán Erdélyi** and **Dr. Csaba Cserhádi** (Department of Solid-State Physics, University of Debrecen). I analyzed the TSEM data. Spectroscopic ellipsometry measurements were performed by **Professor Dr. Zoltán Erdélyi** (Department of Solid-State Physics, University of Debrecen). I evaluated the analysis of these measurements."

5. RESULT AND DISCUSSION

5.1. Thermal, FTIR, and Morphological Analysis of PS Nanospheres With Various Sphere Size Differences

5.1.1. Thermal Analysis Results

PS opal templates with pore sizes of 300 nm (PS-300) and 460 nm (PS-460) were thermally decomposed under both air and N₂ atmospheres, exhibiting similarities. In both environments, an initial mass loss of approximately 1–2 % occurred up to 200 °C, corresponding to solvent evaporation. The primary decomposition took place between 250 °C and 400 °C. Under air, complete degradation was observed by 600 °C, leaving no residual mass. In contrast, in the N₂ atmosphere, a small amount of carbonaceous residue (1–2 %) remained between 400 °C and 600 °C, indicating char formation.

The PS opal template with a pore size of 600 nm (PS-600) exhibited distinct thermal decomposition behaviors under both air and N₂ atmospheres, with the major mass loss occurring between 200 °C and 400 °C in both environments. Complete decomposition was achieved by 500 °C in air, indicating full oxidation of the polymer. In contrast, under N₂, approximately 7 % residual mass remained at 600 °C, consistent with char formation.

Although the thermogravimetric data showed minor inconsistencies, the overall mass loss in air was higher than in N₂, which aligns with expectations. However, the initial mass loss (at 200 °C) attributed to solvent evaporation was greater under N₂ (e.g., 2.4 % for PS-300) than in air (1.2 %), indicating possible differences in solvent retention or evaporation behavior between the two atmospheres.

5.1.2. FTIR Analysis Results

FTIR analysis was performed to examine the chemical structure, and functional groups present in PS nanospheres of varying sizes (PS-300, PS-460, and PS-600). All samples exhibited a broad absorption band around 3400 cm⁻¹, corresponding to O-H stretching vibrations, indicating the presence of hydroxyl groups on the surface. Peaks near 2920–2925 cm⁻¹ and 2850–2854 cm⁻¹ were observed in all spectra, attributed to C-H stretching vibrations in aliphatic chains. Aromatic C=C stretching bands appeared consistently around 1590–1602 cm⁻¹ and 1490–1493 cm⁻¹, confirming the aromatic nature of the PS backbone. Additional C-H bending vibrations were seen at approximately 1450 cm⁻¹ and 1375–1382 cm⁻¹ across all samples. Distinct features in each sample included a carbonyl stretching peak at 1715 cm⁻¹ in

PS-300, suggesting the presence of C=O groups, while PS-460 and PS-600 exhibited prominent C-O stretching bands between 1015–1103 cm^{-1} , indicating ether or ester functionalities. The presence of hydroxyl groups across all samples suggests enhanced surface hydrophilicity, while the consistent aromatic and aliphatic features confirm the successful formation of PS nanospheres with expected structural characteristics (refer to Fig. 5.1 a-c below).

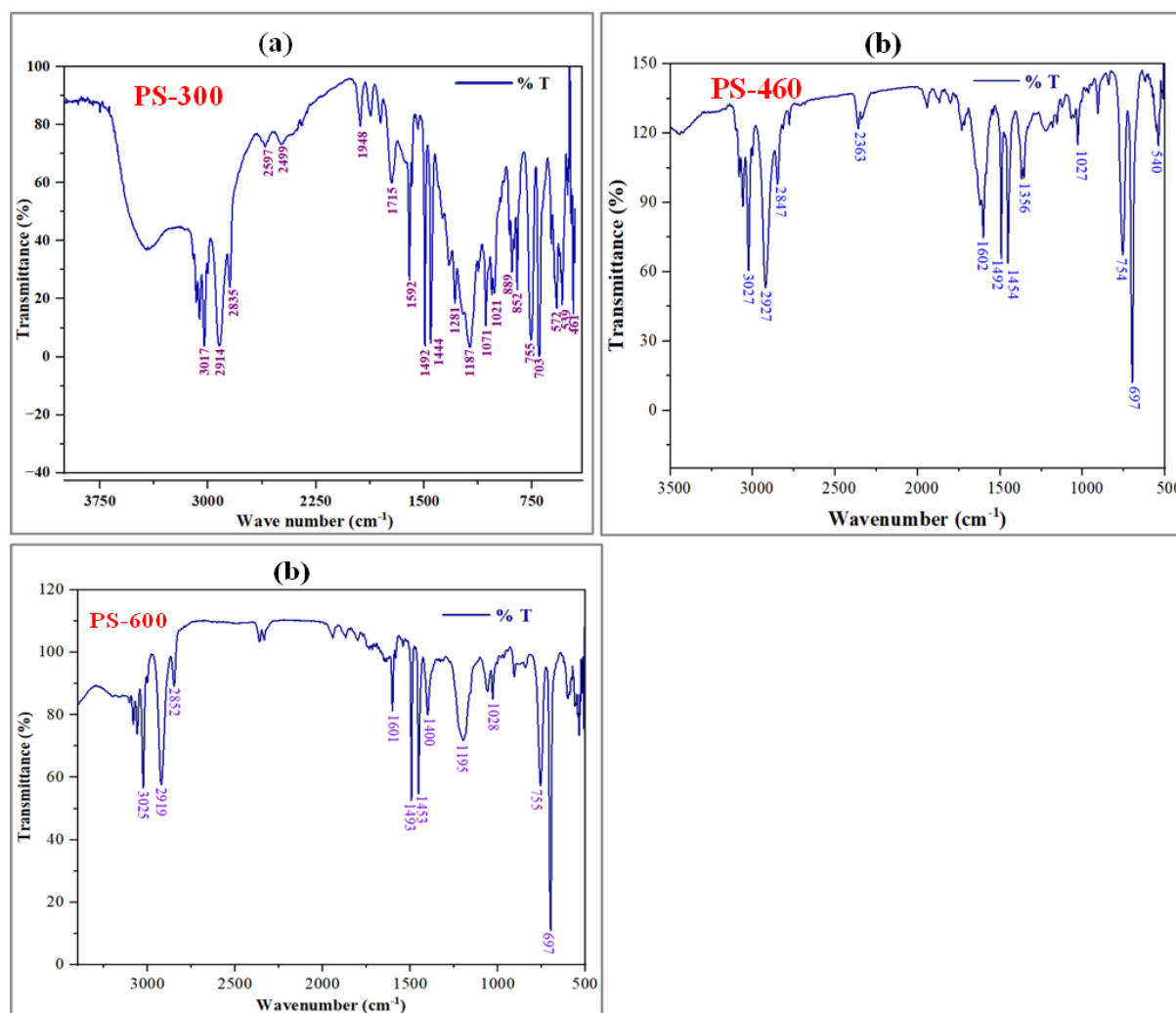


Figure 5. 1. FTIR spectra of PS templates with different particle sizes: (a), PS-460, (b), and PS-600 (c) nanospheres in both air and N_2 atmospheres, respectively.

5.1.3. Morphological Analysis of PS Nanosphere Templates

The colloidal crystal templates, fabricated from monodispersed colloidal spheres, displayed a regular, periodic lattice structure due to van der Waals interactions [32]. As depicted in Fig. 5.2a, the template consisted of an opal macrostructure with a diameter of approximately 290 nm (as determined by SEM). This macrostructure was self-assembled

through vertical deposition methods. The opal spheres exhibited a close-packed hexagonal lattice arrangement, originating from commercially available opal with a nominal diameter of 300 nm. This dense particle packing imparts unique optical and electronic properties to colloidal crystals.

The SEM analysis (Fig. 5.2 b) confirmed the successful synthesis of opal structures from ~460 nm PS nanospheres. These structures showcased an interconnected IO network with periodic arrays and consistent pore sizes. The PS-460 nanosphere template itself displayed regular and compact pores arranged in a hexagonal pattern, a tightly packed structure resembling a honeycomb Fig. 4.3 b presents high-magnification SEM images.

The PS-600 displayed a high-quality colloidal crystal template (Fig. 5.2 c), which was grown using the VLD process and consisted of colloid nanospheres that were approximately 588 nm in size (based on SEM measurements). The (100) planes of the FCC crystal network resembled the periodic arrangement of monodispersed colloidal spheres shown in the top-view SEM pictures. These template structures have shown promising potential as suitable candidates for ALD infiltration techniques

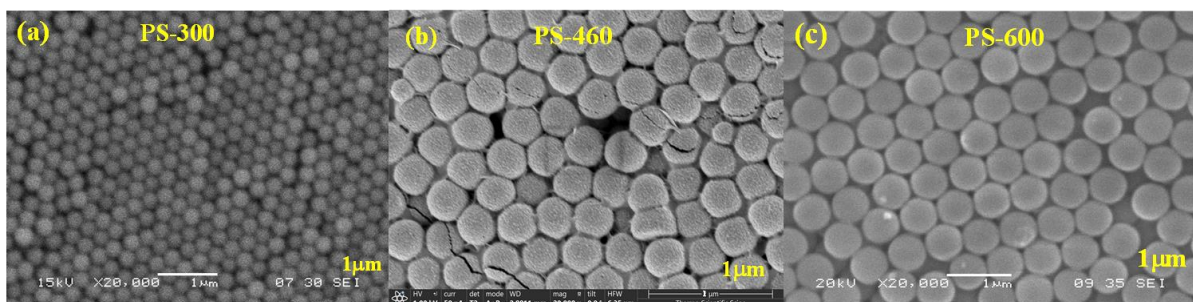


Figure 5.2: SEM images of PS nanosphere templates of varying sizes, (a) 300nm, (b) 460nm, and (c) 600nm, respectively.

5.2. Synthesis of IOs TiO₂, ZnO, and Composites Using PS-300 Template using PEALD Methodology

5.2.1. Morphology & Composition Analysis of IO via PS-300 Template

In this study, I successfully synthesized IO of TiO₂, ZnO, ZnO/TiO₂, and TiO₂/ZnO using PS-300 via the PEALD deposition method. SEM microgram analysis demonstrated an ordered and periodic arrangement of monodispersed colloidal spheres within the IO structures, resembling an FCC crystal lattice. The morphology was honeycomb-like, characterized by interconnected voids that replaced the original colloidal spheres, maintaining the integrity of

the initial template structure post-thermal annealing. SEM identified that cracks were noted in both TiO₂ and ZnO IOs (Fig. 5.3 a & c), with TiO₂ exhibiting a 14 % shrinkage compared to 3.4 % in ZnO. Moreover, the cross-sectional SEM analysis (Fig. 5.3 d) verified the foundation of a consistent and conformal porous network, confirming the complete removal of the PS-300 template. The periodicity and interconnected pores highlight the effectiveness of the PEALD method in preserving the original template structure. Furthermore, the fabricated TSEM micrograms of ZnO/TiO₂ and TiO₂/ZnO (Fig. 5.3 f & g) composites showed a defined periodic lattice with precisely controlled layer thicknesses.

EDX analysis confirmed the successful deposition of TiO₂ and ZnO via PEALD (See APPENDIX K). The table indicated significant amounts of Ti, Zn, and O, confirming the effective formation of the desired metal oxide layers. Trace amounts of C, Na, Al, Si, and Ca were also detected, originating from precursor materials and the glass substrate, but these did not significantly impact the structural or photocatalytic properties of the IO materials.

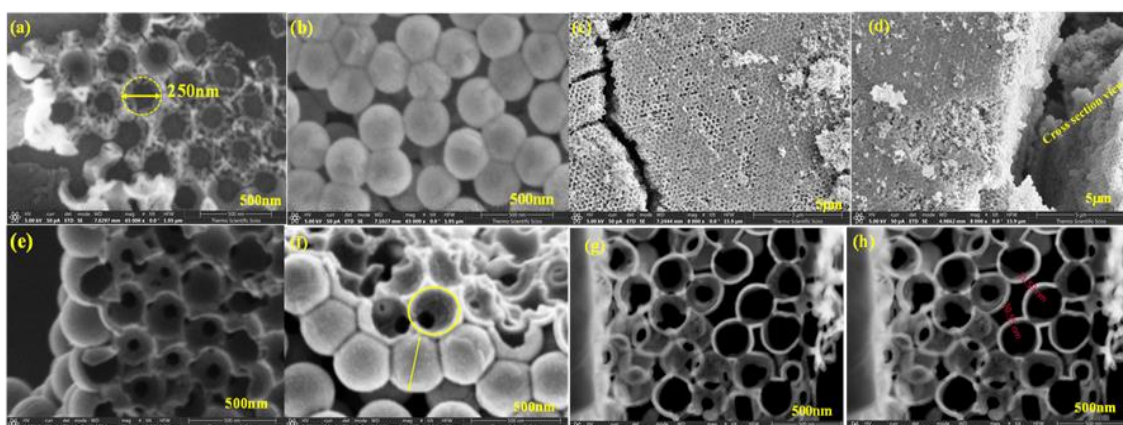


Figure 5.3: Displays SEM images of TiO₂ IO (a, e), ZnO/TiO₂ (b, d), ZnO (c), TiO₂/ZnO (d), and TSEM images of ZnO/TiO₂ (f) and TiO₂/ZnO (g, h), respectively.

5.2.2. Crystalline Structure Analysis: XRD and Raman Analysis

The XRD and Raman analyses examined the crystal structures and vibrational properties of the synthesized materials, including IOs TiO₂, ZnO, and their composites. The XRD pattern (Fig. 5.4 a) of TiO₂ displayed distinct peaks at 25.7°, 38.5°, 48.5°, 54.5°, and 55.6°, corresponding to the anatase phase, confirming the formation of pure IO anatase TiO₂ without impurities or phase transitions. Similarly, ZnO exhibited characteristic XRD peaks at 32.5°, 34.8°, 36.6°, 57.2°, 63.2°, and 68.2°, which can be indexed to the hexagonal wurtzite phase, confirming the successful synthesis of pure wurtzite ZnO IO. The XRD patterns of TiO₂/ZnO and ZnO/TiO₂ composites revealed a combination of peaks from both anatase TiO₂

and wurtzite ZnO phases, indicating heterostructure formation, with slightly broadened and less intense peaks compared to pure TiO₂ and ZnO, likely due to smaller crystallite sizes and the presence of interfaces. The crystallite sizes, estimated using the Scherrer equation, were found to be 27.6 nm for TiO₂ IO and 26.3 nm for ZnO IO, while the composites exhibited slightly reduced sizes of 27.3 nm for TiO₂/ZnO and 25.4 nm for ZnO/TiO₂, suggesting interface-induced grain growth suppression (Table 5.1) [136].

The Raman spectra (Fig. 5.4 b) further confirmed the structural properties, with TiO₂ displaying characteristic vibrational peaks at 142, 197, 393, 516, and 635 cm⁻¹, corresponding to the anatase phase, consistent with XRD results. ZnO exhibited Raman peaks at 333, 440, 574, 986, 1137, and 1352 cm⁻¹, confirming the wurtzite ZnO phase. The Raman spectra of TiO₂/ZnO and ZnO/TiO₂ composites showed peaks from both anatase TiO₂ and wurtzite ZnO phases, validating the heterostructure formation. However, as observed in the XRD results, the Raman peaks were slightly broadened and less intense in the composites, likely due to reduced crystallite sizes and interface effects.

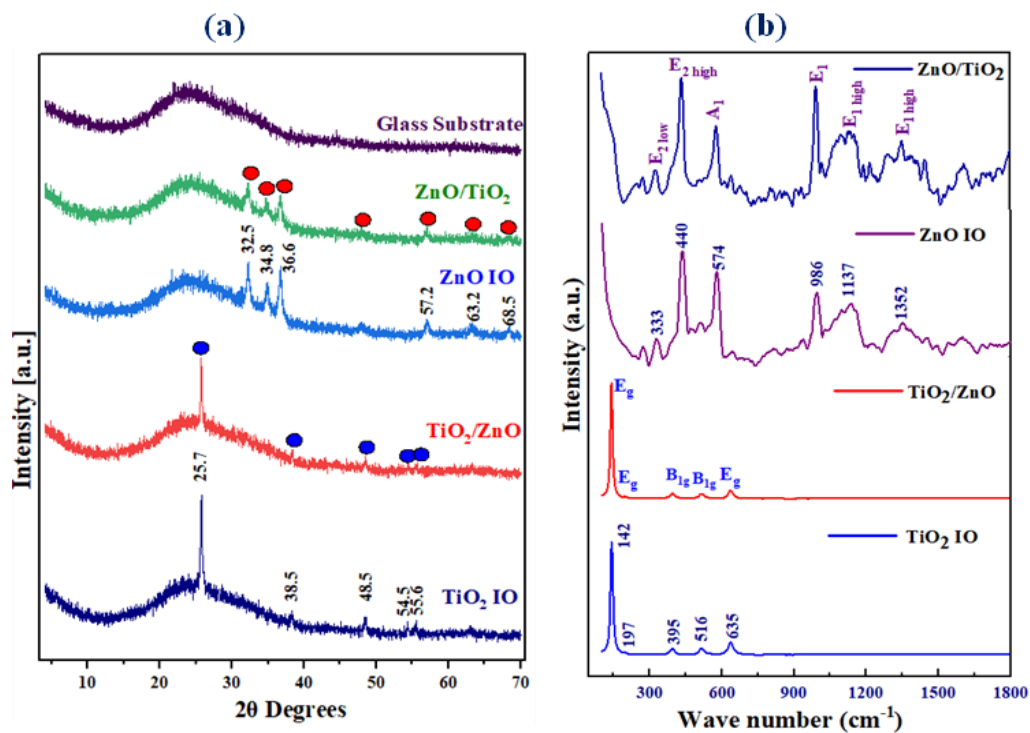


Figure 5.4: (a) XRD and (b) Raman spectroscopy analysis of the PEALD IO samples

Table 5.1. Crystallite size and FWHM analysis of pristine IO materials

Sample	Peak position (2θ °)	FMHW (radian)	Crystallite sizes (nm)
TiO ₂ IO	25.7	0.31	27.6
TiO ₂ /ZnO	25.7	0.32	27.3
ZnO IO	36.6	0.33	26.3
ZnO/TiO ₂	36.6	0.30	25.4

5.2.3. UV Visible Absorption and PL in IO Materials

UV Visible absorption studies of the PEALD IO materials, respectively, with all materials showing enhanced absorption in the UV region. The pure TiO₂ IO shows a broad absorption band, corresponding to its electric bandgap ($E_g=3.0\text{eV}$) [137]. This is attributed to the size-dependent properties of the IO macrostructures. Pores with a size of approximately 290 nm allow for increased light absorption. The pure TiO₂ IO has a PBG around 400 and 630 nm, which coincides with an absorption band at 400 and 610 nm (Fig. 5.5 a). This is likely due to the "slow photon" effect, which can potentially enhance photocatalytic performance. However, the PBG calculated using Bragg's equation is 394 nm, which matches the experimental values. This can be attributed to the consistent periodicity of the IO macrostructures. Additionally, the PBG is highly influenced by the diameter of the spheres used as templates and the angle of light entering the structure. These opals, characterized by a sphere diameter of 290 nm and wider PBG peaks, exhibit greater polydispersity, including pore size variations. The composite TiO₂/ZnO exhibited an absorption spectrum and reflectance spectra identical to the reference TiO₂ IO. The calculated Bragg's PBG (APPENDIX A) matched that of the reference TiO₂ IO. Therefore, the additional PEALD layer on the TiO₂ IO structure did not influence the optical properties of the pure IO. Besides, the composite systems such as TiO₂/ZnO and ZnO/TiO₂ retained PBG, with ZnO/TiO₂ showing a blue shift to 500 nm due to the slight TiO₂ layer modifying influence.

The study applied PL spectroscopy to examine the optical properties of PEALD-grown IOs made from TiO₂, ZnO, and their composite oxides. The results indicated that the IOs exhibited PL only in the visible range. This was because these materials had an electric band gap that corresponded to the energy of visible light. When light of this energy was absorbed by the material, electrons were excited from the valence band to the conduction band. These

electrons could then recombine with holes in the valence band, releasing energy in the form of light [138–140]. Fig. 5.5 b also showed that the pure TiO₂ IO displayed a broad emission spectrum with intense peaks in the violet (430 nm), blue (474 nm), and green (563 nm) regions, suggesting multiple recombination pathways for photogenerated electrons and holes. The high intensity indicated the efficient generation of these species, potentially making it a good photocatalyst [141,142].

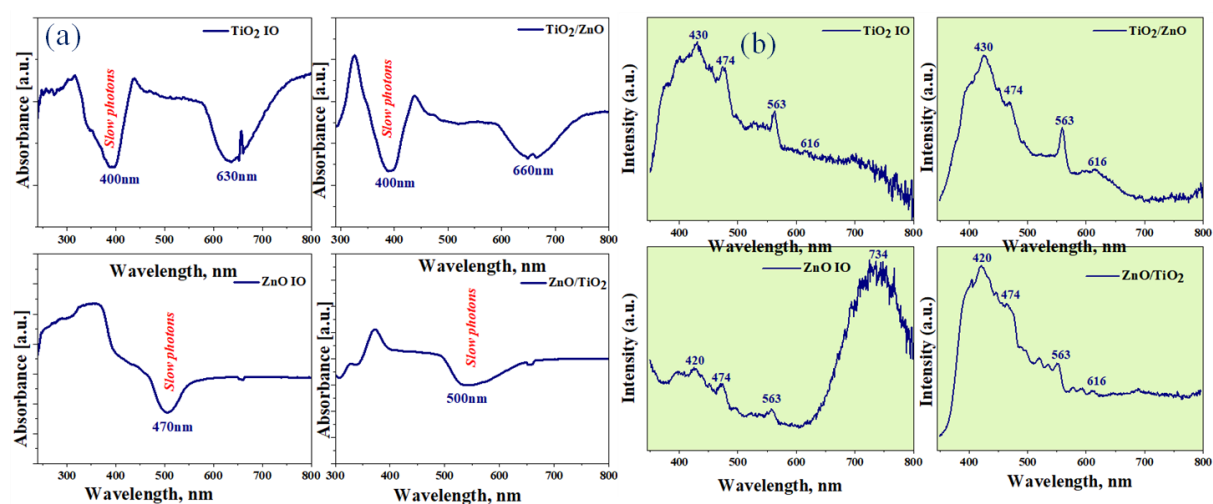


Figure 5.5: (a) UV Visible absorbance spectroscopy, and (b) PL spectroscopy of TiO₂, ZnO, and their composite samples.

4.2.4. Photocatalytic Studies

In this study, all photocatalysts followed pseudo-first-order kinetics. The rate of photodegradation for 4-NP is significantly higher than that for Rh6G under both types of light irradiation after 240 minutes, observed with all IO photocatalysts.

$$\ln[C_0/C_t]=k_{app}t \quad (4.1)$$

where k_{app} is the rate constant. C_0 is the initial concentration of pollutants, and C_t is the concentration after irradiation time t . The linear plots of $-\ln(C_t/C_0)$ versus irradiation time, t , were shown in APPENDIX F, and the calculated rate constants were provided in Table 5.2 and APPENDIX E.

This difference is evident from the k_{app} values for 4-NP, which are consistently higher than those for Rh6G across all light sources. Pristine ZnO IO photocatalyst exhibits a significantly faster rate of 4-NP degradation compared to Rh6G under both UV and visible light irradiation. Specifically, the k_{app} for ZnO IO is 1.9 times faster under UV light and 1.6 times faster under visible light compared to Rh6G. Similarly, pristine TiO₂ IO demonstrated a

1.2 times faster degradation rate for 4-NP ($k_{app}=0.96$) compared to Rh6G ($k_{app}=0.78$) under UV light irradiation within four hours. The composite materials TiO₂/ZnO and ZnO/TiO₂ also showed faster degradation rates for 4-NP than for Rh6G under UV light. Specifically, ZnO/TiO₂ ($k_{app}=0.88$) and TiO₂/ZnO ($k_{app}=0.77$) degraded 4-NP more efficiently.

Pristine IOs show faster degradation rates compared to their composite counterparts (See also APPENDIX D), likely because of their higher surface area, tunable PBG, “slow photon” effect, and efficient charge separation, making IOs a promising photocatalyst material. The pristine IOs have a highly ordered porous IO structure that enhances the interaction between the photocatalyst and the pollutants, leading to more efficient degradation [36,41,143]. In contrast, the composites, while still effective, may have slightly less optimal structural properties for light absorption and pollutant interaction, resulting in a marginally slower degradation rate. Whereas the faster degradation of 4-NP compared to Rh6G can be attributed to the interplay between their chemical structures and light absorption properties. 4-NP's simpler structure, likely lacking the complex conjugated system present in Rh6G, might make it more susceptible to oxidation from the photocatalyst, leading to a higher degradation rate. Additionally, the presence of the nitro group in 4-NP broadens its light absorption range to include some visible light, allowing it to take advantage of both UV and visible irradiation for degradation. The interaction of phenolic intermediates with radicals leads to the opening of the aromatic ring, the cleavage of the carbon chain, and eventually mineralization to form CO₂ and H₂O [144,145]. In contrast, Rh6G primarily absorbs in the visible spectrum. While it can still degrade under UV light, the less efficient overlap between its excitation energy and UV light likely leads to a slower degradation rate compared to 4-NP under both light sources.

Visible light enhances the photocatalytic activity of ZnO/TiO₂ and TiO₂/ZnO composite IOs for Rh6G and 4-NP degradation compared to pristine IOs. The pollutants exhibited a higher degradation rate when using ZnO/TiO₂ and TiO₂/ZnO photocatalysts under visible light. Particularly, the 4-NP exhibited a faster degradation rate with the ZnO/TiO₂ composite IOs. For example, the k_{app} for ZnO/TiO₂ with 4-NP was 1.49, while for Rh6G it was 0.78. Similarly, the rate constant for TiO₂/ZnO with 4-NP was 1.39, compared to 0.60 for Rh6G. This is due to visible light effectively exciting the composite IOs, creating a synergistic effect between bandgap compositing and the PBG effect. This enhanced light trapping and improved charge separation significantly boost the generation of reactive oxygen species, leading to faster degradation of 4-NP compared to pristine IOs (due to slightly less optimal structure) and the more robust structure of Rh6G [146–148].

Table 5.2: k_{app} of the samples, k_{app} [$10^{-2}/\text{min}^{-1}$]

Sample	UV source	Visible source	Sample	UV source	Visible source
4-NP	0.038	0.14	Rh6G	0.05	0.05
TiO ₂ IO	0.96	0.89	TiO ₂ IO	0.78	0.51
TiO ₂ /ZnO	0.77	1.39	TiO ₂ /ZnO	0.50	0.60
ZnO IO	1.07	0.79	ZnO IO	0.56	0.51
ZnO/TiO ₂	0.88	1.49	ZnO/TiO ₂	0.41	0.78

5.2.5. The Photodegradation Mechanism

In this study, I demonstrated that all PEALD IO photocatalysts exhibited the capability to degrade pollutants under UV light, primarily due to their surface area [149,150] and the effects of their PBG. The pristine TiO₂ and ZnO IO materials demonstrated superior performance compared to the composite materials (TiO₂/ZnO or ZnO/TiO₂). This enhanced efficiency in pristine TiO₂ and ZnO can be attributed to their more effective electron excitation under UV light exposure (Fig. 5.6). When UV light interacts with these pristine materials, it excites the electrons, leading to the generation of a greater number of reactive radicals. These radicals play a crucial role in the degradation process, breaking down the pollutant molecules more effectively than the composites [38]. Consequently, the higher efficacy of pristine TiO₂ and ZnO in generating these radicals under UV illumination is a key factor in their superior photocatalytic performance.

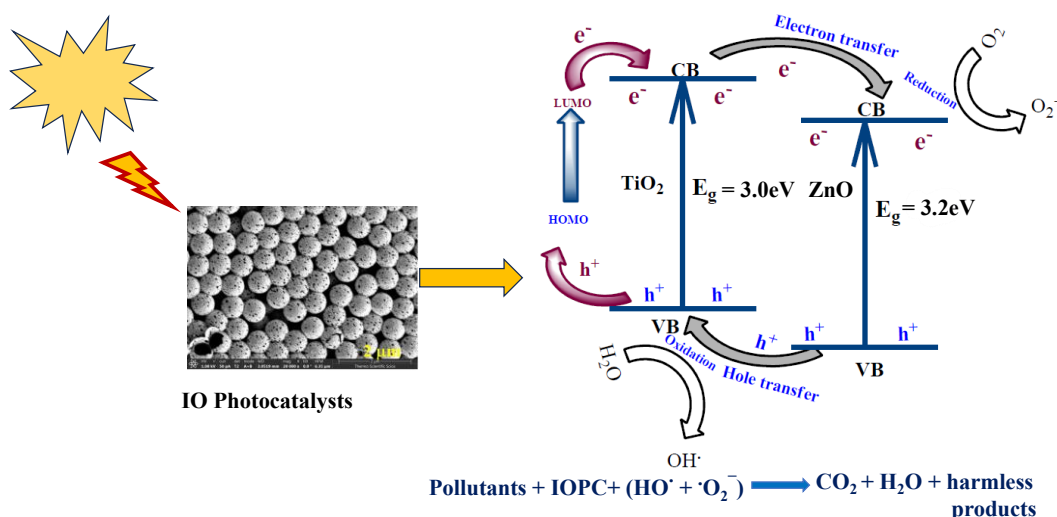


Figure 5.6: Schematic representations of photocatalytic materials: PEALD-IOs of TiO₂ and ZnO for degradation of pollutants under UV light irradiation.

5.3. Thermal and Plasma-Enhanced ALD for the Synthesis of Inverse Opal Al₂O₃ and Its Composite Materials

5.3.1. Morphological Studies by SEM and AFM

The morphological SEM analysis confirmed the successful synthesis of opal structures from ~460 nm PS nanospheres, forming interconnected IO networks with uniform pores in a FCC pattern, Fig. 5.7 a-f below. The Al₂O₃ infiltration via TALD created an IO structure after high-temperature annealing, causing shrinkage and cracks. The SEM microgram measured sphere diameters at ~433 nm with a material thickness of ~39 nm, while ellipsometry suggested ~36 nm. The final FCC-arranged IO structure retained periodicity. The TALD resulted in ~41 nm thickness with 429 nm voids, whereas PEALD increased the thickness (~ 47-48 nm) and reduced void size (~415 nm). Based on the AFM analysis, plasma activation during the PEALD coating resulted in increased surface roughness and reduced film conformality, whereas the TALD method yielded smoother surfaces and more uniform coatings.

Additionally, AFM morphological analysis was conducted to examine surface roughness (See Fig. 5.8 and Fig. 5.9). The AFM results reaffirmed the periodic close-packed structure of IO with a triangular arrangement typical of the FCC (111) plane. The pristine Al₂O₃ IO structure exhibited lower RMS roughness (13.8 nm) than the PS opal template (20.3 nm). The growth of ZnO or TiO₂ layers via TALD and PEALD increased roughness, with TALD consistently producing smoother surfaces (ZnO: 17 nm, TiO₂: 18 nm) than PEALD (ZnO: 19 nm, TiO₂: 20 nm) (See Fig. 5.9). PEALD composites showed a more jagged line profile, indicating a rougher surface. These results highlight the significant impact of deposition techniques and material selection on surface roughness, with TALD exhibiting enhanced smoothness compared to PEALD across all compositions.

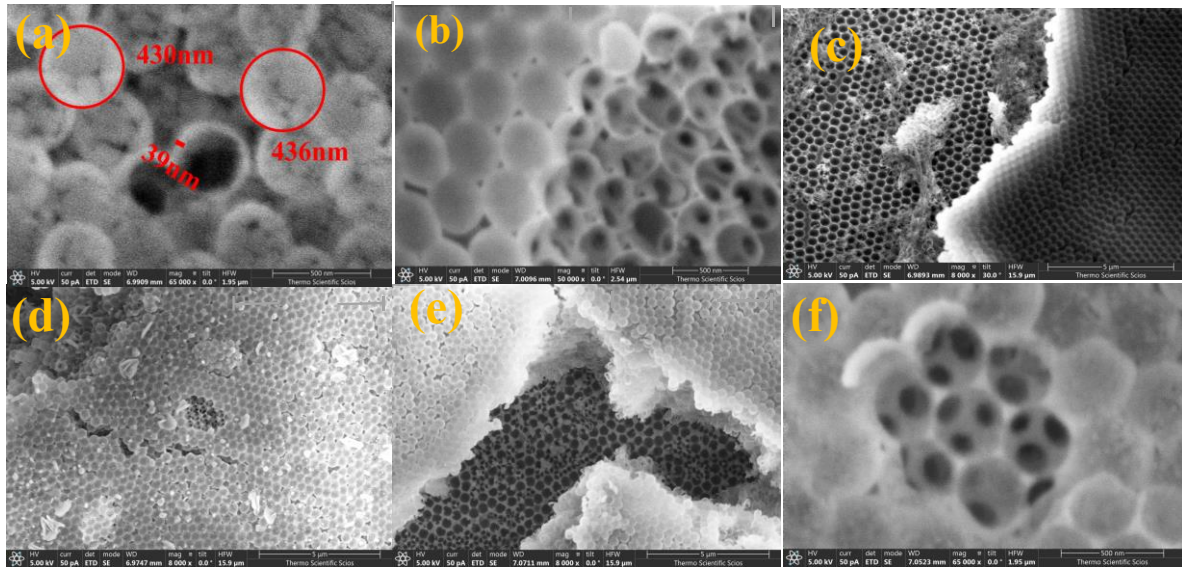


Figure 5.7: SEM micrographs of (a, b) Al₂O₃ IO, (c) Al₂O₃/ZnO TALD, (d) Al₂O₃/TiO₂ TALD, (e) Al₂O₃/ZnO PEALD, and (f) Al₂O₃/TiO₂ PEALD IOs and their composite samples.

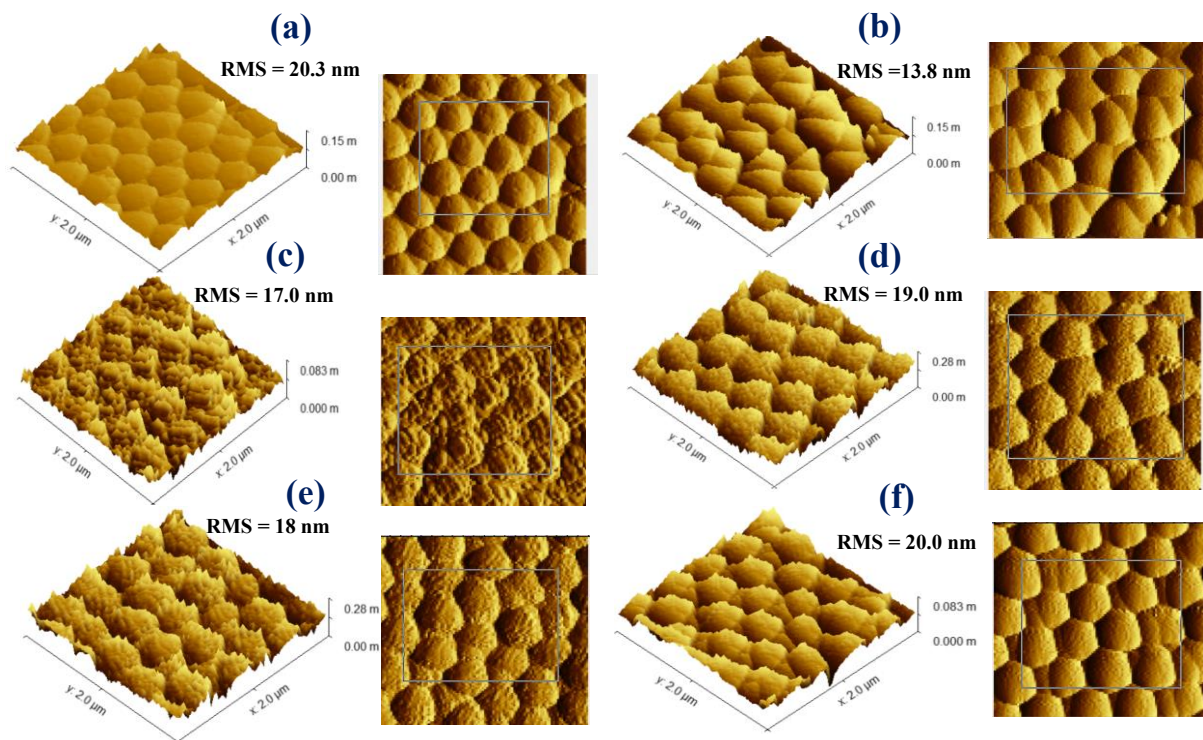


Figure 5.8: AFM images of: (a) 460-PS template, (b) pure Al₂O₃ IO, (c) Al₂O₃/ZnO-TALD, (d) Al₂O₃/ZnO-PEALD, (e) Al₂O₃/TiO₂-TALD, (f) Al₂O₃/TiO₂-PEALD, respectively.

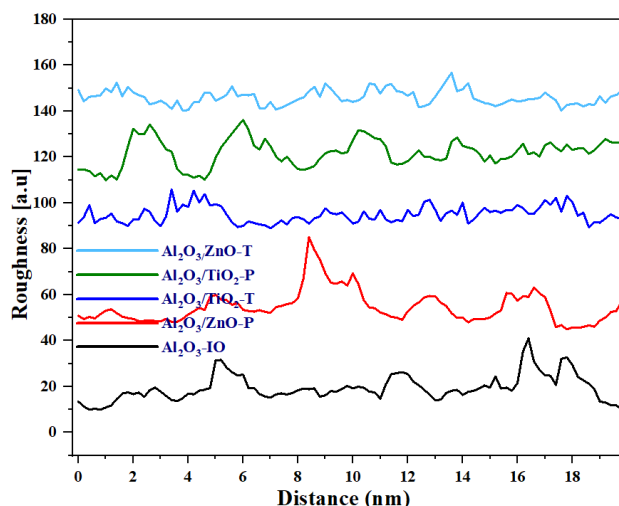


Figure 5.9: Roughness analysis of Al₂O₃ IO and composite samples using AFM

5.3.2. Compositional Analysis Determined by XPS

XPS analyses confirmed the composition of 460 nm-sized IOs synthesized via TALD and PEALD, followed by annealing at 900°C. No carbon was detected, verifying complete template removal. Al, O, Ti, and Zn were identified, confirming the formation of Al₂O₃, TiO₂, and ZnO deposits, with trace Si from the substrate. XPS spectra showed (Fig. 5.10) characteristic peaks for Al₂O₃ and its composites, with an "O loss" peak indicating oxygen vacancies. For Al₂O₃/ZnO composites, Zn incorporation was higher in PEALD (1.07 % Zn) than TALD (0.26 % Zn), while Al₂O₃/TiO₂ composites contained 0.6% Ti (TALD) and 0.4% Ti (PEALD). Elemental ratios remained consistent with Al₂O₃, suggesting ZnO and TiO₂ additions did not significantly alter the composition.

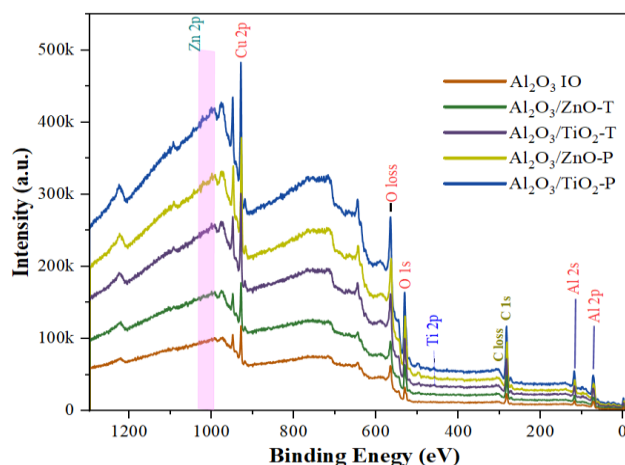


Figure 5.10: The XPS measurement results of Al₂O₃ IO and its composite samples.

5.3.3. Optical Properties Determined by UV Visible and PL Spectroscopy

The UV Visible absorption spectroscopy data for Al₂O₃ IO structures and their composites, including 5 nm ZnO or TiO₂ coated overlayers, reveal distinct optical characteristics influenced by their composition and structural modifications (Fig. 5.11 a). The pure Al₂O₃ IO and its composites containing 5 nm ZnO or TiO₂ overlayer coatings exhibit a UV absorption peak around 275 nm. This absorption is not associated with the intrinsic band gap of bulk Al₂O₃ (≈ 8.8 eV, corresponding to <150 nm), but rather arises from defect-related or interfacial electronic transitions introduced by the composite interfaces and surface states [151]. The absorption edges for all four materials are observed around 320 nm, with slight shifts toward shorter wavelengths (≈ 300 nm) observed across the samples. These variations are attributed to defect states introduced during the PEALD process, as well as stoichiometric and structural deviations that modify the electronic properties of the oxide layers [152].

Pure Al₂O₃ IO exhibits an additional absorption peak at approximately 400 nm, attributed to enhanced "slow photon" absorption at the short-wavelength (blue) and long-wavelength (red) edges of the PBG centered at 529 nm. This effect enhances photon absorption outside the PBG (APPENDIX B), increasing interaction time with the IO material and potentially improving optoelectronic efficiency. However, the PBG calculated using Bragg's equation (479 nm) is slightly lower than the experimental value (529 nm). This discrepancy likely arises from high-temperature annealing (900°C) used for template removal, which may cause shrinkage of the spheres and introduce structural defects. These imperfections are not accounted for in the idealized Bragg model, leading to deviations from experimental observations. TALD/PEALD Al₂O₃/ZnO and Al₂O₃/TiO₂ UV Visible spectra were similar to Al₂O₃, suggesting minimal optical impact from the 5 nm ALD coatings. Both composites showed a primary PBG around 529 nm, as expected for thin ZnO/TiO₂. Despite the bulk of the ZnO narrower band gap (~ 373 nm), composite PBGs (482-501 nm) slightly deviated from 529 nm, likely due to high-temperature annealing causing sphere shrinkage and disrupting structural periodicity, crucial for PBG formation.

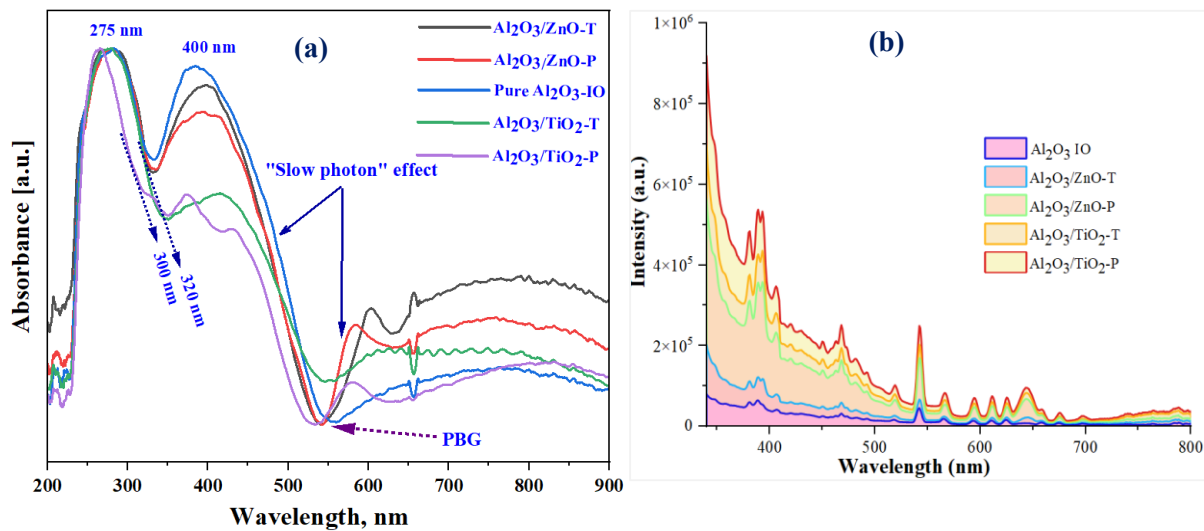


Figure 5.11: (a) UV Visible absorption, and (b) PL spectroscopy of Al₂O₃ IO samples and composite samples, respectively.

The increased PL intensity in Al₂O₃ IO upon TALD and PEALD coatings is attributed to enhanced passivation of defect states and modifications in optical properties (Fig. 5.11 b). Moreover, the PL spectrum of pure Al₂O₃ IO showed multiple emission peaks at approximately 389, 467, 542, 564, 624, 658, and 674 nm, covering the blue, green, and red regions of the visible spectrum. These emissions originated from intrinsic defect states in the alumina lattice, mainly oxygen vacancies (V_o), which determined the material's luminescent behavior. F⁺ centers formed when an oxygen vacancy trapped a single electron (V_o⁺) and caused the blue emissions at 389 nm and 467 nm through electronic transitions between localized defect levels and the band edges. F₂⁺ centers developed when two neighboring oxygen vacancies shared a single trapped electron, leading to more complex electronic configurations. These centers produced the green and red emissions (542–674 nm) via lower-energy radiative transitions. The presence of F⁺ and F₂⁺ centers facilitated broader, longer-wavelength luminescence, and the wide visible emission profile of Al₂O₃ IO resulted from the coexistence of multiple intrinsic defect states and their recombination pathways within the alumina lattice [153,154].

Similar peaks appeared in composites, while ZnO and TiO₂ coatings enhanced PL by passivating vacancies and boosting radiative recombination. TiO₂ composites, particularly via PEALD, exhibited the highest PL due to stronger optical confinement and higher refractive index, emphasizing the impact of coating and deposition method [155,156].

5.3.4. Inverse Opal Composite Layers by TALD and PEALD

This study successfully fabricated IO macrostructures and their composites using polystyrene nanosphere self-assembly and ALD techniques. Both TALD and PEALD were used for Al₂O₃ infiltration and deposition of ultrathin composite overlayers like ZnO or TiO₂ within the IO structures. The process involved high temperature annealing to remove the sacrificial template, which led to the final IO structure but also caused some cracks and shrinkage. The research found that both deposition methods and the materials used influenced the IO composites' final properties. TALD generally produced smoother surfaces and better conformality than PEALD; however, introducing ZnO or TiO₂ layers with either method increased the surface roughness. Both TALD and PEALD composites showed a primary PBG around 529 nm, with additional PBGs in ZnO and TiO₂ composites due to their specific band gaps. PL analyses indicated that incorporating ZnO and TiO₂ layers improved defect passivation and light-matter interactions in the IO structures. PEALD-treated samples showed enhanced PL intensity, confirming plasma activation's effectiveness in promoting defect passivation and enhancing film quality. XPS confirmed the successful incorporation of Al₂O₃, ZnO, and TiO₂ in IO structures, providing insights into surface chemistry details like hydroxylation and oxygen vacancies, with PEALD demonstrating higher ZnO deposition efficiency than TALD.

5.4. Fabrication of ZnO-Al₂O₃ Inverse Opals with Atomic Layer Deposited Amorphous-Al₂O₃ for Enhanced Photocatalysis.

5.4.1. Morphological and Compositional Analysis

The SEM micrograph in Fig. 5.12 showed that ALD successfully fabricated well-ordered ZnO IOs using a high-quality colloidal crystal template synthesized via the VLD method, which consisted of monodisperse PS-600 spheres with an average diameter of ~588 nm. Top-view SEM images revealed a highly periodic, close-packed sphere arrangement resembling the (100) planes of an FCC lattice, confirming the template's long-range order and suitability for ALD infiltration. The resulting pristine ZnO IO structure (Fig. 5.12 a & b), formed by conformal ALD deposition and template removal, exhibited a well-defined hollow network with a wall thickness of ~51.4 nm. The interconnected hollow spheres accurately replicated the template geometry, demonstrating ALD effectiveness in morphological reproduction.

Composite IO structures were fabricated via TALD and PEALD by depositing conformal Al₂O₃ layers. SEM micrograms (Fig. 5.12 c–f) revealed that TALD-grown composites retained the long-range order and periodicity of the original template more effectively than PEALD-derived samples, which exhibited slightly reduced structural regularity, likely due to plasma-induced non-uniform nucleation. A 5 nm ALD overlayer (Al₂O₃ or other oxides) did not alter the surface morphology or periodicity, confirming conformal coating preservation [157]. Post-deposition annealing at 500 °C removed the PS template without compromising the IO or composite framework, as the ALD deposition temperatures were substantially lower, preventing thermal distortion. All samples underwent volume shrinkage after annealing: SEM analysis (APPENDIX C) quantified ~8.0 % shrinkage for pure ZnO IOs, while ZnO/Al₂O₃-T (TALD) and ZnO/Al₂O₃-P (PEALD) composites showed higher shrinkage (16.7 % and 15.2 %, respectively), attributed to cumulative heat treatment effects and oxide layer densification.

Table 5.3 verified the EDX analysis of the elemental composition of ZnO and ZnO-Al₂O₃ composites. Pure ZnO IO exhibited near-stoichiometric Zn and O ratios. The ZnO/Al₂O₃ TALD and ZnO/Al₂O₃-PEALD composites contained 8.4 at % and 9.8 at % Al, respectively, with higher Al content in PEALD due to plasma-enhanced precursor activation. Minor impurities, such as carbon (residual precursors) and glass substrate elements (Na, Si, Ca) were

also detected. These results confirmed successful ZnO and Al₂O₃ deposition and demonstrated the impact of deposition techniques on elemental distribution and interfacial properties.

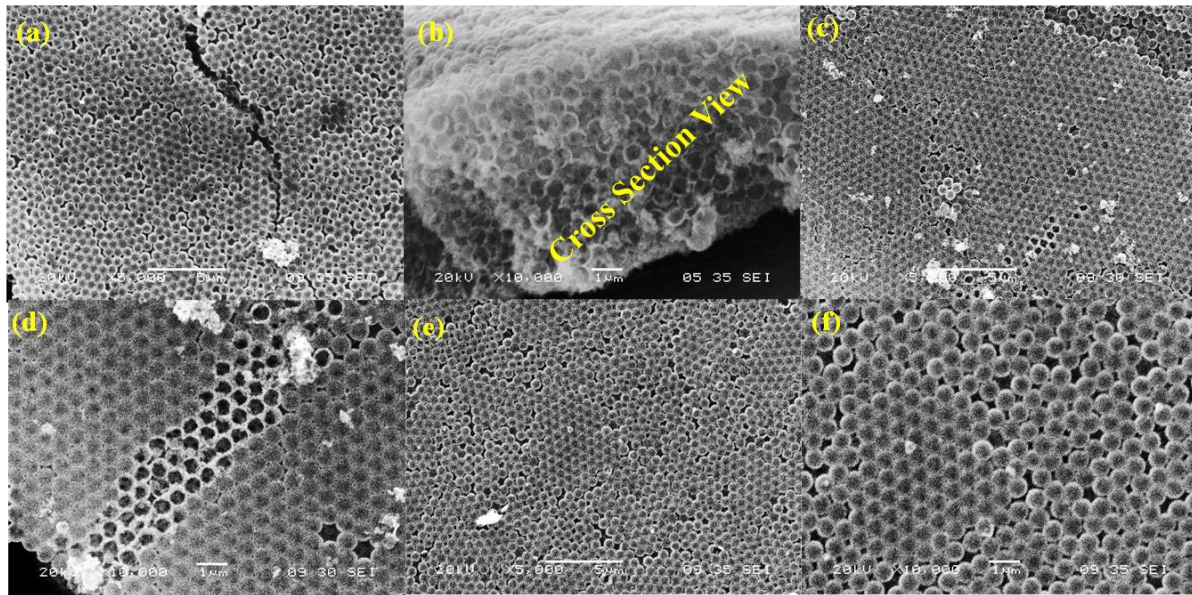


Figure 5.12: SEM images of pure ZnO IO (a,b), ZnO/Al₂O₃-T (c,d), and ZnO/Al₂O₃-P (e,f), respectively.

Table 5.3 EDX Table ZnO IO and composite samples

Samples	ZnO (At, %)	O (At, %)	Al (At, %)	Others (E.g., C, Si, %)
ZnO IO	44.5	53.5	-	2.0
ZnO/Al ₂ O ₃ -T	38.5	48.1	8.4	5.2
ZnO/Al ₂ O ₃ -P	37.2	46.2	9.8	6.8

5.4.2. Crystalline Structure Determined by XRD and Raman Spectroscopy Analysis

The hexagonal wurtzite crystal ZnO IO structure that was indexed with all the key diffraction peaks in the XRD study (Fig. 5.13 a) matched the standard data (ICCD card Number: 98-016-1836) rather well. The TALD or PEALD-grown 5 nm Al₂O₃ layer upon the IO structure was too thin and amorphous for XRD to identify. Because PS nanosphere templates are fragile and IO structures degrade at high annealing temperatures, the Al₂O₃ ALD film can only undergo crystallization when annealed at 1000-1200°C [99]. Annealing the TALD composite at 500°C improved the structural order of the ZnO IO. However, the same annealing conditions were insufficient to restore the ZnO order in the PEALD composite. The

PEALD coating disrupted the ZnO IO structure, resulting in stronger XRD peaks for TALD composites.

The pure ZnO IO wurtzite crystalline nanostructure was verified by Raman analysis, which showed shifts at ~ 333 , ~ 436 , ~ 578 , ~ 995 , and ~ 1132 cm^{-1} , with the most prominent peak at ~ 433 cm^{-1} (Fig. 5.13 b). The Al_2O_3 composite samples, TALD and PEALD, had different peak intensities, with PEALD being less intense than TALD, and neither sample had any Raman shifts. The primary reason for this is that the Al_2O_3 samples were too thin for Raman detection since only 19 ALD cycles were employed for thermal modes and 23 for plasma modes. Prior research has demonstrated that a higher number of ALD cycles and higher annealing temperatures (over 1000°C) are necessary to produce crystalline α - Al_2O_3 and γ - Al_2O_3 films [158].

5.4.3. UV Absorption and PL analysis

According to a UV Visible absorption study, the absorption edge of ZnO semiconductors is located around 400 nm, where all three samples showed a sharp decline in absorption [137,159]. Due to quantum confinement effects, the pure IO displayed the highest UV absorption between 360 and 380 nm (Fig. 5.13 c), which corresponds to the ZnO fundamental band gap. The pure ZnO IO computed band gap was 3.3 eV (APPENDIX G), which is quite near to that of bulk ZnO (3.2 eV). Even though Al_2O_3 nanoparticles absorb UV light at around 280 nm, ZnO- Al_2O_3 composites maintained a comparable absorption edge at 400nm. The ultrathin Al_2O_3 layer in the composites is the cause of this negligible impact. Additionally, the ZnO IO structure showed two absorption peaks at 434 nm (blue edge) and 660 nm (red edge), suggesting that the "slow photon" effect at the PBG edges, which are centered at 560 nm, boosted photon absorption. The PBG was theoretically calculated to be around 676 nm, based on the sacrificial template size of 588 nm (APPENDIX C). Because light is periodic, these absorption peaks correlate to wavelengths where it slows down within the IO structure, boosting absorption [43,44].

The composite showed two visible-region absorption peaks resembling pure IO but with minor PBG shifts to 580 nm for the TALD composite and 570 nm for the PEALD composite. This suggests that Al_2O_3 had a subtle effect on the ZnO IO PBG. In contrast to the actual results, the computed PBGs (557 nm for ZnO/ Al_2O_3 -T and 565 nm for ZnO/ Al_2O_3 -P) were lower for bare ZnO IO. These discrepancies were most likely the result of different macrostructural characteristics of composite and pure ZnO IO structures.

Pure ZnO IO emitted light in both the visible and UV ranges, but the composites only emitted in the visible range, according to the PL spectra of ALD samples (Fig. 5.13 d). The visible emissions were partly attributed to F^+ and F_2^+ centers in ZnO, which act as electron traps and radiative recombination sites. In addition to minor peaks at 468 nm (blue) and 543 nm (green) caused by electron relaxation at surface defects, the pure IO structure showed a significant UV peak at 388 nm, which was ascribed to direct charge carrier recombination [141,160]. In contrast to the PEALD composite, which exhibited two prominent peaks at 468 nm and 543 nm and several smaller peaks between 569 and 679 nm, the ZnO-Al₂O₃-T composite showed peaks at 468 nm, 564 nm, and 764 nm. F^+ and F_2^+ centers also contributed to the enhanced visible emission in the PEALD composite by facilitating recombination at defect sites. More defects at the ZnO-Al₂O₃ interface, which trap charge carriers and promote recombination, were the cause of the PEALD composite having enhanced visible emission. The TALD composite, on the other hand, had fewer flaws, which led to increased photocatalytic activity but decreased emission of visible light [161]. In general, charge carrier recombination was the source of PL emissions, which were probably impacted by structural flaws from plasma deposition.

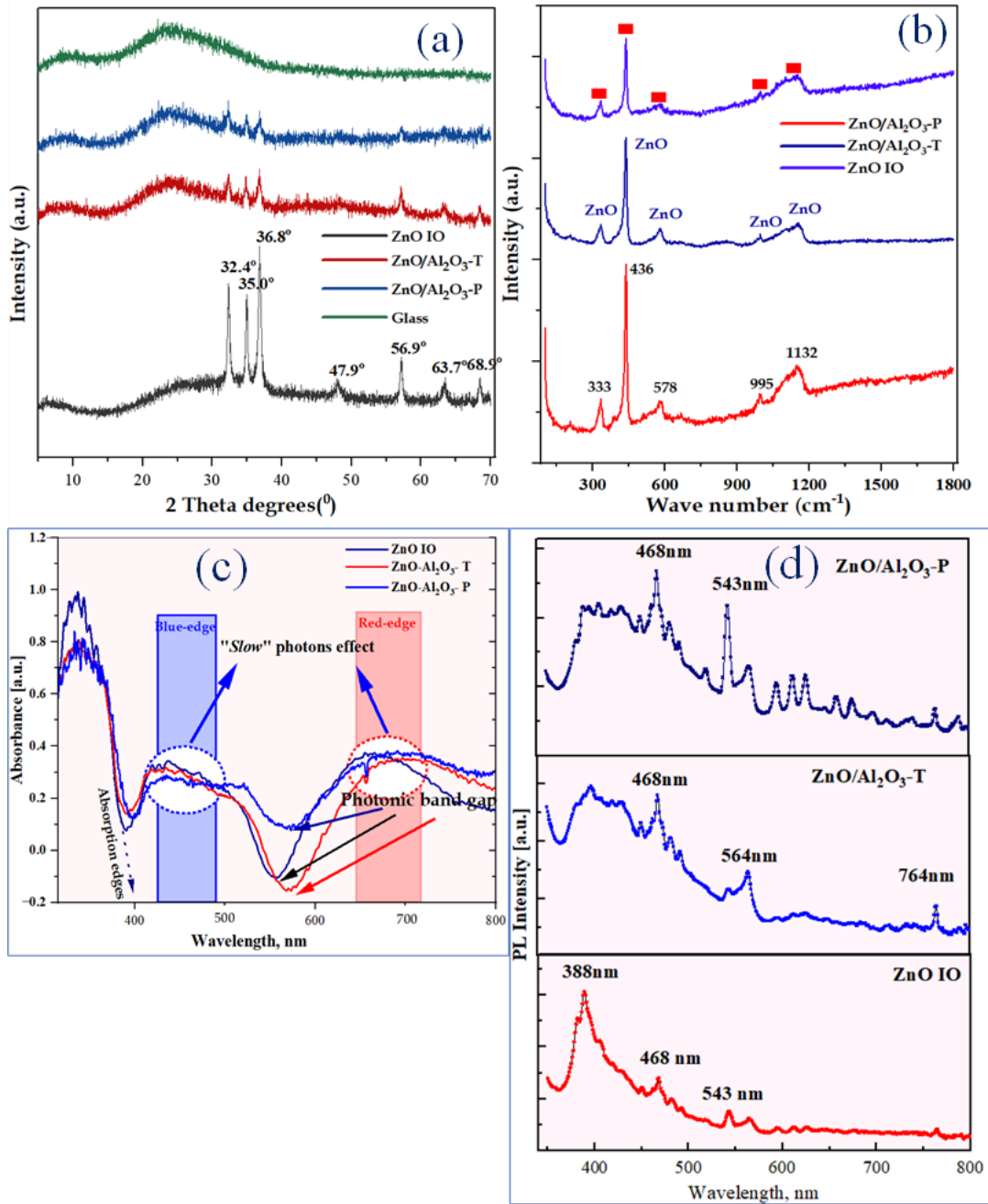


Figure 5.13. (a) XRD diffraction patterns, (b) Raman spectroscopy, (c) UV Visible absorption spectroscopy, and (d) the PL emission spectra of: pure ZnO IO, composite ZnO-Al₂O₃-T, and composite ZnO-Al₂O₃-P, respectively.

5.4.4. Photocatalytic Studies of ALD-Synthesised Inverse Opals Under Visible Light

The degradation of pollutants such as MB, Rh6G, and 4-NP, respectively, when exposed to visible light was used to assess the IO structure's photocatalytic activity (See Fig. 5.14). The pure ZnO IO showed maximum efficiency in breaking down MB because of its highly ordered structure, which improved light absorption and directed photons deeper into the material. All

samples showed pseudo-first-order degradation kinetics [33,42,91]. This impact was further accentuated by the high pore size (~588 nm). With a relative absorbance of 0.78, the IO structure, on the other hand, had the slowest degradation for 4-NP and lesser efficiency for Rh6G. Outperforming both pure IO and PEALD composites by at least 10 %, the TALD-coated IO had the best photocatalytic activity among the composites, attaining the maximum degradation rates ($k = 0.0022 \text{ min}^{-1}$) (see also APPENDIX H and I) and efficiencies (up to 69%) for MB and Rh6G. This improvement was ascribed to the ultrathin Al_2O_3 passivation layer, which enhanced light absorption and the production of reactive oxygen species by decreasing charge recombination, maintaining the ordered IO structure during annealing, and optimizing PBG interactions.

The degradation rate of the $\text{ZnO}/\text{Al}_2\text{O}_3$ -T combination varied according to how the pollutants interacted with visible light. Though Rh6G degraded a little more slowly, both MB and Rh6G, which have conjugated chromophore structures, effectively absorbed visible light, promoting electron excitation and charge transfer [162]. In contrast, 4-NP exhibited less visible light interaction due to its smaller structure and primary UV absorption, which resulted in a decreased rate of deterioration. Due to plasma-assisted deposition, which broke crystallinity and added additional defects, the PEALD-coated $\text{ZnO}/\text{Al}_2\text{O}_3$ composite's photocatalytic activity was diminished, as evidenced by its greater Urbach energy, which reflects the degree of disorder and defect-induced localized states in the band gap ($E_u = 0.28 \text{ eV}$) (APPENDIX G) and band gap ($E_g = 3.4 \text{ eV}$).

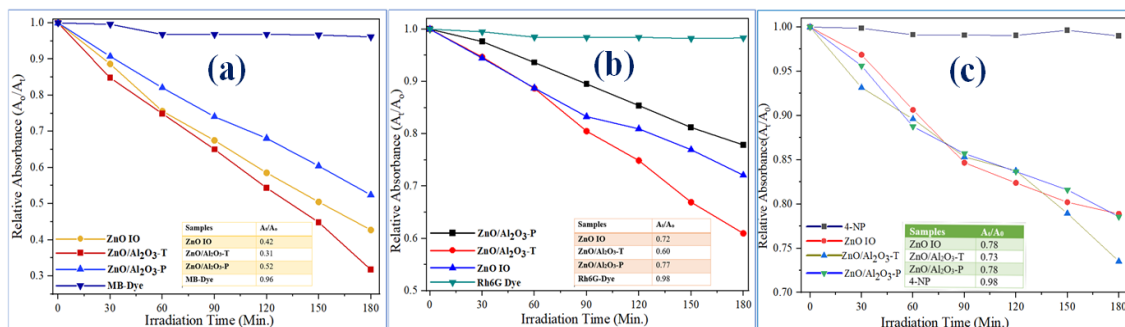


Figure 5.14: Decolorization of MB, Rh6G, and 4-NP dyes through photocatalysis under visible light irradiation for 3 hours using photocatalyst samples grown through ALD. (a-c) Photocatalytic performance – A_t/A_0 vs irradiation time, using ALD photocatalyst samples in the presence of MB (a), Rh6G (b), and 4-NP (c), respectively.

4.5. Synthesis of TiO₂/Al₂O₃ Double Layer Inverse Opal by Thermal and Plasma-Assisted ALD for Photocatalytic Applications

4.5.1. Morphological and Compositional Analysis of the ALD IO samples

The fabrication and structural analysis of TiO₂ and TiO₂/Al₂O₃ IO arrays were carried out using an infiltration approach, whereby the chosen precursor materials were introduced into the voids of a PS nanosphere template. This process enabled the formation of a highly ordered porous structure by replicating the template geometry. The SEM images presented in Figure 5.15, (a), (b), and (c), clearly illustrate the top-view morphology of the synthesized structures. Figure (a) shows the initial opal template made from PS nanospheres, characterized by its uniformly distributed spherical particles and a highly ordered hexagonal arrangement, indicative of excellent monodispersity and packing. After infiltration and subsequent template removal, the resultant IOs retain this periodicity and closely mimic the original opal structure.

Particularly, both the pristine IO TiO₂ and the combined TiO₂/Al₂O₃ samples exhibited interconnected, well-ordered microporous networks, confirming the successful replication of the template architecture. These structures were consistent with an FCC lattice arrangement, a common feature in well-aligned colloidal crystal assemblies. However, despite the overall structural integrity, minor cracks were evident, which could be attributed to volumetric shrinkage during the annealing process. This shrinkage was particularly significant, with the IO shells contracting by approximately 16.7 % post-annealing, leading to the observed fissures in the otherwise continuous porous matrix. Besides, the composition of the samples from the EDX analysis was presented in APPENDIX J, showing significant concentrations of Ti, Al, and O in both the pure IO and double-layer samples.

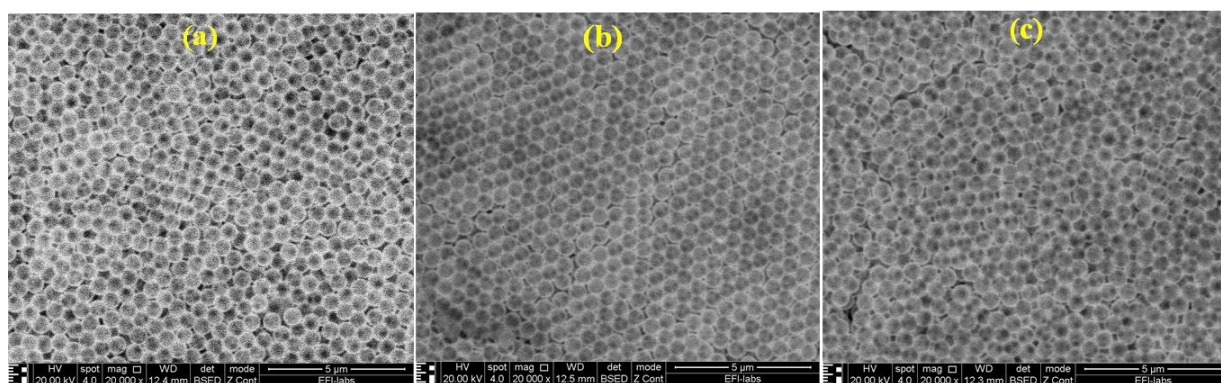


Figure 5.15: SEM micrograms of (a) pure TiO₂ IO, (b) TiO₂/Al₂O₃-TALD, and (c) TiO₂/Al₂O₃-PEALD, respectively.

4.5.2. Structural and Optical Studies

XRD and Raman spectroscopy were both used to characterize the TiO₂ IO and its composite material crystalline arrangement. The TiO₂ tetragonal anatase phase (ICCD card number: 98-009-2363) was represented by the main XRD peaks, which were seen at 25.6⁰, 38.2⁰, 48.6⁰, 55.4⁰, and 63.1⁰. In agreement with the findings of Chakraborty et al., the amorphous TiO₂ was crystallized into a stable anatase phase at an annealing temperature of 500°C [163]. The ultrathin layer of TALD maintained the crystallinity of TiO₂ IO, but plasma ALD decreased both crystallinity and the intensity of TiO₂ peaks, revealing only those at 25.6°, 38.2°, and 48.6° (Fig. 5.16 a).

The results from Raman spectroscopy showed peaks at around 142, 395, 519, and 637 cm⁻¹, which matched the tetragonal anatase TiO₂ IO phase (Fig. 5.16 b). Šćepanović et al. discovered a similar Raman shift trend for TiO₂ IO nanostructures [164]. The ultrathin layers of amorphous Al₂O₃ produced by thermal or plasma ALD were not visible, just like in the XRD analysis.

The pure TiO₂ and its composite IO samples demonstrated a significant increase in absorption intensity at shorter wavelengths, with distinct absorption edges observed at 330 nm for pure TiO₂, 320 nm for the thermal ALD-grown TiO₂/Al₂O₃ double-layer nanocomposite, and 335 nm for the plasma ALD-grown counterpart, as illustrated in Fig. 5. 17 a-c. These sharp absorption edges enhanced the overall light absorption efficiency due to “slow photon” effects, which involve reduced group velocity of light propagation, as referenced in studies, facilitating electronic transitions that generate electron-hole pairs essential for photocatalytic activity [38]. Additionally, the composite samples exhibited extended absorption edges into the visible region, specifically at 470 nm, 630 nm, and 800 nm for the thermal ALD samples and 490 nm, 610 nm, 672 nm, and 800 nm for the PEALD samples, with these sinusoidal absorption patterns correlating to the layer thickness and the influence of ultrathin Al₂O₃ ALD films combined with an energy band gap ranging between 3.6 eV and 3.8 eV.

The fundamental absorption energy, associated with electron excitation from the valence band to the conduction band, was utilized to determine the energy band gap of the thin films using the Tauc model, which fits the absorption spectrum to estimate E_g, as described in the reference [106]. The Tauc equation (see Equation 5.2),

$$(\alpha h\nu)^{1/n} = A (h\nu - E_g) \quad 4.2$$

where α represents the absorption coefficient, E_g is the band gap energy, $h\nu$ is the photon energy, and A is a constant related to the transition type, was applied with $n = \frac{1}{2}$ for indirect band gap calculations. The calculated indirect optical band gaps were 3.2 eV for pure TiO_2 , 3.6 eV for the thermal ALD-grown $\text{TiO}_2/\text{Al}_2\text{O}_3$ nanocomposite, and 3.8 eV for the plasma ALD-grown sample. Particularly, while bulk Al_2O_3 typically exhibits a much higher band gap (8.7 eV) [165], the composite $\text{TiO}_2/\text{Al}_2\text{O}_3$ structure resulted in a reduced band gap, attributed to the interfacial interactions between the materials. Furthermore, the plasma ALD-grown Al_2O_3 , characterized by a highly amorphous and less ordered structure, exhibited a lower band gap compared to previously reported values for thicker plasma ALD Al_2O_3 films (4.3 eV for 8 nm and 4.75 eV for 38 nm), aligning with findings from Shi et al. and Costina on ultrathin Al_2O_3 films [166,167]. These results underscore the influence of deposition method and structural properties on the optical characteristics of nanocomposite materials.

Furthermore, UV Visible absorption (See Fig. 5.17 a-c) also determined that the pure TiO_2 IO exhibited a single PBG at 400 nm, the $\text{TiO}_2/\text{Al}_2\text{O}_3$ composites display multiple PBGs in the visible range— $\text{TiO}_2/\text{Al}_2\text{O}_3$ -TALD at 400, 550, and 720 nm, and $\text{TiO}_2/\text{Al}_2\text{O}_3$ -PEALD at 400, 560, 645, and 750 nm, due to the introduction of composite (Al_2O_3) layers modifying the refractive index contrast and optical path.

The PL spectra of three IO photocatalysts at an excitation wavelength of 380 nm are shown in Fig. 5.17 d. All three PL curves had broad peaks between approximately 515 nm and 540 nm, with a threshold of 420 nm and a cut-off at 800 nm. These PL bands matched the "green band" (~515 nm) found in ALD-grown anatase TiO_2 IOs, associated with surface oxygen vacancies, and the "red band" (~600 nm), linked to Ti^{3+} defects [168]. The thermal composite $\text{TiO}_2/\text{Al}_2\text{O}_3$ showed the strongest PL and most intense (101) anatase XRD peak, while the plasma composite $\text{TiO}_2/\text{Al}_2\text{O}_3$ exhibited the weakest luminescence and lowest crystallinity, due to plasma-induced defects and disorder. Higher crystallinity resulted in stronger PL by reducing non-radiative recombination centers.

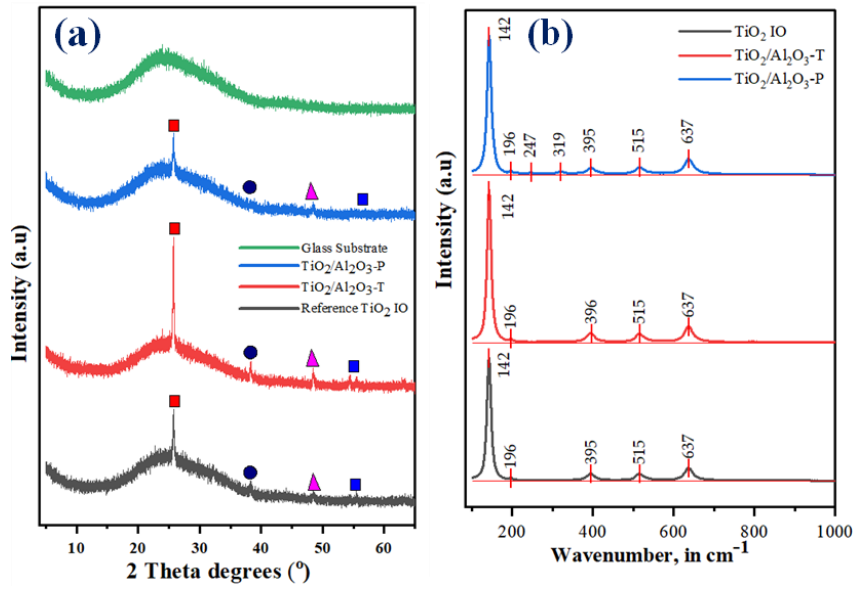


Figure 5.16 (a) XRD, (b) Raman analysis results of IOs of pure TiO₂, TiO₂/Al₂O₃-thermal, TiO₂/Al₂O₃-plasma ALD composite samples, respectively.

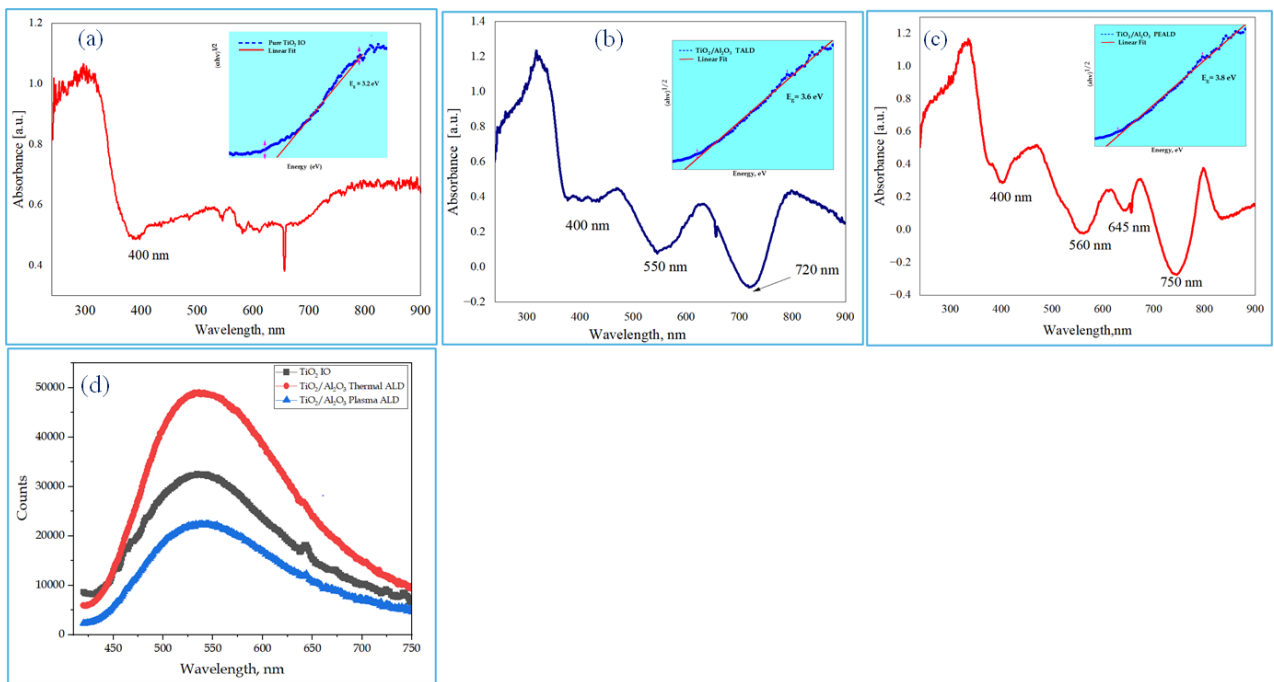


Figure 5.17: UV Visible absorption results of IOs of pure TiO₂ (a), TiO₂/Al₂O₃-TALD (b), TiO₂/Al₂O₃-PEALD (c) composite samples, and (d) PL spectroscopic results, respectively.

4.5.3. Photocatalytic Activities of IO TiO₂ and ALD-Coated Al₂O₃ Composites for MB Dye Decolorization

All samples showed successful MB dye decolorization under UV Visible light, according to the photocatalytic analysis, which used a pseudo-first-order kinetic model (Table 5.4). In contrast to thermal and plasma ALD-grown TiO₂/Al₂O₃ composites, which had lower rate constant (k) values, bare IO TiO₂ demonstrated the highest k. The quickest decolorization was accomplished by TiO₂ IO (35.4% in 3 hours), while the values for thermal and plasma Al₂O₃ composites were 24.7% and 14.8%, respectively (APPENDIX K). The more ordered structure and narrow band gap of the thermally produced Al₂O₃ composite IO improved optical absorption and charge carrier interaction, which in turn improved photocatalysis. However, the decreased electron tunnelling caused by the higher thickness of Al₂O₃ was the reason for the decreased activity of Al₂O₃-coated samples in comparison to bare IO TiO₂ [169].

Table 5.4: The rate constant, k, and linear regression square, R², of the sample

Sample	R ²	Rate Constant, k (* 10 ⁻² Min ⁻¹)
Pure TiO ₂ IO	0.9957	0.24
TiO ₂ /Al ₂ O ₃ thermal	0.9981	0.16
TiO ₂ /Al ₂ O ₃ plasma	0.9932	0.089
MB dye	0.994	0.014

5. CONCLUSION

In this research work, I have successfully fabricated IOPC structures using ALD methods, leveraging PS nanospheres of varying sizes, 300 nm, 460 nm, and 600 nm, as sacrificial templates. These templates played a pivotal role in defining the structural integrity, periodicity, and subsequent photocatalytic performance of the synthesized materials, including TiO₂, ZnO, Al₂O₃, and their various composites. Each template size produced distinct porous architectures characterized by an FCC arrangement, confirmed via SEM. In the case of 300 nm PS templates, used for TiO₂ and ZnO IOs, SEM revealed highly ordered structures with visible shrinkage post-template removal, approximately 14 % for TiO₂ and 3.4 % for ZnO. These differences highlight material-dependent contraction behaviour. For 460 nm and 600 nm PS spheres, used to fabricate Al₂O₃ and ZnO-based IOs, the final pore sizes were slightly reduced to ~433 nm due to thermal annealing. A 600 nm template applied to double-layered TiO₂/Al₂O₃ structures yielded an ordered and uniform network, also showing minimal structural differences after calcination at 500 °C.

The impact of PS sphere size extended beyond structure, directly influencing PBGs and the “slow photon” effect, both crucial for enhancing light–matter interaction in photocatalysis. Optical characterization through UV Visible spectroscopy revealed distinct PBGs correlating with the template diameter. For example, Al₂O₃ IOs templated with 460 nm PS exhibited a PBG centered around 529 nm, while smaller spheres yielded blue-shifted gaps. These effects facilitated improved light absorption, especially under visible light in composite systems like ZnO/Al₂O₃ and TiO₂/ZnO.

Photocatalytic testing across all systems demonstrated that pristine IOs (TiO₂ and ZnO) were more efficient under UV irradiation due to optimal electric bandgap energies (3.0–3.2 eV) and high porosity for pollutant adsorption. Particularly, the ZnO IOs derived from 588 nm spheres exhibited enhanced visible-light activity when coated with Al₂O₃ via TALD, outperforming their plasma-treated counterparts. This improvement was attributed to enhanced passivation, reduced recombination centers, and preserved crystallinity. Similarly, TiO₂/Al₂O₃ composites fabricated with 600 nm PS templates showed degradation efficiencies of 35.4 % for pristine TiO₂ IO, 24.7 % for thermal Al₂O₃ coatings, and 14.8% for plasma-grown layers under visible light, as measured using MB dye.

Despite the improved visible-light responsiveness of composites, pristine IOs generally maintained over UV-driven degradation rates. However, PEALD-treated samples often

suffered from surface roughness and structural disorder, as confirmed by AFM and PL spectroscopy, which observed diminished emission intensity and broader defect-related peaks. Conversely, thermal ALD produced smoother, more conformal coatings that preserved the IO framework and enhanced interfacial charge transfer. Particularly, Al₂O₃ layers (~4.4–5.5 nm thick) were amorphous and undetectable in XRD or Raman but played a significant role in altering the bandgap (up to 3.8 eV in PEALD composites).

Furthermore, the template size is a fundamental design parameter in tuning the morphology, optical behavior, and photocatalytic performance of IO materials. Smaller PS spheres (300 nm) led to tighter structures and stronger UV absorption, while larger spheres (460 nm and 600 nm) enhanced visible-light interactions and structural stability. Coupled with the deposition strategy (TALD vs. PEALD), these factors dictate the balance between UV and visible photocatalytic activity. The findings advocate precise control over template size and layer deposition to engineer IOs for targeted environmental applications, especially in harnessing solar energy for pollutant degradation. Future directions include optimizing interface chemistry and exploring doped or multi-functional coatings to further expand the operational window into the visible spectrum.

6. THESIS POINTS

1. Using low-temperature (50 °C) plasma-enhanced atomic layer deposition (PEALD), I synthesized TiO₂ and ZnO single-material as well as ZnO/TiO₂ and TiO₂/ZnO composite inverse opal photonic crystal (IOPC) structures. For this opal template of 300 nm sacrificial polystyrene (PS) particles were applied, which were removed after PEALD by annealing in air at 500 °C. The second PEALD layer resulted in a ca. 30 nm red shift in the photonic bandgap (PBG) compared to the PBG of the first layer. In photocatalytic tests, single-material IOPCs degraded the model pollutants (4-nitrophenol, 4-NP and rhodamine 6G, Rh6G) more efficiently under UV light, while the composites were more efficient under visible-light irradiation [P3].
2. I prepared Al₂O₃/TiO₂ and Al₂O₃/ZnO IOPCs using a combination of thermal atomic layer deposition (TALD) and PEALD. At first, Al₂O₃ IOPC was made via TALD using a 460 nm PS opal template, depositing 36 nm Al₂O₃ layer by TALD and annealing it at 450 °C. Then ultrathin (~5 nm) TiO₂ or ZnO overlayers were grown by both TALD and PEALD on the Al₂O₃ IOPC to form Al₂O₃/TiO₂ and Al₂O₃/ZnO composites, followed by post annealing at 900 °C. Atomic force microscopy (AFM) showed that composites with TALD-grown overlayers had smoother surfaces (Root mean square - RMS: 17–18 nm) than those grown by PEALD (RMS: 19–20 nm) [P4].
3. I fabricated ZnO/Al₂O₃ IOPCs by combining TALD and PEALD. A 52 nm ZnO layer was first grown by TALD on a 600 nm PS nanosphere opal template and subsequently converted into a ZnO IOPC by annealing at 500 °C. Consecutively, an ultrathin (~5 nm) Al₂O₃ layer was deposited by TALD or PEALD to obtain ZnO/Al₂O₃-TALD and ZnO/Al₂O₃-PEALD composites. The electric bandgap shifted from 3.3 ± 0.01 eV (single-material ZnO) to 3.4 ± 0.01 eV for TALD-coated and 3.6 ± 0.01 eV for PEALD-coated composites, due to the ultrathin Al₂O₃ overlayer. After 3 hours visible-light irradiation the TALD-coated composite was more effective in the photocatalytic decomposition of photocatalytic studies to decompose methylene blue (MB), Rh6G, and 4-NP model compounds, achieving 69 %, 40 %, and 27 % degradation, respectively, compared to the PEALD-coated composite (48 %, 23 %, and 22 % degradation, respectively) [P2].

4. By combining TALD and PEALD, I synthesized $\text{TiO}_2/\text{Al}_2\text{O}_3$ IOPCs. At first, TiO_2 IOPC was prepared by depositing 52 nm of TiO_2 via TALD onto a 600 nm PS sacrificial template, followed by annealing at 500 °C. After this, a ~5 nm Al_2O_3 film was grown on it by either TALD or PEALD to get $\text{TiO}_2/\text{Al}_2\text{O}_3$ -TALD and $\text{TiO}_2/\text{Al}_2\text{O}_3$ -PEALD composites. The electric bandgap (3.2 ± 0.01 eV for the TiO_2) shifted to 3.6 ± 0.01 eV for TALD-coated, and to 3.8 ± 0.01 eV for PEALD-coated composites, due to the ultrathin Al_2O_3 overlayer. The TALD composite exhibited more efficient photocatalytic activity than its PEALD counterpart, achieving 25% MB degradation under 3 hours of visible-light irradiation, compared to 15% [P1].

7. PUBLICATIONS

7.1. PUBLICATIONS RELATED TO DISSERTATION

- P1 **Hamsasew Hankebo Lemago**, Addin F.S., Atilla K, Igricz T, Parditka B, Hessz D, Erdélyi Z., Szilágyi I.M., Synthesis of TiO₂/Al₂O₃ Double-layer inverse opal by thermal and plasma-assisted atomic layer deposition for photocatalytic applications. *Nanomaterials* **2023**, 13, 1314. <https://doi.org/10.3390/nano13081314>; **Q1**, IF:**4.4**, Independent Citations: 1.
- P2 **Hamsasew Hankebo Lemago**, Nour Khauli, Dóra Hessz, Tamás Igricz, Pál Petra, Csaba Cserhádi, Baradács Eszter Mónika, Bence Parditka, Zoltán Erdélyi, Imre Miklós Szilágyi, Fabrication of ZnO/Al₂O₃ inverse opals with atomic layer deposited Amorphous-Al₂O₃ for enhanced photocatalysis. *Materials Science in Semiconductor Processing* **2024**, 183, 108733. <https://doi.org/10.1016/j.mssp.2024.108733>; **Q1**, IF: **4.2**, Independent Citations: 3.
- P3 **Hamsasew Hankebo Lemago**, Leticia Tolezani, Tamás Igricz, Dóra Hessz, Petra Pál, Csaba Cserhádi, Gergő Vecsei, Barbara Sárközi, Eszter Mónika Baradács, Zoltán Erdélyi, and Imre Miklós Szilágyi, Enhanced Photocatalysis via Inverse Opal Structures: Synthesis and Characterization of TiO₂/ZnO and ZnO/TiO₂ Composites Using Plasma-Enhanced ALD. *Ceramic International* **2025**, 51, 339352. <https://doi.org/10.1016/j.ceramint.2024.10.465>; **Q1**, IF: **5.1**, Independent Citations: 17.
- P4 **Hamsasew Hankebo Lemago**, Soeun Choi, Dóra Hessz, Gyula Jággerszki, Petra Pál, Csaba Cserhádi, Eszter Mónika Baradács, Tamás Fodor, Zoltán Erdélyi, and Imre Miklós Szilágyi, Thermal, and Plasma-Enhanced ALD for the Synthesis of Inverse Opal Al₂O₃ and Its Composite Materials. *Vacuum*, **2025**, 238, 114254. <https://doi.org/10.1016/j.vacuum.2025.114254>; **Q1**, IF: **3.8**, Independent Citations: 0.

7.2. PUBLICATION PARTLY RELATED TO DISSERTATION

1. **Hamsasew Hankebo Lemago**, and Imre Miklós Szilágyi, Inverse opal photonic crystals: synthesis techniques, unique properties, and multifunctional applications, A review paper, *Applied Surface Science Advances* **2025** 28,100805. <https://doi.org/10.1016/j.apsadv.2025.100805>, SJR 2024, **Q1**, IF: **8.7**, Independent Citations: 0.

7.2. PUBLICATIONS NOT RELATED TO DISSERTATION

1. Luminița Predoană, Jeanina Pandeale-Cusu, Irina Atkinson, Simona Petrescu, Oana Cătălina Mocioiu, Daniela C. Culiță, Dániel Attila Karajz, Vincent Otieno Odhiambo, Hamsasew Hankebo Lemago, Ana Paula Barreto Gomes, Zalán István Várady, Marcell Bohus, Imre M. Szilágyi, György Pokol, Ruxandra M. Costescu, Maria Zaharescu; Comparative study of the Cu-TiO₂ nanostructures obtained by sol-gel and microwave-assisted sol-gel methods; *Journal of Sol-Gel Science and Technology*, 2025, <https://doi.org/10.1007/s10971-025-06757-x> SJR 2024 Q2, IF: **2.3**, Independent Citations: 0

8. CONFERENCE PARTICIPATION

1. **Hamsasew Hankebo Lemago**, Feras Shugaa Addin, Bence Parditka, Zoltán Erdélyi, and Imre Miklós Szilágyi; 11 – 13th of July 2022, 1st Forum of Young Researchers on Heterogeneous Catalysis, YOURHETCAT 2022, Szeged, Hungary; **Poster** presentation on Preparation of TiO₂/Al₂O₃ double-layered inverse opal photocatalysts by plasma and thermal ALD methods.
2. **Hamsasew Hankebo Lemago**, Daniel Karajz, Nour Khauli, Tamas Igricz, Bence Parditka, Zoltán Erdélyi and Imre Miklós Szilágyi; 26th of September 2022, 4th George Olah Conference, Budapest Hungary. **Poster** presentation on Fabrication and characterization of ZnO and ZnO/Al₂O₃ composite inverse opals by thermal and plasma-assisted ALD for photocatalysis.
3. **Hamsasew Hankebo Lemago**, Tamás Igricz, Bence Parditka, Zoltán Erdélyi, and Imre Miklós Szilágyi; 3rd Journal of Thermal Analysis and Calorimetry Conference and 9th V4 (Joint Czech-Hungarian-Polish-Slovakian) Thermoanalytical Conference 20–23rd June 2023, Balatonfüred, Hungary, **Poster** presentation on Thermal and plasma-assisted atomic layer deposition for the synthesis of inverse opal photocatalysts.
4. **Hamsasew Hankebo Lemago**, L. Tolezani, A. Choi, T. Igricz, B. Parditka, Z. Erdélyi, and I.M. Szilágyi, **Oral** presentation on ZnO-Al₂O₃ composite inverse opals for enhanced Photocatalysis, International Conference of Physical Chemistry-**ROMPHYSICHEM** 17th edition: September 25-27, 2023, Bucharest, Romania.
5. **Hamsasew Hankebo Lemago**, Tamás Igricz, Zoltán Erdélyi, and Imre Miklós Szilágyi, **Oral** presentation on Atomic Layer Deposition of Inverse Opals for Photocatalytic Degradation of Methylene Blue under Visible Light Illumination, Materials science day XXIII of PhD students conference on the 20th November 2023.
6. Cristina Maria Vlăduț, Oana Cătălina Mocioiu, Irina Atkinson, Imre Miklós Szilágyi, Jeanina Pandeale Cușu, János Madarász, Dániel Karajz, **Hamsasew Hankebo Lemago**; 3rd Journal of Thermal Analysis and Calorimetry Conference and 9th V4 (Joint: Czech-Hungarian-Polish-Slovakian) Thermoanalytical Conference 20–23rd June 2023, Balatonfüred, Hungary, **Poster** presentation on Synthesis and Characterization of Doped Zinc Oxide Nanoparticles for Nanofluids.

7. Luminita Predoana, Irina Atkinson, Dániel Attila Karajz, Vincent Otieno Odhiambo, **Hamsasew Hankebo Lemago**, Jeanina Pandeale-Cusu, Simona Petrescu, Adriana Rusu, Nicoleta Apostol, Imre M. Szilágyi, György Pokol, Maria Zaharescu, July 24-29 International Solgel Conference Solgel 2022, Lyon, France. **Poster** presentation on Properties of the Cu-TiO₂ nanostructures obtained by sol-gel and microwave-assisted sol-gel methods.

8. REFERENCES

- [1] J. Theerthagiri, S.J. Lee, K. Karuppasamy, S. Arulmani, S. Veeralakshmi, M. Ashokkumar, M.Y. Choi, Application of advanced materials in sonophotocatalytic processes for the remediation of environmental pollutants, *J. Hazard. Mater.* 412 (2021) 125245. <https://doi.org/10.1016/j.jhazmat.2021.125245>.
- [2] C. Karthikeyan, P. Arunachalam, K. Ramachandran, A.M. Al-Mayouf, S. Karuppuchamy, Recent advances in semiconductor metal oxides with enhanced methods for solar photocatalytic applications, *J. Alloys Compd.* 828 (2020) 154281. <https://doi.org/10.1016/j.jallcom.2020.154281>.
- [3] L. Zhu, X. Shang, K. Lei, C. Wu, S. Zheng, C. Chen, H. Song, Doping in Semiconductor Oxides-Based Electron Transport Materials for Perovskite Solar Cells Application, *Sol. RRL.* 5 (2021). <https://doi.org/10.1002/solr.202000605>.
- [4] A. Chaudhari, X. Cui, B. Hoex, L. Hyde, C.N. Ironside, W.M. Jadwisieniczak, M.E. Kordesch, F. Rahman, R.D. Vispute, Zinc oxide family semiconductors for ultraviolet radiation emission – A cathodoluminescence study, *Mater. Res. Bull.* 153 (2022) 111906. <https://doi.org/10.1016/j.materresbull.2022.111906>.
- [5] M.I. Din, R. Khalid, Z. Hussain, Recent Research on Development and Modification of Nontoxic Semiconductor for Environmental Application, *Sep. Purif. Rev.* 50 (2021) 244–261. <https://doi.org/10.1080/15422119.2020.1714658>.
- [6] E. Armstrong, C. O'Dwyer, Artificial opal photonic crystals and inverse opal structures-fundamentals and applications from optics to energy storage, *J. Mater. Chem. C.* 3 (2015) 6109–6143. <https://doi.org/10.1039/c5tc01083g>.
- [7] Z. Li, M. Xiao, Y.F. Liu, H.H. Gao, P. V. Braun, Three-dimensional mesostructured binder-free nickel-based TiO₂/RGO lithium-ion battery negative electrodes with enhanced volumetric capacity, *Ceram. Int.* 47 (2021) 21381–21387. <https://doi.org/10.1016/j.ceramint.2021.04.147>.
- [8] B.H. Patil, K. Jang, S. Lee, J.H. Kim, C.S. Yoon, J. Kim, D.H. Kim, H. Ahn, Periodically ordered inverse opal TiO₂/polyaniline core/shell design for electrochemical energy storage applications, *J. Alloys Compd.* 694 (2017) 111–118. <https://doi.org/10.1016/j.jallcom.2016.09.331>.

- [9] J. Jiang, C. Li, S. Zhu, Z. Chen, M. Fu, D. He, Y. Wang, Optical properties of PMMA inverse opal structures with anisotropic geometries by stretching, *Mater. Res. Express.* 7 (2020) 0–6. <https://doi.org/10.1088/2053-1591/ab88fe>.
- [10] A. Lonergan, D. McNulty, C. O'Dwyer, Tetrahedral framework of inverse opal photonic crystals defines the optical response and photonic band gap, *J. Appl. Phys.* 124 (2018). <https://doi.org/10.1063/1.5033367>.
- [11] N. Abid, A.M. Khan, S. Shujait, K. Chaudhary, M. Ikram, M. Imran, J. Haider, M. Khan, Q. Khan, M. Maqbool, Synthesis of nanomaterials using various top-down and bottom-up approaches, influencing factors, advantages, and disadvantages: A review, *Adv. Colloid Interface Sci.* 300 (2022) 102597. <https://doi.org/10.1016/j.cis.2021.102597>.
- [12] H. Shahi, J. Kaur, S. Vaidya, Designing Nanostructured Materials through Self-Assembly and their Applications, *J. Inst. Eng. Ser. C.* 103 (2022) 135–142. <https://doi.org/10.1007/s40032-021-00660-4>.
- [13] J.E.S. Van Der Hoeven, A. V. Shneidman, N.J. Nicolas, J. Aizenberg, Evaporation-Induced Self-Assembly of Metal Oxide Inverse Opals: From Synthesis to Applications, *Acc. Chem. Res.* 55 (2022) 1809–1820. <https://doi.org/10.1021/acs.accounts.2c00087>.
- [14] D.A. Santamaría Razo, L. Pallavidino, E. Garrone, F. Geobaldo, E. Descrovi, A. Chiodoni, F. Giorgis, A version of Stöber synthesis enabling the facile prediction of silica nanospheres size for the fabrication of opal photonic crystals, *J. Nanoparticle Res.* 10 (2008) 1225–1229. <https://doi.org/10.1007/s11051-008-9373-4>.
- [15] F. Meseguer, A. Blanco, H. Míguez, F. García-Santamaría, M. Ibisate, C. López, Synthesis of inverse opals, *Colloids Surfaces A Physicochem. Eng. Asp.* 202 (2002) 281–290. [https://doi.org/10.1016/S0927-7757\(01\)01084-6](https://doi.org/10.1016/S0927-7757(01)01084-6).
- [16] B.Y. Valles-Pérez, M.A. Badillo-Ávila, G. Torres-Delgado, R. Castanedo-Pérez, O. Zelaya-Ángel, Photocatalytic activity of ZnO + CuO thin films deposited by dip coating: coupling effect between oxides, *J. Sol-Gel Sci. Technol.* 93 (2020) 517–526. <https://doi.org/10.1007/s10971-020-05223-0>.
- [17] C.C. Chiang, L.D. Tuyen, C.R. Ren, L.K. Chau, C.Y. Wu, P.J. Huang, C.C. Hsu, Fabrication of titania inverse opals by multi-cycle dip-infiltration for optical sensing, *Photonics Nanostructures - Fundam. Appl.* 19 (2016) 48–54.

<https://doi.org/10.1016/j.photonics.2016.02.004>.

- [18] A. Di Mauro, M.E. Fragalà, V. Privitera, G. Impellizzeri, ZnO for application in photocatalysis: From thin films to nanostructures, *Mater. Sci. Semicond. Process.* 69 (2017) 44–51. <https://doi.org/10.1016/j.mssp.2017.03.029>.
- [19] L. Sun, G. Yuan, L. Gao, J. Yang, M. Chhowalla, M.H. Gharahcheshmeh, K.K. Gleason, Y.S. Choi, B.H. Hong, Z. Liu, Chemical vapour deposition, *Nat. Rev. Methods Prim.* 1 (2021). <https://doi.org/10.1038/s43586-020-00005-y>.
- [20] Y. Zhou, J. Zhao, Y. Liu, R.J.H. Ng, J.K.W. Yang, Optical and electrochemical properties of 3D nanoporous Cu₂O–Cu inverse opal structures tuned by electrodeposition, *Mater. Sci. Semicond. Process.* 121 (2021). <https://doi.org/10.1016/j.mssp.2020.105444>.
- [21] S. Koussi-Daoud, O. Majerus, D. Schaming, T. Pauporté, Electrodeposition of NiO Films and Inverse Opal Organized Layers from Polar Aprotic Solvent-Based Electrolyte, *Electrochim. Acta.* 219 (2016) 638–646. <https://doi.org/10.1016/j.electacta.2016.10.074>.
- [22] V. Abramova, A. Sinitskii, Large-scale ZnO inverse opal films fabricated by a sol-gel technique, *Superlattices Microstruct.* 45 (2009) 624–629. <https://doi.org/10.1016/j.spmi.2009.03.003>.
- [23] X. Zhang, G.J. Blanchard, Polymer sol-gel composite inverse opal structures, *ACS Appl. Mater. Interfaces.* 7 (2015) 6054–6061. <https://doi.org/10.1021/acsami.5b00656>.
- [24] R.C. Schroden, M. Al-Daous, C.F. Blanford, A. Stein, Optical properties of inverse opal photonic crystals, *Chem. Mater.* 14 (2002) 3305–3315. <https://doi.org/10.1021/cm020100z>.
- [25] X.P. Li, L.L. Wang, Z.L. Gong, X.F. Wang, Y.M. Zhou, Preparation of inverse opal Zirconia, *Sci. Sinter.* 50 (2018) 387–394. <https://doi.org/10.2298/SOS1803387L>.
- [26] G. Collins, M. Blömker, M. Osiak, J.D. Holmes, M. Bredol, C. O’Dwyer, Three-dimensionally ordered hierarchically porous tin dioxide inverse opals and immobilization of palladium nanoparticles for catalytic applications, *Chem. Mater.* 25 (2013) 4312–4320. <https://doi.org/10.1021/cm402458v>.
- [27] L. Li, X. Huang, J. Zhang, W. Zhang, F. Ma, Z. Xiao, S. Gai, D. Wang, N. Li, Multi-

- layer three-dimensionally ordered Bismuth trioxide/Titanium dioxide nanocomposite: Synthesis and enhanced photocatalytic activity, *J. Colloid Interface Sci.* 443 (2015) 13–22. <https://doi.org/10.1016/j.jcis.2014.11.062>.
- [28] M. Zalfani, B. van der Schueren, M. Mahdouani, R. Bourguiga, W.B. Yu, M. Wu, O. Deparis, Y. Li, B.L. Su, ZnO quantum dots decorated 3DOM TiO₂ nanocomposites: Symbiose of quantum size effects and photonic structure for highly enhanced photocatalytic degradation of organic pollutants, *Appl. Catal. B Environ.* 199 (2016) 187–198. <https://doi.org/10.1016/j.apcatb.2016.06.016>.
- [29] G.I.N. Waterhouse, M.R. Waterland, Opal and inverse opal photonic crystals: Fabrication and characterization, *Polyhedron.* 26 (2007) 356–368. <https://doi.org/10.1016/j.poly.2006.06.024>.
- [30] X. Zhang, C. Weinberger, S. Amrehn, X. Wu, M. Tiemann, T. Wagner, Synthesis of Metal Oxide Inverse Opals from Metal Nitrates by PMMA Colloidal Crystal Templating, *Eur. J. Inorg. Chem.* 2020 (2020) 3402–3407. <https://doi.org/10.1002/ejic.202000517>.
- [31] M.C. Orilall, N.M. Abrams, J. Lee, F.J. DiSalvo, U. Wiesner, Highly crystalline inverse opal transition metal oxides via a combined assembly of soft and hard chemistries, *J. Am. Chem. Soc.* 130 (2008) 8882–8883. <https://doi.org/10.1021/ja802093u>.
- [32] J. Liu, X. Zhang, W. Li, C. Jiang, Z. Wang, X. Xiao, Recent progress in periodic patterning fabricated by self-assembly of colloidal spheres for optical applications, *Sci. China Mater.* 63 (2020) 1418–1437. <https://doi.org/10.1007/s40843-020-1284-8>.
- [33] J. Long, M. Fu, C. Li, C. Sun, D. He, Y. Wang, High-quality ZnO inverse opals and related heterostructures as photocatalysts produced by atomic layer deposition, *Appl. Surf. Sci.* 454 (2018) 112–120. <https://doi.org/10.1016/j.apsusc.2018.05.160>.
- [34] S.R. Kousik, D. Sipp, K. Abitaev, Y. Li, T. Sottmann, K. Koynov, P. Atanasova, From macro to mesoporous zno inverse opals: Synthesis, characterization and tracer diffusion properties, *Nanomaterials.* 11 (2021) 1–18. <https://doi.org/10.3390/nano11010196>.
- [35] R. Mudi, A. Carpentiero, M. Bollani, M. Barozzi, K. Debnath, A. Chiappini, B.N.S. Bhaktha, Inverse opal optical Tamm state for sensing applications, *Photonics Nanostructures - Fundam. Appl.* 62 (2024) 101315.

<https://doi.org/10.1016/j.photonics.2024.101315>.

- [36] J. Gao, W. Tian, H. Zhang, S. Wang, Engineered inverse opal structured semiconductors for solar light-driven environmental catalysis, *Nanoscale*. (2022) 14341–14367. <https://doi.org/10.1039/d2nr03924a>.
- [37] M. Zhou, Y. Xu, C. Wang, Q. Li, J. Xiang, L. Liang, M. Wu, H. Zhao, Y. Lei, Amorphous TiO₂ inverse opal anode for high-rate sodium ion batteries, *Nano Energy*. 31 (2017) 514–524. <https://doi.org/10.1016/j.nanoen.2016.12.005>.
- [38] V. Likodimos, Photonic crystal-assisted visible light activated TiO₂ photocatalysis, *Appl. Catal. B Environ.* 230 (2018) 269–303. <https://doi.org/10.1016/j.apcatb.2018.02.039>.
- [39] M.N. Armenise, C.E. Campanella, C. Ciminelli, F. Dell’Olio, V.M.N. Passaro, Phononic and photonic band gap structures: Modelling and applications, *Phys. Procedia*. 3 (2010) 357–364. <https://doi.org/10.1016/j.phpro.2010.01.047>.
- [40] E. Armstrong, C. O’Dwyer, Artificial opal photonic crystals and inverse opal structures—fundamentals and applications from optics to energy storage, *J. Mater. Chem. C*. 3 (2015) 6109–6143. <https://doi.org/10.1039/c5tc01083g>.
- [41] S. Meng, D. Li, P. Wang, X. Zheng, J. Wang, J. Chen, J. Fang, X. Fu, Probing photonic effect on photocatalytic degradation of dyes based on 3D inverse opal ZnO photonic crystal, *RSC Adv.* 3 (2013) 17021–17028. <https://doi.org/10.1039/c3ra42618a>.
- [42] J. Liu, J. Jin, Y. Li, H.W. Huang, C. Wang, M. Wu, L.H. Chen, B.L. Su, Tracing the slow photon effect in a ZnO inverse opal film for photocatalytic activity enhancement, *J. Mater. Chem. A*. 2 (2014) 5051–5059. <https://doi.org/10.1039/c3ta15044e>.
- [43] T. Raja-Mogan, B. Ohtani, E. Kowalska, Photonic crystals for plasmonic photocatalysis, *Catalysts*. 10 (2020) 1–20. <https://doi.org/10.3390/catal10080827>.
- [44] T. Baba, Slow light in photonic crystals, *Nat. Photonics*. 2 (2008) 465–473. <https://doi.org/10.1038/nphoton.2008.146>.
- [45] J.H. Han, A. V. Shneidman, D.Y. Kim, N.J. Nicolas, J.E.S. van der Hoeven, M. Aizenberg, J. Aizenberg, Highly Ordered Inverse Opal Structures Synthesized from Shape-Controlled Nanocrystal Building Blocks, *Angew. Chemie - Int. Ed.* 61 (2022) 1–9. <https://doi.org/10.1002/anie.202111048>.

- [46] M. Wu, J. Jin, J. Liu, Z. Deng, Y. Li, O. Deparis, B.L. Su, High photocatalytic activity enhancement of titania inverse opal films by slow photon effect induced strong light absorption, *J. Mater. Chem. A.* 1 (2013) 15491–15500. <https://doi.org/10.1039/c3ta13574h>.
- [47] D. Pan, L. Ma, Y. Xie, T.C. Jen, C. Yuan, On the physical and chemical details of alumina atomic layer deposition: A combined experimental and numerical approach, *J. Vac. Sci. Technol. A Vacuum, Surfaces, Film.* 33 (2015). <https://doi.org/10.1116/1.4905726>.
- [48] S.K. Karuturi, L.J. Liu, L.T. Su, W. Bin Niu, A.L.Y. Tok, Atomic layer deposition of inverse opals for solar cell applications, *Adv. Mater. Res.* 789 (2013) 3–7. <https://doi.org/10.4028/www.scientific.net/AMR.789.3>.
- [49] F. Fathi, H. Monirinasab, F. Ranjbary, K. Nejati-Koshki, Inverse opal photonic crystals: Recent advances in fabrication methods and biological applications, *J. Drug Deliv. Sci. Technol.* 72 (2022) 103377. <https://doi.org/10.1016/j.jddst.2022.103377>.
- [50] K. Pham, S. Pelisset, N. Kinnunen, P. Karvinen, T.K. Hakala, J.J. Saarinen, Controlled photocatalytic activity of TiO₂ inverse opal structures with atomic layer deposited (ALD) metal oxide thin films, *Mater. Chem. Phys.* 277 (2022) 0–5. <https://doi.org/10.1016/j.matchemphys.2021.125533>.
- [51] H.B. Profijt, S.E. Potts, M.C.M. van de Sanden, W.M.M. Kessels, Plasma-Assisted Atomic Layer Deposition: Basics, Opportunities, and Challenges, *J. Vac. Sci. Technol. A Vacuum, Surfaces, Film.* 29 (2011). <https://doi.org/10.1116/1.3609974>.
- [52] H. Kim, Characteristics and applications of plasma enhanced-atomic layer deposition, *Thin Solid Films.* 519 (2011) 6639–6644. <https://doi.org/10.1016/j.tsf.2011.01.404>.
- [53] H. Kim, I.K. Oh, Review of plasma-enhanced atomic layer deposition: Technical enabler of nanoscale device fabrication, *Jpn. J. Appl. Phys.* 53 (2014). <https://doi.org/10.7567/JJAP.53.03DA01>.
- [54] M. van de Poll, J. Shen, J. Hilfiker, M. Verheijen, P. Poodt, F. van den Bruele, W. Kessels, B. Macco, Plasma-Enhanced Spatial Atomic Layer Deposition on 2D and 3D Surface Topologies: The Case of Amorphous and Crystalline TiO₂, *J. Phys. Chem. C.* (2025). <https://doi.org/10.1021/acs.jpcc.4c08281>.

- [55] P. Schindler, M. Logar, J. Provine, F.B. Prinz, Enhanced step coverage of TiO₂ deposited on high aspect ratio surfaces by plasma-enhanced atomic layer deposition, *Langmuir*. 31 (2015) 5057–5062. <https://doi.org/10.1021/acs.langmuir.5b00216>.
- [56] M. Van Daele, M.B.E. Gri, A. Raza, M.M. Minjauw, E. Solano, R. Baets, T. Barry, J. Feng, R.K. Ramachandran, C. Detavernier, J. Dendooven, Plasma-Enhanced Atomic Layer Deposition of Nanostructured Gold Near Room Temperature, (2019). <https://doi.org/10.1021/acsami.9b10848>.
- [57] C. Hedrich, N.T. James, L.G. Maragno, V. de Lima, S.Y.G. González, R.H. Blick, R. Zierold, K.P. Furlan, Enhanced Photocatalytic Properties and Photoinduced Crystallization of TiO₂-Fe₂O₃ Inverse Opals Fabricated by Atomic Layer Deposition, *ACS Appl. Mater. Interfaces*. 16 (2024) 46964–46974. <https://doi.org/10.1021/acsami.4c10831>.
- [58] N. Justh, L.P. Bakos, K. Hernádi, G. Kiss, B. Réti, Z. Erdélyi, B. Párditka, I.M. Szilágyi, Photocatalytic hollow TiO₂ and ZnO nanospheres prepared by atomic layer deposition, *Sci. Rep.* 7 (2017) 2–10. <https://doi.org/10.1038/s41598-017-04090-0>.
- [59] R. Lo Nigro, E. Schilirò, G. Mannino, S. Di Franco, F. Roccaforte, Comparison between thermal and plasma enhanced atomic layer deposition processes for the growth of HfO₂ dielectric layers, *J. Cryst. Growth*. 539 (2020) 125624. <https://doi.org/10.1016/j.jcrysgro.2020.125624>.
- [60] M.R. Saleem, S. Honkanen, J. Turunen, Thermal properties of TiO₂ films fabricated by atomic layer deposition, *IOP Conf. Ser. Mater. Sci. Eng.* 60 (2014). <https://doi.org/10.1088/1757-899X/60/1/012008>.
- [61] C. Detavernier, D. Deduytsche, J. Musschoot, J. Dendooven, Thermal Versus Plasma-Enhanced ALD: Growth Kinetics and Conformality, *ECS Meet. Abstr.* MA2008-02 (2008) 1913–1913. <https://doi.org/10.1149/ma2008-02/24/1913>.
- [62] S.B.S. Heil, J.L. Van Hemmen, M.C.M. Van De Sanden, W.M.M. Kessels, Reaction mechanisms during plasma-assisted atomic layer deposition of metal oxides: A case study for Al₂O₃, *J. Appl. Phys.* 103 (2008). <https://doi.org/10.1063/1.2924406>.
- [63] P.R. Varadwaj, V.A. Dinh, Y. Morikawa, R. Asahi, Polymorphs of Titanium Dioxide: An Assessment of the Variants of Projector Augmented Wave Potential of Titanium on

- Their Geometric and Dielectric Properties, *ACS Omega*. 8 (2023) 22003–22017. <https://doi.org/10.1021/acsomega.3c02038>.
- [64] C.Y. Hsu, Z.H. Mahmoud, S. Abdullaev, F.K. Ali, Y. Ali Naeem, R. Mzahim Mizher, M. Morad Karim, A.S. Abdulwahid, Z. Ahmadi, S. Habibzadeh, E. Kianfar, Nano titanium oxide (nano-TiO₂): A review of synthesis methods, properties, and applications, *Case Stud. Chem. Environ. Eng.* 9 (2024) 100626. <https://doi.org/10.1016/j.cscee.2024.100626>.
- [65] A.J. Haider, Z.N. Jameel, I.H.M. Al-Hussaini, Review on: Titanium dioxide applications, *Energy Procedia*. 157 (2019) 17–29. <https://doi.org/10.1016/j.egypro.2018.11.159>.
- [66] J. Yu, J. Lei, L. Wang, J. Zhang, Y. Liu, TiO₂ inverse opal photonic crystals: Synthesis, modification, and applications - A review, *J. Alloys Compd.* 769 (2018) 740–757. <https://doi.org/10.1016/j.jallcom.2018.07.357>.
- [67] F. Temerov, B. Ankudze, J.J. Saarinen, TiO₂ inverse opal structures with facile decoration of precious metal nanoparticles for enhanced photocatalytic activity, *Mater. Chem. Phys.* 242 (2020) 2–7. <https://doi.org/10.1016/j.matchemphys.2019.122471>.
- [68] P. Bernal, M.C. Marco de Lucas, I. Pochard, B. Domenichini, L. Imhoff, Photocatalytic properties of atomic layer deposited TiO₂ inverse opals and planar films for the degradation of dyes, *Appl. Surf. Sci.* 512 (2020) 145693. <https://doi.org/10.1016/j.apsusc.2020.145693>.
- [69] H. Hu, B. Dong, H. Hu, F. Chen, M. Kong, Q. Zhang, T. Luo, L. Zhao, Z. Guo, J. Li, Z. Xu, S. Wang, D. Eder, L. Wan, Atomic Layer Deposition of TiO₂ for a High-Efficiency Hole-Blocking Layer in Hole-Conductor-Free Perovskite Solar Cells Processed in Ambient Air, *ACS Appl. Mater. Interfaces*. 8 (2016) 17999–18007. <https://doi.org/10.1021/acsomega.6b02701>.
- [70] L. Bertel, D.A. Miranda, J.M. García-martín, Nanostructured titanium dioxide surfaces for electrochemical biosensing, *Sensors*. 21 (2021). <https://doi.org/10.3390/s21186167>.
- [71] A. Zulfiqar, F. Temerov, J.J. Saarinen, Multilayer TiO₂ Inverse Opal with Gold Nanoparticles for Enhanced Photocatalytic Activity, *ACS Omega*. 5 (2020) 11595–11604. <https://doi.org/10.1021/acsomega.0c00833>.

- [72] P. Birnal, M.C. Marco de Lucas, I. Pochard, F. Herbst, O. Heintz, L. Saviot, B. Domenichini, L. Imhoff, Visible-light photocatalytic degradation of dyes by TiO₂-Au inverse opal films synthesized by Atomic Layer Deposition, *Appl. Surf. Sci.* 609 (2023). <https://doi.org/10.1016/j.apsusc.2022.155213>.
- [73] C.X. Lei, X.M. Liu, J. Han, B. Bin Ma, L.Y. Chen, H. Fu, J.J. Sun, J. Zuo, H.A. Zhang, G.S. Zhang, Enhanced photocatalytic activity of spherical TiO₂ inverse opal photonic crystals decorated by Ag nanoparticles, *J. Porous Mater.* (2025). <https://doi.org/10.1007/s10934-025-01768-z>.
- [74] Z. Hu, L. Xu, L. Wang, Y. Huang, L. Xu, J. Chen, One-step fabrication of N-doped TiO₂ inverse opal films with visible light photocatalytic activity, *Catal. Commun.* 40 (2013) 106–110. <https://doi.org/10.1016/j.catcom.2013.06.010>.
- [75] J. Xu, B. Yang, M. Wu, Z. Fu, Y. Lv, Y. Zhao, Novel N-F-codoped TiO₂ inverse opal with a hierarchical meso-/macroporous structure: Synthesis, characterization, and photocatalysis, *J. Phys. Chem. C.* 114 (2010) 15251–15259. <https://doi.org/10.1021/jp101168y>.
- [76] K. Pham, F. Temerov, J.J. Saarinen, Multicomponent inverse opal structures with gold nanoparticles for visible light photocatalytic activity, *Mater. Des.* 194 (2020). <https://doi.org/10.1016/j.matdes.2020.108886>.
- [77] J. Wang, R. Chen, L. Xiang, S. Komarneni, Synthesis, properties and applications of ZnO nanomaterials with oxygen vacancies: A review, *Ceram. Int.* 44 (2018) 7357–7377. <https://doi.org/10.1016/j.ceramint.2018.02.013>.
- [78] M.J. Haque, M.M. Bellah, M.R. Hassan, S. Rahman, Synthesis of ZnO nanoparticles by two different methods & comparison of their structural, antibacterial, photocatalytic and optical properties, *Nano Express.* 1 (2020). <https://doi.org/10.1088/2632-959X/ab7a43>.
- [79] S. Dey, D. lochan Mohanty, N. Divya, V. Bakshi, A. Mohanty, D. Rath, S. Das, A. Mondal, S. Roy, R. Sabui, A critical review on zinc oxide nanoparticles: Synthesis, properties and biomedical applications, *Intell. Pharm.* 3 (2024) 53–70. <https://doi.org/10.1016/j.ipha.2024.08.004>.
- [80] F. Güell, A. Galdámez-Martínez, P.R. Martínez-Alanis, A.C. Catto, L.F. da Silva, V.R. Mastelaro, G. Santana, A. Dutt, ZnO-based nanomaterials approach for photocatalytic

- and sensing applications: recent progress and trends, *Mater. Adv.* 4 (2023) 3685–3707. <https://doi.org/10.1039/d3ma00227f>.
- [81] J. Cai, Z. Ma, U. Wejinya, M. Zou, Y. Liu, H. Zhou, X. Meng, A revisit to atomic layer deposition of zinc oxide using diethylzinc and water as precursors, *J. Mater. Sci.* 54 (2019) 5236–5248. <https://doi.org/10.1007/s10853-018-03260-3>.
- [82] O.Y. Ramírez-Esquivel, D.A. Mazón-Montijo, D. Cabrera-German, E. Martínez-Guerra, Z. Montiel-González, Atomic layer deposition supercycle approach applied to the Al-doping of nearly saturated ZnO surfaces, *Ceram. Int.* 47 (2021) 7126–7134. <https://doi.org/10.1016/j.ceramint.2020.11.066>.
- [83] S.I. Boyadjiev, V. Georgieva, R. Yordanov, Z. Raicheva, I.M. Szilágyi, Preparation and characterization of ALD deposited ZnO thin films studied for gas sensors, *Appl. Surf. Sci.* 387 (2016) 1230–1235. <https://doi.org/10.1016/j.apsusc.2016.06.007>.
- [84] X. Sun, C. Zhou, M. Xie, H. Sun, T. Hu, F. Lu, S.M. Scott, S.M. George, J. Lian, Synthesis of ZnO quantum dot/graphene nanocomposites by atomic layer deposition with high lithium storage capacity, *J. Mater. Chem. A.* 2 (2014) 7319–7326. <https://doi.org/10.1039/c4ta00589a>.
- [85] S.H. Han, R.E. Agbenyeke, G.Y. Lee, B.K. Park, C.G. Kim, Y.K. Lee, S.U. Son, T.M. Chung, Synthesis and characterization of novel zinc precursors for ZnO thin film deposition by atomic layer deposition, *Dalt. Trans.* 49 (2020) 4306–4314. <https://doi.org/10.1039/c9dt04644e>.
- [86] S. Sinha, D.K. Nandi, S. Kim, J. Heo, Solar Energy Materials and Solar Cells Atomic-layer-deposited buffer layers for thin film solar cells using earth-abundant absorber materials: A review, *Solar Energy* 176 (2018) 49–68.
- [87] J. Tian, L. Chen, J. Dai, X. Wang, Y. Yin, P. Wu, Preparation and characterization of TiO₂, ZnO, and TiO₂/ZnO nanofilms via sol-gel process, *Ceram. Int.* 35 (2009) 2261–2270. <https://doi.org/10.1016/j.ceramint.2008.12.010>.
- [88] L. Gao, S. Li, D. Huang, Y. Shen, M. Wang, ZnO decorated TiO₂ nanosheet composites for lithium ion battery, *Electrochim. Acta.* 182 (2015) 529–536. <https://doi.org/10.1016/j.electacta.2015.09.108>.
- [89] C.C. Wang, C.Y. Chou, S.R. Yi, H.D. Chen, Deposition of heterojunction of ZnO on

- hydrogenated TiO₂ nanotube arrays by atomic layer deposition for enhanced photoelectrochemical water splitting, *Int. J. Hydrogen Energy*. 44 (2019) 28685–28697. <https://doi.org/10.1016/j.ijhydene.2019.09.133>.
- [90] E. Biehler, R. Whiteman, P. Lin, K. Zhang, H. Baumgart, T.M. Abdel-Fattah, Controlled Synthesis of ZnO Nanorods Using Different Seed Layers, *ECS J. Solid State Sci. Technol.* 9 (2020) 121008. <https://doi.org/10.1149/2162-8777/abcb60>.
- [91] C. Yang, Q. Li, ZnO inverse opals with deposited Ag nanoparticles: Fabrication, characterization and photocatalytic activity under visible light irradiation, *J. Photochem. Photobiol. A Chem.* 371 (2019) 118–127. <https://doi.org/10.1016/j.jphotochem.2018.10.039>.
- [92] Z. Wu, M. Fu, X. Liu, J. Li, C. Wei, Y. Zhang, Y. Ning, D. He, Y. Wang, Boosting the photocathode performances of protected Cu₂O inverse opals using photonic-crystal heterostructures, *Appl. Surf. Sci.* 644 (2024). <https://doi.org/10.1016/j.apsusc.2023.158792>.
- [93] M.S. Amin, F.M. Alshareef, W.T. Alsaggaf, Z.I. Zaki, Employing manufactured Mn₃O₄–ZnO nanocomposite for ameliorated photocatalytic performance under visible light, *Opt. Mater. (Amst)*. 127 (2022). <https://doi.org/10.1016/j.optmat.2022.112286>.
- [94] J. Zhang, H. Yang, Q.L. Zhang, S. Dong, J.K. Luo, Structural, optical, electrical and resistive switching properties of ZnO thin films deposited by thermal and plasma-enhanced atomic layer deposition, *Appl. Surf. Sci.* 282 (2013) 390–395. <https://doi.org/10.1016/j.apsusc.2013.05.141>.
- [95] A. Jiamprasertboon, A. Kafizas, M. Sachs, M. Ling, A.M. Alotaibi, Y. Lu, T. Siritanon, I.P. Parkin, C.J. Carmalt, Heterojunction α -Fe₂O₃/ZnO Films with Enhanced Photocatalytic Properties Grown by Aerosol-Assisted Chemical Vapour Deposition, *Chem. - A Eur. J.* 25 (2019) 11337–11345. <https://doi.org/10.1002/chem.201902175>.
- [96] M.A. Trunov, M. Schoenitz, X. Zhu, E.L. Dreizin, Effect of polymorphic phase transformations in Al₂O₃ film on oxidation kinetics of aluminum powders, *Combust. Flame*. 140 (2005) 310–318. <https://doi.org/10.1016/j.combustflame.2004.10.010>.
- [97] M.G. Baronskiy, S. V. Tsybulya, A.I. Kostyukov, A. V. Zhuzhgov, V.N. Snytnikov, Structural properties investigation of different alumina polymorphs (η -, γ -, χ -, θ -, α -

- Al₂O₃) using Cr³⁺ as a luminescent probe, *J. Lumin.* 242 (2022) 118554. <https://doi.org/10.1016/j.jlumin.2021.118554>.
- [98] E. Langereis, M. Bouman, J. Keijmel, M.C. Van de Sanden, W.M. Kessels, Plasma-assisted ALD of Al₂O₃ at Low Temperatures: Reaction Mechanisms and Material Properties, *ECS Meet. Abstr.* MA2008-02 (2008) 1914–1914. <https://doi.org/10.1149/ma2008-02/24/1914>.
- [99] L. Zhang, H.C. Jiang, C. Liu, J.W. Dong, P. Chow, Annealing of Al₂O₃ thin films prepared by atomic layer deposition, *J. Phys. D. Appl. Phys.* 40 (2007) 3707–3713. <https://doi.org/10.1088/0022-3727/40/12/025>.
- [100] S.S. Shenouda, M.S.A. Hussien, B. Parditka, A. Csík, V. Takats, Z. Erdélyi, Novel amorphous Al-rich Al₂O₃ ultra-thin films as active photocatalysts for water treatment from some textile dyes, *Ceram. Int.* 46 (2020) 7922–7929. <https://doi.org/10.1016/j.ceramint.2019.12.012>.
- [101] K.P. Furlan, R.M. Pasquarelli, T. Krekeler, M. Ritter, R. Zierold, K. Nielsch, G.A. Schneider, R. Janssen, Highly porous α -Al₂O₃ ceramics obtained by sintering atomic layer deposited inverse opals, *Ceram. Int.* 43 (2017) 11260–11264. <https://doi.org/10.1016/j.ceramint.2017.05.176>.
- [102] G.I.N. Waterhouse, W.T. Chen, A. Chan, H. Jin, D. Sun-Waterhouse, B.C.C. Cowie, Structural, optical, and catalytic support properties of γ -Al₂O₃ inverse opals, *J. Phys. Chem. C.* 119 (2015) 6647–6659. <https://doi.org/10.1021/acs.jpcc.5b00437>.
- [103] F. Gallego-Gómez, M. Ibisate, D. Golmayo, F.J. Palomares, M. Herrera, J. Hernández, S.I. Molina, Á. Blanco, C. López, Light emission from nanocrystalline Si inverse opals and controlled passivation by atomic layer deposited Al₂O₃, *Adv. Mater.* 23 (2011) 5219–5223. <https://doi.org/10.1002/adma.201101797>.
- [104] A. Coll, S. Bermejo, D. Hernández, L. Castañer, Al₂O₃/TiO₂ inverse opals from electrosprayed self-assembled templates, *Beilstein J. Nanotechnol.* 9 (2018) 216–223. <https://doi.org/10.3762/bjnano.9.23>.
- [105] E. Graugnard, J.S. King, D.P. Gaillot, C.J. Summers, Sacrificial-layer atomic layer deposition for fabrication of non-close-packed inverse-opal photonic crystals, *Adv. Funct. Mater.* 16 (2006) 1187–1196. <https://doi.org/10.1002/adfm.200500841>.

- [106] J. López, E. Solorio, H.A. Borbón-Nuñez, F.F. Castellón, R. Machorro, N. Nedev, M.H. Farías, H. Tiznado, Refractive index and bandgap variation in Al₂O₃-ZnO ultrathin multilayers prepared by atomic layer deposition, *J. Alloys Compd.* 691 (2017) 308–315. <https://doi.org/10.1016/j.jallcom.2016.08.271>.
- [107] M. Nasr, R. Viter, C. Eid, R. Habchi, P. Miele, M. Bechelany, Optical and structural properties of Al₂O₃ doped ZnO nanotubes prepared by ALD and their photocatalytic application, *Surf. Coatings Technol.* 343 (2018) 24–29. <https://doi.org/10.1016/j.surfcoat.2017.11.060>.
- [108] K. Wenderich, G. Mul, Methods, Mechanism, and Applications of Photodeposition in Photocatalysis: A Review, *Chem. Rev.* 116 (2016) 14587–14619. <https://doi.org/10.1021/acs.chemrev.6b00327>.
- [109] S. Mishra, B. Sundaram, A review of the photocatalysis process used for wastewater treatment, *Mater. Today Proc.* 102 (2023) 393–409. <https://doi.org/10.1016/j.matpr.2023.07.147>.
- [110] M. Curti, J. Schneider, D.W. Bahnemann, C.B. Mendive, Inverse Opal Photonic Crystals as a Strategy to Improve Photocatalysis: Underexplored Questions, *J. Phys. Chem. Lett.* 6 (2015) 3903–3910. <https://doi.org/10.1021/acs.jpcclett.5b01353>.
- [111] J. Liu, H. Zhao, M. Wu, B. Van der Schueren, Y. Li, O. Deparis, J. Ye, G.A. Ozin, T. Hasan, B.L. Su, Slow Photons for Photocatalysis and Photovoltaics, *Adv. Mater.* 29 (2017) 1–21. <https://doi.org/10.1002/adma.201605349>.
- [112] S. Boonphan, S. Prachakiew, C. Nontakoat, Y. Keereeta, C. Boonruang, A. Klinbumrung, South African Journal of Chemical Engineering Crystallographic defects induced F-Center and optical enhancements in, 52 (2025) 68–79. <https://doi.org/10.1016/j.sajce.2025.01.010>.
- [113] H. Khan, M.U.H. Shah, Modification strategies of TiO₂ based photocatalysts for enhanced visible light activity and energy storage ability: A review, *J. Environ. Chem. Eng.* 11 (2023). <https://doi.org/10.1016/j.jece.2023.111532>.
- [114] A. Rafiq, M. Ikram, S. Ali, F. Niaz, M. Khan, Q. Khan, M. Maqbool, Photocatalytic degradation of dyes using semiconductor photocatalysts to clean industrial water pollution, *J. Ind. Eng. Chem.* 97 (2021) 111–128.

<https://doi.org/10.1016/j.jiec.2021.02.017>.

- [115] M.K.H.M. Nazri, N. Sapawe, A short review on photocatalytic toward dye degradation, *Mater. Today Proc.* 31 (2020) A42–A47. <https://doi.org/10.1016/j.matpr.2020.10.967>.
- [116] L.P. Bakos, D. Karajz, A. Katona, K. Hernadi, B. Parditka, Z. Erdélyi, I. Lukács, Z. Hórvölgyi, G. Szitási, I.M. Szilágyi, Carbon nanosphere templates for the preparation of inverse opal titania photonic crystals by atomic layer deposition, *Appl. Surf. Sci.* 504 (2020). <https://doi.org/10.1016/j.apsusc.2019.144443>.
- [117] J. Wang, Y. Wan, X. Wang, Y. Pu, N. Ali, S. Yuan, Q. Zhang, M. Bilal, Fabrication and characterization of inverse opal tin dioxide as a novel and high-performance photocatalyst for degradation of Rhodamine B dye, *Inorg. Nano-Metal Chem.* 51 (2021) 150–158. <https://doi.org/10.1080/24701556.2020.1769664>.
- [118] J. Xu, B.F. Yang, Z.P. Fu, M.W. Wen, Y.X. Zhao, Synthesis and photocatalytic property of ZnO/TiO₂ inverse opals films with controllable composition and topology, *Chinese J. Chem. Phys.* 25 (2012) 235–241. <https://doi.org/10.1088/1674-0068/25/02/235-241>.
- [119] K. Pham, F. Temerov, J.J. Saarinen, Multicomponent inverse opal structures with gold nanoparticles for visible light photocatalytic activity, *Mater. Des.* 194 (2020) 108886. <https://doi.org/10.1016/j.matdes.2020.108886>.
- [120] R. Yew, S.K. Karuturi, J. Liu, H.H. Tan, Y. Wu, C. Jagadish, Exploiting defects in TiO₂ inverse opal for enhanced photoelectrochemical water splitting, *Opt. Express.* 27 (2019) 761. <https://doi.org/10.1364/oe.27.000761>.
- [121] Y. Zeng, T. Yang, C. Li, A. Xie, S. Li, M. Zhang, Y. Shen, Zn_xCd_{1-x}Se nanoparticles decorated ordered mesoporous ZnO inverse opal with binder-free heterojunction interfaces for highly efficient photoelectrochemical water splitting, *Appl. Catal. B Environ.* 245 (2019) 469–476. <https://doi.org/10.1016/j.apcatb.2019.01.011>.
- [122] B.H. Xiao, C. Huo, J.Y. Chen, Y.G. Xiao, S.S. Cao, Z.Q. Liu, Inverse opal anatase/rutile TiO₂ multi-heterojunctions enable efficient photoelectrochemical water splitting, *Chem. Sci.* (2025). <https://doi.org/10.1039/d4sc07901a>.
- [123] X. Chai, H. Zhang, C. Cheng, 3D FTO Inverse Opals@Hematite@TiO₂ hierarchically structured Photoanode for Photoelectrochemical Water Splitting, *Semicond. Sci. Technol.* 32 (2017). <https://doi.org/10.1088/1361-6641/aa8b2e>.

- [124] M. Zhou, J. Bao, Y. Xu, J. Zhang, J. Xie, M. Guan, C. Wang, L. Wen, Y. Lei, Y. Xie, Photoelectrodes based upon Mo:BiVO₄ inverse opals for photoelectrochemical water splitting, *ACS Nano*. 8 (2014) 7088–7098. <https://doi.org/10.1021/nm501996a>.
- [125] L. Ran, S. Qiu, P. Zhai, Z. Li, J. Gao, X. Zhang, B. Zhang, C. Wang, L. Sun, J. Hou, Conformal Macroporous Inverse Opal Oxynitride-Based Photoanode for Robust Photoelectrochemical Water Splitting, *J. Am. Chem. Soc.* 143 (2021) 7402–7413. <https://doi.org/10.1021/jacs.1c00946>.
- [126] L. Zhang, C. Baumanis, L. Robben, T. Kandiel, D. Bahnemann, Bi₂WO₆ inverse opals: Facile fabrication and efficient visible-light-driven photocatalytic and photoelectrochemical water-splitting activity, *Small*. 7 (2011) 2714–2720. <https://doi.org/10.1002/sml.201101152>.
- [127] K. Zhang, X. Shi, J.K. Kim, J.S. Lee, J.H. Park, Inverse opal structured α -Fe₂O₃ on graphene thin films: Enhanced photo-assisted water splitting, *Nanoscale*. 5 (2013) 1939–1944. <https://doi.org/10.1039/c2nr33036a>.
- [128] R. Yew, H.H. Tan, C. Jagadish, S.K. Karuturi, Three-dimensional ordered macroporous TiO₂–TaOxny heterostructure for photoelectrochemical water splitting, *J. Phys. Chem. C*. 124 (2020) 24135–24144. <https://doi.org/10.1021/acs.jpcc.0c05039>.
- [129] Z. Chen, M. Fu, Z. Wu, C. Li, J. Jiang, Facile Synthesis of Au Nanoparticles Supported on TiO₂ Inverse Opals with Biosensor, *J. Phys. Conf. Ser.* 1622 (2020). <https://doi.org/10.1088/1742-6596/1622/1/012066>.
- [130] Y. Xie, R. Xing, Q. Li, L. Xu, H. Song, Three-dimensional ordered ZnO-CuO inverse opals toward low concentration acetone detection for exhaled breath sensing, *Sensors Actuators, B Chem.* 211 (2015) 255–262. <https://doi.org/10.1016/j.snb.2015.01.086>.
- [131] Y. Yan, Z. Liu, W. Pang, S. Huang, M. Deng, J. Yao, Q. Huang, M. Jin, L. Shui, Integrated biosensor array for multiplex biomarkers cancer diagnosis via in-situ self-assembly carbon nanotubes with an ordered inverse-opal structure, *Biosens. Bioelectron.* 262 (2024). <https://doi.org/10.1016/j.bios.2024.116528>.
- [132] Y. Jiang, P. Zheng, D. Li, L. Zhou, L. Tian, J. Wang, B. Yang, X. Wang, X. Zhang, J. Gao, Enzyme-containing silica inverse opals prepared by using water-soluble colloidal crystal templates: Characterization and application, *Biochem. Eng. J.* 112 (2016) 123–

129. <https://doi.org/10.1016/j.bej.2016.04.007>.
- [133] T. Wang, L. Wang, N. Ma, Y. Zhang, L. Liu, Y. Wan, L. Zhou, W. Qian, Nanoporous Polystyrene Inverse Opal Materials with Optical Interference Properties for Label-Free Biosensing, *Langmuir*. (2024). <https://doi.org/10.1021/acs.langmuir.4c01947>.
- [134] S.S. Shenouda, M.S.A. Hussien, B. Parditka, A. Csík, V. Takats, Z. Erdélyi, Novel amorphous Al-rich Al₂O₃ ultra-thin films as active photocatalysts for water treatment from some textile dyes, *Ceram. Int.* 46 (2020) 7922–7929. <https://doi.org/10.1016/j.ceramint.2019.12.012>.
- [135] G. Greczynski, L. Hultman, Binding energy referencing in X-ray photoelectron spectroscopy, *Nat. Rev. Mater.* 10 (2024). <https://doi.org/10.1038/s41578-024-00743-5>.
- [136] H.K.E. Latha, H.S. Lalithamba, Synthesis and Characterization of Titanium Dioxide Thin Film for Sensor Applications, *Mater. Res. Express.* 5 (2018). <https://doi.org/10.1088/2053-1591/aab695>.
- [137] A.R. Zanatta, Revisiting the optical bandgap of semiconductors and the proposal of a unified methodology to its determination, *Sci. Rep.* 9 (2019) 11225. <https://doi.org/10.1038/s41598-019-47670-y>.
- [138] C. Yang, Q. Li, ZnO inverse opals with deposited Ag nanoparticles: Fabrication, characterization and photocatalytic activity under visible light irradiation, *J. Photochem. Photobiol. A Chem.* 371 (2019) 118–127. <https://doi.org/10.1016/j.jphotochem.2018.10.039>.
- [139] C.A. Aggelopoulos, M. Dimitropoulos, A. Govatsi, L. Sygellou, C.D. Tsakiroglou, S.N. Yannopoulos, Influence of the surface-to-bulk defects ratio of ZnO and TiO₂ on their UV-mediated photocatalytic activity, *Appl. Catal. B Environ.* 205 (2017) 292–301. <https://doi.org/10.1016/j.apcatb.2016.12.023>.
- [140] Y.Q. Cao, T.Q. Zi, X.R. Zhao, C. Liu, Q. Ren, J. Bin Fang, W.M. Li, A.D. Li, Enhanced visible light photocatalytic activity of Fe₂O₃ modified TiO₂ prepared by atomic layer deposition, *Sci. Rep.* 10 (2020) 1–10. <https://doi.org/10.1038/s41598-020-70352-z>.
- [141] H. Noh, M. Scharrer, M.A. Anderson, R.P.H. Chang, H. Cao, Photoluminescence modification by a high-order photonic band with abnormal dispersion in ZnO inverse opal, *Phys. Rev. B - Condens. Matter Mater. Phys.* 77 (2008) 1–9.

<https://doi.org/10.1103/PhysRevB.77.115136>.

- [142] O.K.M. Bashiar, R.E. Kroon, H.C. Swart, R.A. Harris, Producing ZnO films that exhibited near-infrared (NIR) luminescence with a templated design procedure, *Phys. B Condens. Matter.* 673 (2024) 415523. <https://doi.org/10.1016/j.physb.2023.415523>.
- [143] L. Liu, S.K. Karuturi, L.T. Su, A.I.Y. Tok, TiO₂ inverse-opal electrode fabricated by atomic layer deposition for dye-sensitized solar cell applications, *Energy Environ. Sci.* 4 (2011) 209–215. <https://doi.org/10.1039/c0ee00086h>.
- [144] D.B. Thinh, N.T. Tien, N.M. Dat, H.H.T. Phong, N. Thi Huong Giang, L.T. Tai, D. Thi Yen Oanh, H.M. Nam, M.T. Phong, N.H. Hieu, Improved photodegradation of p-nitrophenol from water media using ternary MgFe₂O₄-doped TiO₂/reduced graphene oxide, *Synth. Met.* 270 (2020) 116583. <https://doi.org/10.1016/j.synthmet.2020.116583>.
- [145] N. Wang, G. Lv, L. He, X. Sun, New insight into photodegradation mechanisms, kinetics and health effects of p-nitrophenol by ozonation in polluted water, *J. Hazard. Mater.* 403 (2021) 123805. <https://doi.org/10.1016/j.jhazmat.2020.123805>.
- [146] H.G. Lee, G. Sai-Anand, S. Komathi, A.I. Gopalan, S.W. Kang, K.P. Lee, Efficient visible-light-driven photocatalytic degradation of nitrophenol by using graphene-encapsulated TiO₂ nanowires, *J. Hazard. Mater.* 283 (2015) 400–409. <https://doi.org/10.1016/j.jhazmat.2014.09.014>.
- [147] M.M. Ali, M.J. Haque, M.H. Kabir, M.A. Kaiyum, M.S. Rahman, Nano synthesis of ZnO–TiO₂ composites by sol-gel method and evaluation of their antibacterial, optical and photocatalytic activities, *Results Mater.* 11 (2021) 100199. <https://doi.org/10.1016/j.rinma.2021.100199>.
- [148] Y. zhen Dong, Y. shan Xue, W. wei Yang, H. ming You, Y. Su, Visible light driven CdS/WO₃ inverse opals with enhanced RhB degradation activity, *Colloids Surfaces A Physicochem. Eng. Asp.* 561 (2019) 381–387. <https://doi.org/10.1016/j.colsurfa.2018.10.033>.
- [149] X.M. Liu, W.L. Zhong, Y.C. Huang, G.S. Zhang, X.K. Bai, X.C. Wei, C.X. Lei, Facile preparation of spherical TiO₂ inverse opals with enhanced visible-light photodegradation of methylene blue, *J. Mater. Sci. Mater. Electron.* 32 (2021) 21742–21755. <https://doi.org/10.1007/s10854-021-06694-9>.

- [150] Y. Wan, J. Wang, X. Wang, H. Xu, S. Yuan, Q. Zhang, M. Zhang, Preparation of inverse opal titanium dioxide for photocatalytic performance research, *Opt. Mater. (Amst)*. 96 (2019) 109287. <https://doi.org/10.1016/j.optmat.2019.109287>.
- [151] Z. Gholizadeh, M. Aliannezhadi, M. Ghominejad, F.S. Tehrani, High specific surface area γ -Al₂O₃ nanoparticles synthesized by facile and low-cost co-precipitation method, *Sci. Rep.* 13 (2023) 1–14. <https://doi.org/10.1038/s41598-023-33266-0>.
- [152] P. Paul, M.G. Hafiz, P. Schmitt, C. Patzig, F. Otto, T. Fritz, A. Tünnermann, A. Szeghalmi, Optical bandgap control in Al₂O₃/TiO₂ heterostructures by plasma enhanced atomic layer deposition: Toward quantizing structures and tailored binary oxides, *Spectrochim. Acta - Part A Mol. Biomol. Spectrosc.* 252 (2021) 119508. <https://doi.org/10.1016/j.saa.2021.119508>.
- [153] A.I. Kostyukov, A. V. Zhuzhgov, V. V. Kaichev, A.A. Rastorguev, V.N. Snytnikov, V.N. Snytnikov, Photoluminescence of oxygen vacancies in nanostructured Al₂O₃, *Opt. Mater. (Amst)*. 75 (2018) 757–763. <https://doi.org/10.1016/j.optmat.2017.11.040>.
- [154] D. Gupta, V. Chauhan, N. Koratkar, F. Singh, A. Kumar, S. Kumar, R. Kumar, High energy (MeV) ion beam induced modifications in Al₂O₃-ZnO multilayers thin films grown by ALD and enhancement in photoluminescence, optical and structural properties, *Vacuum*. 192 (2021). <https://doi.org/10.1016/j.vacuum.2021.110435>.
- [155] V.A. Pustovarov, T. V. Perevalov, V.A. Gritsenko, T.P. Smirnova, A.P. Yelisseyev, Oxygen vacancy in Al₂O₃: Photoluminescence study and first-principle simulation, *Thin Solid Films*. 519 (2011) 6319–6322. <https://doi.org/10.1016/j.tsf.2011.04.014>.
- [156] L.D.V. Sangani, M.A. Mohiddon, G. Rajaram, M.G. Krishna, Optical confinement in TiO₂ waveguides fabricated by resist free electron beam lithography, *Opt. Laser Technol.* 123 (2020). <https://doi.org/10.1016/j.optlastec.2019.105901>.
- [157] K. Pham, H. Ali-Löyty, J. Saari, M. Zubair, M. Valden, K. Lahtonen, N. Kinnunen, M. Gunell, J.J. Saarinen, Functionalization of TiO₂ inverse opal structure with atomic layer deposition grown Cu for photocatalytic and antibacterial applications, *Opt. Mater. (Amst)*. 131 (2022). <https://doi.org/10.1016/j.optmat.2022.112695>.
- [158] M.T. Aguilar-Gama, E. Ramírez-Morales, Z. Montiel-González, A. Mendoza-Galván, M. Sotelo-Lerma, P.K. Nair, H. Hu, Structure and refractive index of thin alumina films

- grown by atomic layer deposition, *J. Mater. Sci. Mater. Electron.* 26 (2015) 5546–5552. <https://doi.org/10.1007/s10854-014-2111-z>.
- [159] D. Karajz, D. Cseh, B. Parditka, Z. Erdélyi, I. Szilágyi, Combining ZnO inverse opal and ZnO nanorods using ALD and hydrothermal growth, *J. Therm. Anal. Calorim.* (2022). <https://doi.org/10.1007/s10973-022-11255-1>.
- [160] M. Scharrer, X. Wu, A. Yamilov, H. Cao, R.P.H. Chang, Fabrication of inverted opal ZnO photonic crystals by atomic layer deposition, *Appl. Phys. Lett.* 86 (2005) 1–3. <https://doi.org/10.1063/1.1900957>.
- [161] J. Lv, C. Li, Z. Chai, Defect luminescence and its mediated physical properties in ZnO, *J. Lumin.* 208 (2019) 225–237. <https://doi.org/10.1016/j.jlumin.2018.12.050>.
- [162] C. Yang, W. Dong, G. Cui, Y. Zhao, X. Shi, X. Xia, B. Tang, W. Wang, Highly efficient photocatalytic degradation of methylene blue by P2ABSA-modified TiO₂ nanocomposite due to the photosensitization synergetic effect of TiO₂ and P2ABSA, *RSC Adv.* 7 (2017) 23699–23708. <https://doi.org/10.1039/c7ra02423a>.
- [163] R. Chakraborty, A. Dey, A.K. Mukhopadhyay, Loading rate effect on nanohardness of soda-lime-silica glass, *Metall. Mater. Trans. A Phys. Metall. Mater. Sci.* 41 (2010) 1301–1312. <https://doi.org/10.1007/s11661-010-0176-8>.
- [164] M.J. Šćepanović, M.U. Grujić-Brojčin, Z.D. Dohčević-Mitrović, Z. V. Popović, Effects of confinement, strain and nonstoichiometry on Raman spectra of anatase TiO₂ nanopowders, *Mater. Sci. Forum.* 518 (2006) 101–106. <https://doi.org/10.4028/www.scientific.net/MSF.518.101>.
- [165] B. Hu, M. Yao, R. Xiao, J. Chen, X. Yao, Optical properties of amorphous Al₂O₃ thin films prepared by a sol-gel process, *Ceram. Int.* 40 (2014) 14133–14139. <https://doi.org/10.1016/j.ceramint.2014.05.148>.
- [166] I. Costina, R. Franchy, Band gap of amorphous and well-ordered Al₂O₃ on Ni₃Al(100), *Appl. Phys. Lett.* 78 (2001) 4139–4141. <https://doi.org/10.1063/1.1380403>.
- [167] S. Shi, S. Qian, X. Hou, J. Mu, J. He, X. Chou, Structural and optical properties of amorphous Al₂O₃ thin film deposited by atomic layer deposition, *Adv. Condens. Matter Phys.* 2018 (2018). <https://doi.org/10.1155/2018/7598978>.
- [168] C. Jin, B. Liu, Z. Lei, J. Sun, Structure and photoluminescence of the TiO₂ films grown

by atomic layer deposition using tetrakis-dimethylamino titanium and ozone, *Nanoscale Res. Lett.* 10 (2015). <https://doi.org/10.1186/s11671-015-0790-x>.

- [169] P. Zhang, T. Tachikawa, M. Fujitsuka, T. Majima, Atomic Layer Deposition-Confined Nonstoichiometric TiO₂ Nanocrystals with Tunneling Effects for Solar Driven Hydrogen Evolution, *J. Phys. Chem. Lett.* 7 (2016) 1173–1179. <https://doi.org/10.1021/acs.jpcllett.6b00227>.

9. APPENDICES

9.1. APPENDIX A

Summary of PBG properties, IO synthesised from PS-300 templates

Sample	n	D (nm)	n_{avg}	Shrinkage (%)	$\lambda_{calculated}$ (nm)	$\lambda_{experimental}$ (nm)	E_g (eV)
PS	1.6	290	1.4	-	493	-	-
TiO ₂ IO	2.5	250	1.4	14	394	400	3.0
TiO ₂ /ZnO	2.5	260	1.4	11	390	400	3.2
ZnO IO	2.0	280	1.3	3.4	380	470	3.2
ZnO/TiO ₂	2.0	280	1.3	3.4	380	500	3.2

9.2. APPENDIX B

Summary of PBG properties IO synthesised from PS-460 templates

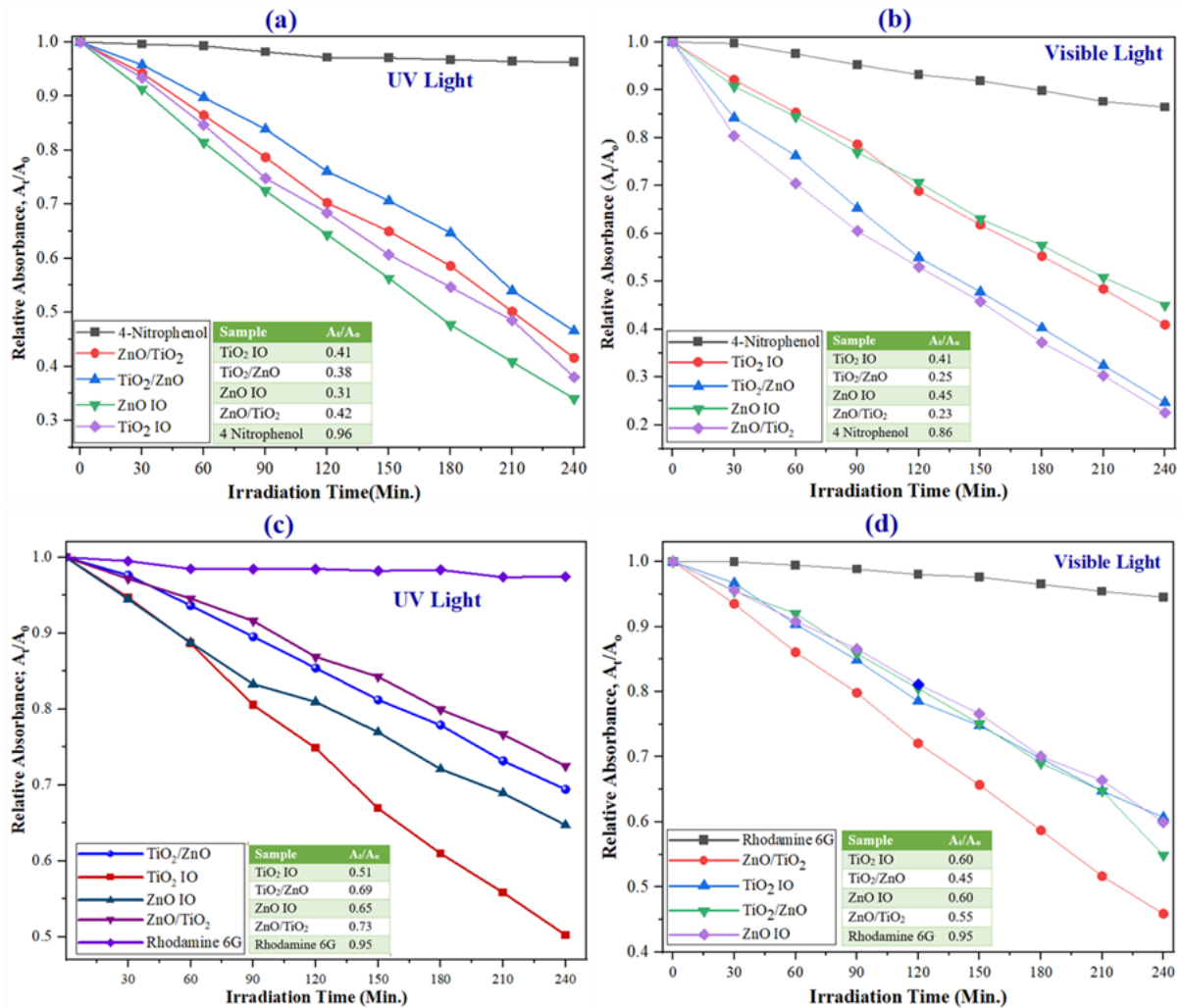
Sample	D (nm)	f	% Shrinkage	n_{avg}	PBG position Calculated (nm)	PBG position Experimental (nm)
PS-template	460	0.74	-	1.44	782	-
Pure Al ₂ O ₃ IO	433	0.26	5.9	1.15	479	529
Al ₂ O ₃ /ZnO-T	429	0.26	6.7	1.16	482	529
Al ₂ O ₃ /ZnO-P	415	0.26	9.8	1.16	482	529
Al ₂ O ₃ /TiO ₂ -T	429	0.26	6.7	1.18	501	529
Al ₂ O ₃ /TiO ₂ -P	415	0.26	9.8	1.18	501	529

9.3. APPENDIX C

Summary of PBG properties IO synthesized from PS-600 templates

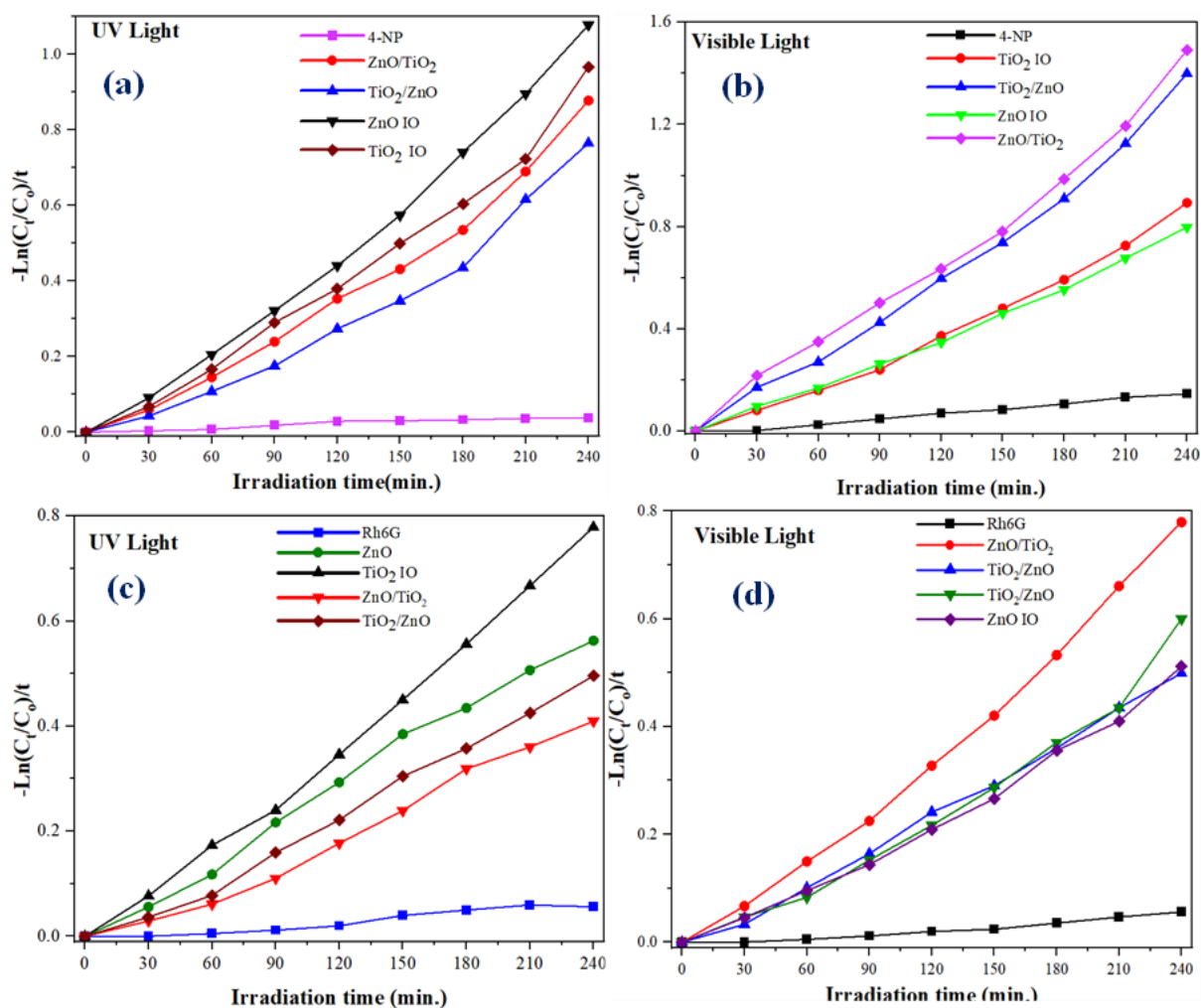
Sample	Average void size: D (nm) ^a	Shrinkage (%)	n	n_{avg}	$\lambda_{max, exp}$ [nm]	$\lambda_{max, calc}$ [nm]
PS-template	588	-	1.59	1.44	ND	990
ZnO IO	541	8.0	2.00	1.24	560	676
ZnO/Al ₂ O ₃ -T	451	16.7	1.70	1.25	580	557

9.4. APPENDIX D



Photocatalytic degradation of organic pollutants using UV and visible light:(a & b) for 4-nitrophenol and (c & d) for rhodamine 6G respectively.

9.5. APPENDIX E



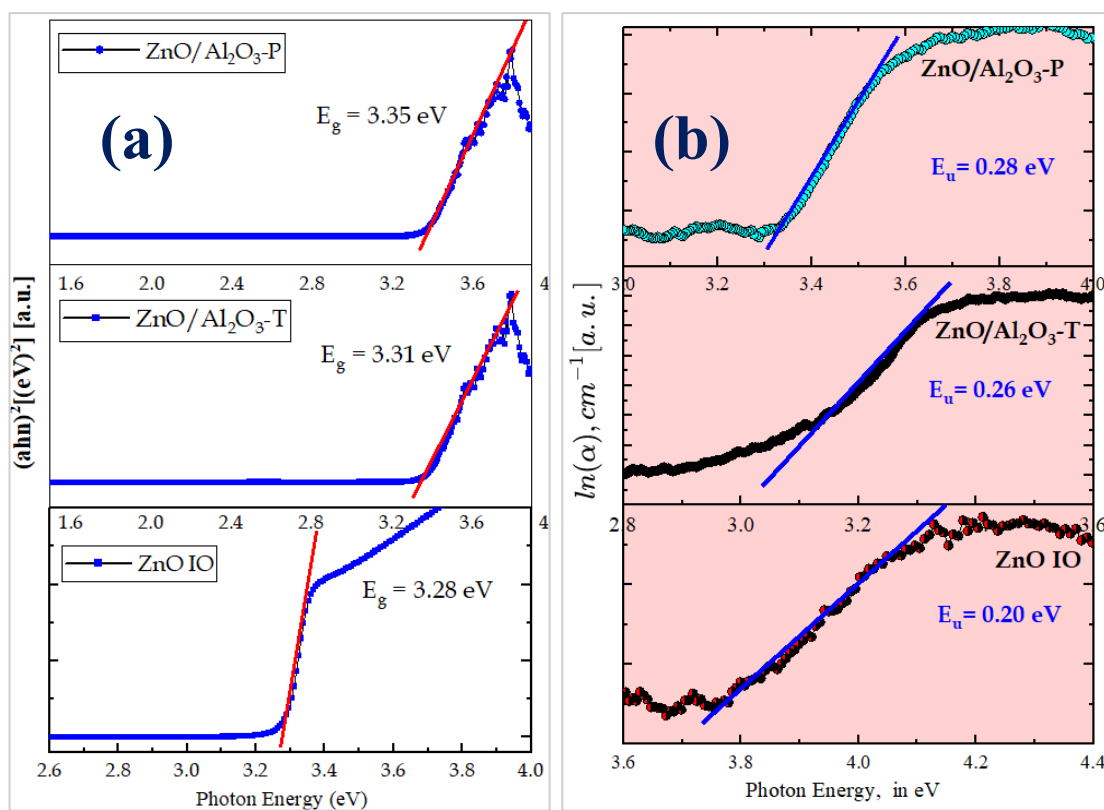
Rate of photocatalytic degradation of organic dyes using UV and visible light: (a & b) for 4-NP and (c & d) for Rh6G, respectively.

9.6. APPENDIX F

k_{app} of the samples, $k_{app}[10^{-2}/\text{min}^{-1}]$

Sample	UV source	Visible source	Sample	UV source	Visible source
4-NP	0.038	0.14	Rh6G	0.05	0.05
TiO ₂ IO	0.96	0.89	TiO ₂ IO	0.78	0.51
TiO ₂ /ZnO	0.77	1.39	TiO ₂ /ZnO	0.50	0.60
ZnO IO	1.07	0.79	ZnO IO	0.56	0.51
ZnO/TiO ₂	0.88	1.49	ZnO/TiO ₂	0.41	0.78

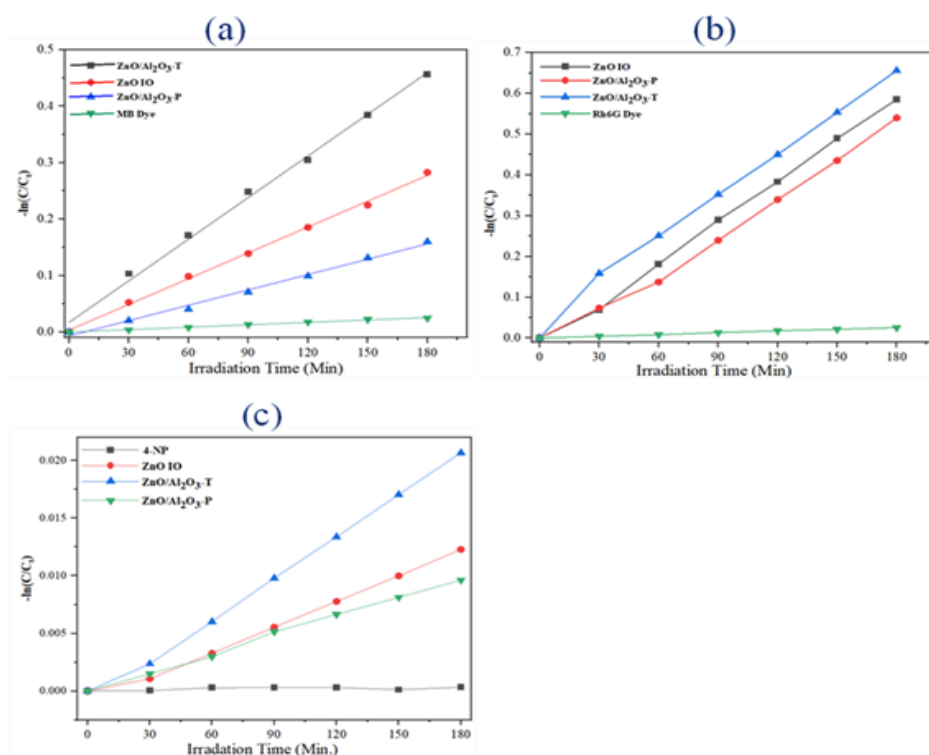
9.7. APPENDIX G



(a) The Tauc plot derived from UV Visible absorption analysis of ALD samples

(b) The Urbach energy (E_u) values of the samples

9.8. APPENDIX H



The pseudo-first-order linear plots of $\ln(C_0/C_t)$ versus irradiation time, illustrating the reaction kinetics for all sample materials.

9.9. APPENDIX I

Rate constant, k , and R-squared of the sample in dyes

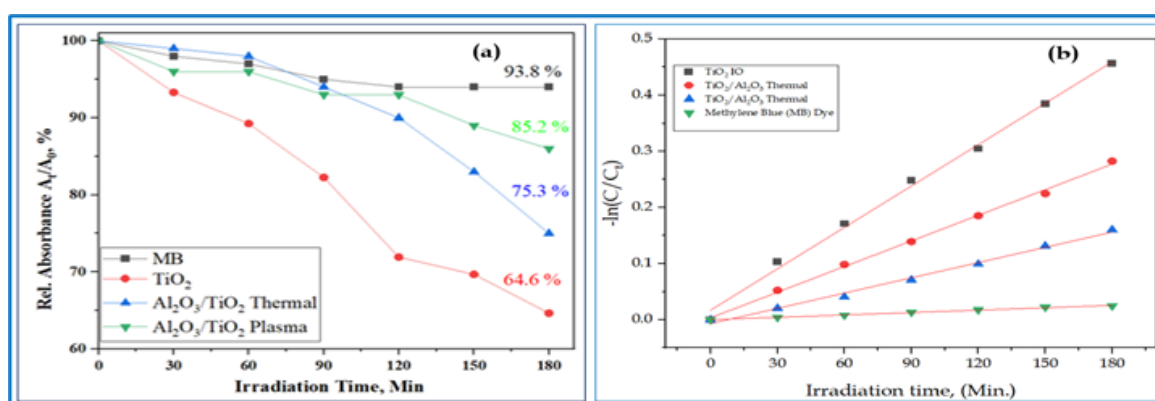
Sample	MB		Rh6G		4-NP	
	$k \times 10^{-2}(\text{min}^{-1})$	R^2	$k \times 10^{-2}(\text{min}^{-1})$	R^2	$k \times 10^{-2}(\text{min}^{-1})$	R^2
ZnO IO	0.19	0.9993	0.17	0.9993	0.11	0.9991
ZnO/Al ₂ O ₃ - T	0.22	0.9995	0.19	0.9994	0.15	0.9984
ZnO/Al ₂ O ₃ - P	0.11	0.9975	0.10	0.9966	0.10	0.9996

9.10. APPENDIX J

EDX Compositional analysis of the samples

Sample	% w/w Ti	% w/w Al	% w/w O	% w/w C	% w/w Si	% w/w Ca	% w/w Cl	% w/w Na
TiO ₂	23.4	-	64.0	3.2	8.0	-	-	1.4
TiO ₂ /Al ₂ O ₃	18.1	2.6	64.3	3.8	7.9	1.4	0.3	1.6
Thermal								
TiO ₂ /Al ₂ O ₃	19.0	2.5	65.6	2.8	7.8	1.4	0.3	1.6
Plasma								

9.11. APPENDIX K



Photocatalytic performance- Relative absorbance in % vs Irradiation time in minute (a) and Pseudo-first-order linear plots of $\ln(C_0/C_t)$ vs. irradiation time for the degradation kinetics of the sample materials (b).

9.12. APPENDIX L

Table: Distribution of elements based on their atomic %.

Samples	Line	Ti (atomic %)	Zn (atomic %)	O (atomic %)	Others (atomic %)
TiO ₂ IO	Ka	39.5	-	57.3	3.2
TiO ₂ /ZnO	Ka	44.7	9.9	40.7	4.7
ZnO IO	Ka	-	40.5	54.3	5.2
ZnO/TiO ₂	Ka	10.9	38.6	46.1	4.4

10. ACKNOWLEDGEMENT

First and foremost, I extend my deepest gratitude to Almighty God, through Jesus Christ, for His divine guidance, wisdom, and unwavering light throughout my journey.

I would like to express my heartfelt appreciation to my supervisor, Professor Dr. Szilágyi Imre Miklós, for his invaluable support, mentorship, and encouragement during my studies. His patience, insight, and dedication have been instrumental in shaping both my academic and personal growth.

My sincere thanks also go to Dr. Erdélyi Zoltán, Dr. Cserháti Csaba, Dr. Baradács Eszter Mónika, and Dr. Pál Petra for their guidance, support, and collaboration during my research at the University of Debrecen.

I am deeply grateful to my colleagues Karajz Dániel (PhD), Bohus Marcell, Zalán Várady, Niloofar Bayat, and Karanja Lucy for their friendship, teamwork, and the sense of belonging they fostered within our research group. My heartfelt appreciation also goes to my friends and compatriots in Budapest, Atallo Kassaw, Ermiyas Belachew (PhD), and Anteneh Agezew (PhD) for their companionship and support whenever I was in need.

I would like to acknowledge the staff of the Department of Inorganic and Analytical Chemistry and the George Oláh Doctoral School, Budapest University of Technology and Economics, for providing an enriching academic environment and continuous support throughout my studies. I am also sincerely thankful to Stipendium Hungaricum, Tempus Foundation, and the Government of Ethiopia for the generous scholarship that made this study possible.

Finally, my deepest love and gratitude go to my beloved wife Wubshet, my sons Eyobed and Robel, my brothers, sisters, relatives, and friends. Your unwavering love, prayers, and encouragement have been my greatest strength. May the Lord bless you abundantly and specially touch your lives.

DECLARATION

I, the undersigned, declare that this PhD thesis is entirely my own work and I have only used the sources referenced. Any parts that have been quoted from the works of others or have been taken from other sources and rephrased, have been clearly stated with the source indicated.

Budapest..... November 2025



.....
Hamsasew Hankebo Lemago (PhD Candidate)